Dissertation

submitted to the

Combined Faculties for the Natural Sciences and for Mathematics

of the Ruperto-Carola University of Heidelberg, Germany

for the degree of

Doctor of Natural Sciences

presented by

Diplom-Physicist Lutz Lammich

born in Ludwigshafen am Rhein

Oral examination: 12. May 2004

Fragmentation Studies with Stored Beams of Small Polyatomic Ions

Referees: **Prof. Dr. Andreas Wolf**
Prof. Dr. H.-Jürgen Kluge

Kurzfassung

Fragmentations-Studien an gespeicherten Strahlen kleiner mehratomiger Molekülionen

Die Struktur kleiner Moleküle hängt wie auch ihre Reaktionen eng mit den fundamentalen Mechanismen zusammen, die allen chemischen Reaktionen zugrundeliegen. Experimentelle Untersuchungen molekularer Fragmentationsprozesse liefern daher einen wichtigen Beitrag zum detaillierten Verständnis dieser grundlegenden Mechanismen. Als geeignete Umgebung für solche Studien an Molekülionen stehen heute Schwerionen-Speicherringe zur Verfügung, mit denen bisher hauptsächlich zweiatomige Molekülionen unter wohldefinierten Bedingungen und mit effizientem Nachweis der produzierten Fragmente untersucht wurden. Für eine genaue Untersuchung mehratomiger Systeme müssen die in früheren Fragmentationsstudien an zweiatomigen Ionen etablierten Techniken in mehreren Aspekten erweitert werden, hauptsächlich bezüglich der Identifikation der entstehenden Fragmente und der Auswertung der hier auftretenden multi-dimensionalen Fragmentationsgeometrien. In der vorliegenden Arbeit wird die Erweiterung experimenteller Methoden auf dreiatomige Moleküle für zwei Fälle studiert: Für die Dissoziative Rekombination des H_3^+-Kations und seiner Isotopomere mit langsamen Elektronen, mit dem Schwerpunkt auf Fragmentationsgeometrien und Isotopeffekten, sowie die Fragmentation des LiH_2^--Anions nach Entfernen eines Elektrons, hier mit dem Schwerpunkt auf der chemischen Zusammensetzung der Produkte.

Abstract

Fragmentation Studies with Stored Beams of Small Polyatomic Ions

The structure of small molecules, as well as their reactions, is closely related to the fundamental mechanisms governing all chemical reactions. Experimental investigations of molecular fragmentation processes thus yield important data contributing to the detailed understanding of these basic mechanisms. As an advantageous environment for such studies on molecular ions nowadays heavy ion storage rings are available, where so far mainly diatomic molecules were studied under well defined conditions and with efficient detection of the fragments produced. For a detailed investigation of polyatomic systems, the standard techniques established for previous fragmentation studies on diatomic ions have to be extended in several aspects, mainly connected to the identification of the emerging fragments and to the analysis of the occurring multi-dimensional breakup geometries. In this work, the extension of experimental methods on triatomic molecules is studied for two cases: The dissociative recombination of the H_3^+ cation and its isotopomers with slow electrons, focusing on fragmentation geometries and isotope effects, and the fragmentation of the LiH_2^- anion following electron detachment, here focusing on the chemical composition of the products.

Contents

Contents

1. Introduction

Fragmentation is a fundamental phenomenon occurring in many fields of physics and chemistry. Besides an interest in the actual fragmentation dynamics itself, in many cases the fragmentation of a system is also initiated on purpose for studying structural properties which cannot be addressed in the undisturbed system.

Examples reach from high energy physics, where the fragments emerging from very high energetic collisions are studied to gain insight in the properties of the particles and interactions involved in the reaction, over nuclear physics, where the most prominent example is the large-scale technical use of energy released in the fragmentation of heavy nuclei, to the wide field of atomic and molecular physics with its applications in chemistry and biology. Considering larger systems, even the phase transition of a liquid to its gaseous form, or the breakup of a macroscopic compound by mechanical force, revealing properties of interest in material science, can be viewed as examples of fragmentation reactions in a most general sense.

In atomic and molecular physics, the spectrum of fragmentation reactions includes processes like the ionisation of an atom, whose dynamics especially is investigated in modern experiments capable of recording a full, energy and momentum resolved picture of fragments as different as an atomic ion and an electron. On the other hand, fragmentation processes involving large metal clusters or biomolecules are studied today on an event-by-event basis.

In this work, the focus is set on event-by-event studies of the fragmentation of *small molecular ions* in a dilute environment, where an unstable excited state of the investigated system is created in a collision with a free electron or, in some cases, might result already from the process in which the molecular ion was previously prepared. The basic phenomenon consists in the separation of nuclei formerly bound in a molecular system to macroscopic distances, that is, the breaking of chemical bonds. Small molecules containing only few atoms here lend themselves to detailed studies both experimentally and theoretically, giving insight in the fundamental mechanisms of chemical bonding. For many particular breakup reactions, there are in addition applications in astrophysics or plasma physics, which increase the demand for a detailed understanding of these systems.

Numerous studies have been performed on the most simple type of molecules, the various diatomic species. However, a large interest exists also in small *polyatomic* molecules containing

three or more atoms. On the theoretical side, the multi-dimensionality of the vector space describing the arrangement of the nuclei in these systems turns their treatment into a challenging task concerning both the quantum chemical methods and the computational resources required. Also experimentally, careful considerations are necessary when extending the standard techniques established for diatomic fragmentation studies to experiments on polyatomic systems. In the present work, experimental investigations of the electron-induced fragmentation of several triatomic molecular ions will be discussed. Special emphasis will be put on the new aspects to be considered when moving from the well-known diatomic case to polyatomic fragmentation studies. The main aspects discussed are the measurement and analysis of fragmentation geometries and of partial cross sections or branching ratios for fragmentation channels with different chemical composition of the products.

In the next chapter, the actual breakup processes to be studied will be introduced in some more detail. The experimental apparatus employed in the present studies is that of a *heavy-ion storage ring*. This technique is exceptionally suited for fragmentation studies on small molecular ions, as will be discussed in Chapter 3.

After these preparations, Chapters 4 and 5 present the results obtained from experiments on the electron induced fragmentation of H_3^+ and LiH_2^-, respectively. In the case of H_3^+, the process of *dissociative recombination* of the ions with low-energy electrons is studied. The focus here lies on an investigation of the energy release and geometry of the breakup reaction, in particular for the observed three-body fragmentation channel. For an exploration of possible isotope effects, the same studies are repeated with the isotopomers of H_3^+, that is D_3^+, H_2D^+ and D_2H^+.

For LiH_2^-, the fragmentation after *electron detachment* was investigated. In this case, the main topic was an identification of the exit channels and possible reaction pathways of the breakup reaction, for which no previous experimental data were available. The results are contrasted to existing theoretical approaches as well as new, preliminary *ab initio* calculations.

Chapter 6 finally gives a summary of the results obtained and an outlook on possible future applications of the methods discussed in this work.

2. Fragmentation of molecules

This chapter gives an overview of the molecular fragmentation processes which are subject to the experimental investigations presented later in this work. After an introduction of the basic concepts needed for the description of molecules and their fragmentation reactions, experimental applications are addressed in the form of some particular types of fragmentation processes. A more detailed introduction is then given for the case of electron-induced fragmentation of molecular ions, being the actual process studied in the following chapters.

While diatomic molecules are used as introductory examples, the principal subject of this work is the generalisation of these concepts to polyatomic systems. As will be seen, already the seemingly small step from diatomic to triatomic systems introduces a variety of new aspects regarding the physics of molecular fragmentation reactions, but also concerning the experimental methods needed in the investigation of polyatomic systems.

2.1 General concepts

2.1.1 Molecular structure: The concept of potential energy surfaces

The structures and reactions of molecular systems are usually described based on the Born-Oppenheimer (BO) approximation [10]. This fundamental principle makes use of the considerable mass difference of the electrons and nuclei involved, which leads to a corresponding difference in typical velocities of the electronic and nuclear motion. Approximatively, the electrons can thus be assumed to immediately follow the relatively slow movement of the nuclei. Using this assumption, the basic problem of solving the Schrödinger equation for a molecular system can be separated into two problems of reduced dimensionality: First, the wave functions describing the movement of the electrons are determined for fixed positions of the nuclei. That is, the spatial coordinates of the nuclei enter in the description of the electronic system only as external parameters. The electronic eigenenergies found for each nuclear arrangement then, together with the mutual Coulomb interaction of the nuclei, are viewed as potential energy functions which govern the movement of the nuclei. In a second step, the Schrödinger equation

corresponding to the nuclear motion can then be solved. The forces acting on the nuclei are thus described here as a result of the different binding energy of the system at different geometric arrangements of the nuclei.

The noted potential energy function in this picture plays a central role for the description of nuclear dynamics. The equilibrium structure of a bound molecule can be found as the geometry corresponding to the minimum of the potential energy. The vibrational motion is described as oscillations around this minimum. Finally, also the fragmentation of a molecular system is determined by a potential energy function, which for example can possess a minimum at a geometry that corresponds to infinite separation of the fragments.

Depending on the number of atoms to be described, the number of coordinates varies which is needed to parametrise the nuclear arrangement and thus the potential energy function. In the simple case of a diatomic molecule, the system is described by one-dimensional potential energy curves $V(r)$ which only depend on the distance between the two nuclei. For triatomic molecules, already a three-dimensional *potential energy surface* (PES) has to be considered and the inclusion of even more atoms would introduce three more degrees of freedom with each additional atom.

The Born-Oppenheimer approximation yields a description of good accuracy for all problems where the potential energy surfaces corresponding to different electronic states are energetically well separated. In situations where the energy eigenvalues of the electronic system are degenerate or near-degenerate, couplings of the electronic and nuclear motion, which are considered zero in the BO case, become important. As a first step, shifts of the electronic energy levels due to the dependency of the electronic wave functions on the nuclear coordinates can be considered (adiabatic approximation). However, for an accurate description of the system in the case of considerable nuclear-electronic couplings, the eigenstates of the electronic system can no longer be considered stationary states of the total system. Therefore, the simple picture of the nuclear system moving on a single PES defined by the electronic state has to be given up.

However, the concept of potential energy surfaces can still be used for the description and visualisation of molecular structures and processes when keeping in mind the possible occurrence of non-Born-Oppenheimer effects in situations involving PES of similar energy.

An important attribute of a PES, besides its energy, are the *symmetry properties* of the corresponding electronic state (see, e.g. [11]). These are defined by the behaviour of the electronic wave function when applying symmetry operations like rotations or reflections that leave the nuclear system unchanged. For example, in a planar molecule a reflection on this plane will not change the nuclear arrangement. The electronic wave function can by this operation then either

stay unaffected or change its sign. In both cases, a second application of the same reflection will lead back to the original system. For molecules exhibiting this simple reflection symmetry (labelled C_S), the electronic states thus can be classified as symmetric (A') or antisymmetric (A'') with respect to the corresponding symmetry operation.

The importance of this classification, besides an easier solution of the electronic Schrödinger equation, lies in the fact that PES of different symmetry are allowed to cross, that is, the corresponding electronic systems can possess degenerate energy eigenvalues. For states of the same symmetry, such degeneracies in general are lifted by electronic couplings and an *avoided crossing* occurs. In the case of polyatomic molecules, the situation is further complicated by the appearance of additional symmetry properties of the nuclear system at certain geometries. For example, the aforementioned planar molecule will in the case of a linear arrangement of all nuclei also be symmetric under rotations about the such formed axis. The possibly different behaviour of the electronic wave functions under the new symmetry operations then leads to a refinement of the classification scheme. Thus, two PES belonging to the same class for planar arrangements can have different symmetry properties in the linear case and thus are allowed to cross at these specific geometries. This phenomenon leads to the appearance of so-called *conical intersections* of two PES at nuclear geometries with exceptional symmetry properties.

2.1.2 Fragmentation processes

The fragmentation of a molecule can be initiated by a variety of processes. Within the picture of a movement on potential energy surfaces, these can be divided into three cases:

(a) The system can stay on the same PES, that is in the same electronic eigenstate, but leave the minimum which defined the bound molecule.

(b) The electronic state of the system can change, corresponding to a transition to a different PES which exhibits no suitable minimum.

(c) A transition to a different system can happen. This includes for example the addition or removal of an electron, but also a temporary inclusion of one or more additional atoms.

Examples of these three types of fragmentation processes are sketched in Fig. 2.1 for the simplest case of a diatomic system. Similar considerations apply also to polyatomic molecules.
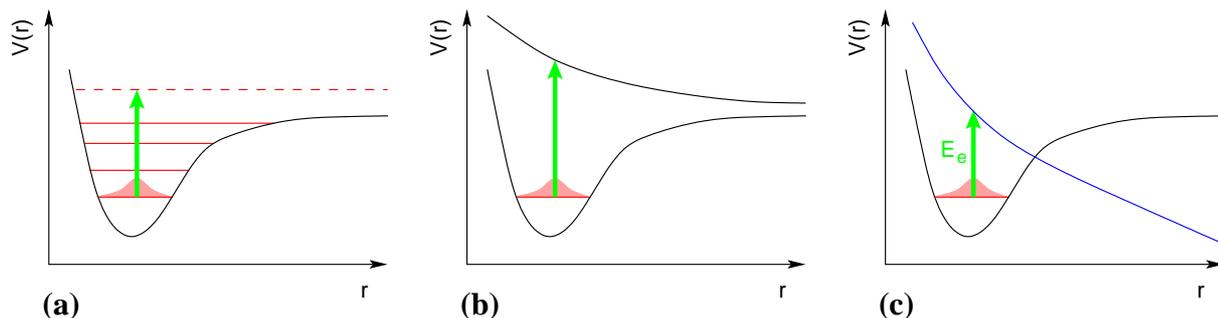
Fig. 2.1: *Three types of fragmentation processes visualised by the potential energy curve $V(r)$ for a diatomic molecule: (a) excitation to a vibrational continuum state of the same electronic PES, (b) transition to a different, non-binding PES, (c) change to another system, e.g. through the addition of an electron.*

In case (a) only one PES is involved, corresponding for example to the ground state of the electronic system (black curve). This PES possesses a minimum, which gives rise to several vibrational levels of the bound molecule, that is, to discrete eigenvalues of the Hamiltonian describing the nuclear motion (red lines).[1]

For the vibrational ground state, the square of the nuclear wave function is indicated in the figure. If the molecule now gains vibrational energy, for example in a collision or by absorption of a photon, it can either be excited to a higher-lying, bound vibrational state, or to a continuum state as indicated by the dashed red line. In the latter case, the molecule is no longer bound and the two atoms can separate to arbitrary distances.

Process (b) involves a change of the electronic eigenstate of the system. This transition can again be caused e.g. by the absorption of a photon, an inelastic collision with an electron or with some other particle. Compared to the nuclear motion, such an electronic transition takes place very fast (it is thus also called a *vertical transition*) and the nuclei suddenly find themselves on another PES with a possibly completely different shape. In other words, the nuclear spatial wave function of the system is projected vertically into the vibrational eigenfunctions belonging to the new PES. In the example shown in Fig. 2.1(b), these are continuum eigenfunctions of a dissociative PES, leading to a fragmentation of the molecule.

In process (c), the new state after the transition is not another electronic state of the original system, but instead some state of a different molecular system. The difference to the original system can for example lie in the number of electrons, but also in the nuclear composition. In principle, such a transition can be described as well as a transition within *one* system, which

---

1 In this overview, only electronic and vibrational degrees of freedom are considered. Rotational excitations could be included in this picture e.g. by defining one potential energy curve for each rotational-electronical state.

includes all the nuclei and electrons involved, some of them as the case may be at infinite spatial separation from the rest of the system. Thus it is possible to visualise also process (c) employing the concept of transitions between PES, keeping in mind that some of these states involve special properties of the system. In Fig. 2.1(c) e.g. the electronic state belonging to the black curve exhibits one electron at rest at infinite distance from the molecule. If this electron is accelerated to the energy E_e and brought close to the nuclei, the transition to the blue curve can occur, where the electron is bound, but the nuclei start to separate.

The fragmentation reactions studied in the following are of type (c), where not only an energetic excitation, but also the change to another system takes place. As the simplest form of such a system change, the addition or detachment of an electron will be investigated.

Besides the fragmentation processes discussed here, there are for most systems also transitions which lead to geometrically *stable* configurations. Except for the ground state of the total system, however, these states are only metastable and will undergo a transition to a lower state after some time. This phenomenon can lead to the observation of the spontaneous fragmentation of a molecule, which however does not constitute an additional mechanism for a fragmentation reaction, since some reaction that prepares the metastable state has to precede.

2.2 Experimental studies of molecular fragmentation

2.2.1 Motivation

An interesting quality of molecular fragmentation reactions is their ability to provide a link between the microscopic world of molecular structure and interactions on one side and the macroscopic scales accessible with experimental apparatus on the other side. This is especially the case for reactions producing neutral fragments, where the absence of long-range interactions between the fragments allows a direct 'view' on the dynamics of the actual fragmentation process. Studies of such reactions can give insight in both the structure of molecular systems, as described e.g. in terms of potential energy surfaces, and their interactions like the response of a molecular system on the advent of an additional electron.

The motivation for performing such experimental studies usually is twofold: First, the comparison of experimental results and theoretical calculations can help to refine the methods applied in these calculations and to approach a full theoretical understanding of the underlying mechanisms. Although molecular systems are governed by the well known rules of quantum mechanics and electrodynamics, their detailed quantum chemical description can impose considerable challenges already for seemingly simple systems like hydrogen molecules.

The second motive for studies of molecular fragmentation reactions is the importance of

many particular reactions in fields like chemistry, plasma physics or astrophysics. Astrophysical applications for example include the modelling of interstellar clouds, in which molecules play an essential role for processes like the formation of stars. The abundance of molecules in these environments is often determined by their destruction in fragmentation reactions [28].

2.2.2 Methods

In order to experimentally investigate a molecular fragmentation reaction, the molecule under study first has to be prepared in a state as well-defined as possible, regarding e.g. its electronic or rovibrational state. In a second step, the fragmentation reaction is then initiated. Finally, the outcome of the reaction is analysed, usually by detection of the emerging fragments.

In the experiments considered in this work, fragmentation processes are studied which are initiated by the impact of an electron on a molecular ion. Before moving on to a more detailed description of such electron induced processes in Sec. 2.3 and of the particular experimental method applied (Chap. 3), two different examples of molecular fragmentation experiments are shortly summarised:

- An important fragmentation mechanism is the process of *photodissociation*. Here the interaction with an electromagnetic field, produced e.g. by a laser, causes either an excitation of the molecule to a dissociative state, or even the removal of an electron. The latter process, *photoionisation* in the case of cations and neutrals, or *photodetachment* for anions, is in many cases also followed by dissociation. The underlying mechanisms are quite different depending on the intensity and wavelength of the light field in use, and range from single photon transitions, which can be studied at high spectral resolution, over multiple photon reactions up to the very strong electromagnetic fields achieved in intense laser pulses or, similarly, by the passage of a fast, highly charged ion (see, e.g. [12, 27]).

- Another fragmentation reaction is the interaction of a fast molecule with a solid, as used e.g. in the foil induced *Coulomb Explosion Imaging* technique [75]. The idea of this method is the sudden removal of all binding electrons of a molecule by the impact on a very thin foil. The remaining atomic fragments then dissociate driven by their well-known mutual Coulomb repulsion, and the analysis of the relative velocities reached by the fragments allows to draw conclusions on the geometrical structure of the molecule in the instant of impact in the foil. Besides the comparison to *ab initio* calculations of molecular wave functions, this technique is also used as a tool for the monitoring of vibrational excitations of molecular ions [81, 2].

Other fields of research involving the fragmentation of molecules extend up to interactions with 'exotic' particles like positrons [44] or more technical applications like the fragmentation of molecular anions in a gas target which is used in Tandem Van de Graaf accelerators for the production of MeV beams of molecular cations.

2.3 Electron induced fragmentation reactions

In the following, some mechanisms important in the electron induced fragmentation of molecular cations and anions are outlined. Special emphasis is put on reactions producing neutral fragments, as such reactions will be studied in the following chapters.

2.3.1 Cations: Dissociative excitation and recombination

Figure 2.2 gives a schematic overview of processes important in the electron induced fragmentation of a molecular cation. To start with a simple example, the potential energy curves of a diatomic cation AB^+ (red) and its neutral counterpart AB (black) are shown, that is, the energy of the system in a specific electronic state as a function of the distance r of the two nuclei. The molecule is assumed to be in the vibrational ground state $(v = 0)$, the squared wave func-
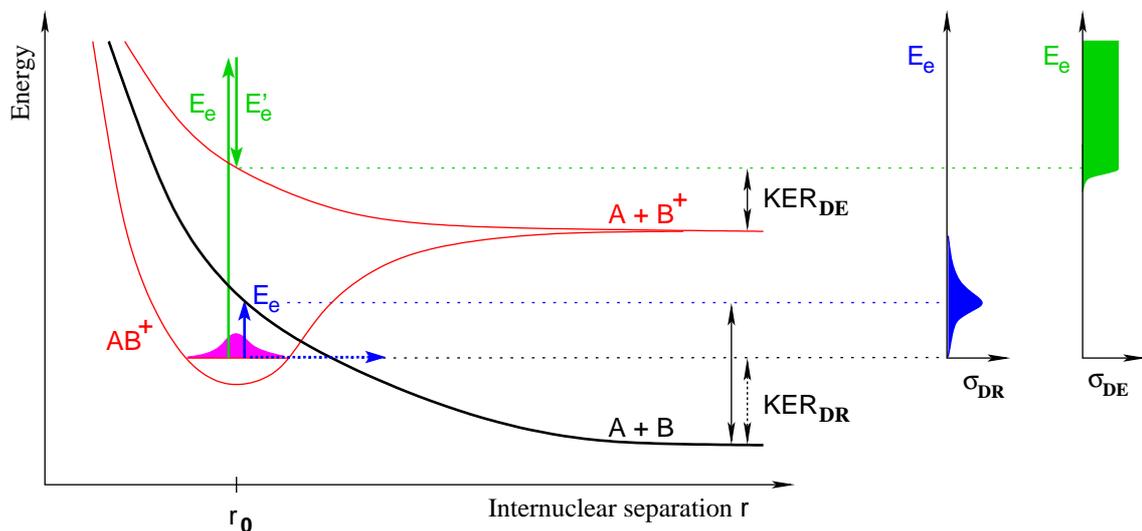
Fig. 2.2: *Dissociative recombination (DR) and dissociative excitation (DE) of a diatomic cation: Potential energy curves of the cation AB^+ (red) and the neutral AB (black) are sketched. The impact of an electron with energy E_e can lead to capture (blue) or excitation (green). In the latter case the electron is re-emitted with the energy E'_e. In the right part of the figure the cross sections σ for these reactions are outlined. The dotted blue arrow indicates a DR reaction for $E_e = 0$, resulting in a KER as depicted by the dotted black arrow.*

tion of internuclear distance $|\Psi(r)|^2$ is then concentrated around the equilibrium distance r_0, as indicated by the magenta coloured area.

The impact of an electron with the relative energy E_e can then initiate two fragmentation processes, the *Dissociative Recombination (DR)* and the *Dissociative Excitation (DE)*. Dissociative recombination describes a neutralisation of the cation by capture of the incoming electron into a dissociative state of the neutral AB system (indicated by the blue arrow in Fig. 2.2). The system then propagates to higher internuclear distances gaining kinetic energy and finally reaching a macroscopic separation of the nuclei and a kinetic energy release KER_{DR}. This process has a resonant character and works efficiently only if the electron energy E_e matches the transition energy from the $AB^+(v = 0)$ state to the A+B curve at the internuclear distance r_0 of the cation. More precisely, the cross section for electron capture is given by

$$\sigma_{\text{cap}} \propto \frac{1}{E_e}\left|\langle\Psi(r)|M(r)|\Phi_{E_e}(r)\rangle\right|^2 \tag{2.1}$$

where $M(r)$ denotes the electronic transition matrix element and $\Phi_{E_e}(r)$ a vibrational continuum eigenfunction of energy E_e belonging to the dissociative A+B potential. In the approximation of slowly variable $M(r)$, σ_{cap} is determined by the overlap of the bound and dissociative wave functions (Franck-Condon principle), which peaks for an E_e matching the transition energy close to the peak of $|\Psi(r)|^2$.

Once the system has reached the neutral AB state, it has a certain probability to *autoionize*, that is, to re-emit the electron into the continuum before reaching a high internuclear distance, and to descend back into the bound AB^+ state. This possibility gives rise to a survival factor S, which determines the DR cross section in addition to the capture process:

$$\sigma_{\text{DR}} = \sigma_{\text{cap}} \cdot S \tag{2.2}$$

The resulting spectrum of $\sigma_{\text{DR}}(E_e)$ is outlined in blue in the right part of Fig. 2.2. Similarly, a resonant spectrum is also expected for the kinetic energy KER_{DR} of the atomic fragments A and B released in this reaction. In a real molecule, the situation usually will be much more complex than in this simple sketch of basic reaction mechanisms. In general, more electronic states of both the cation and the neutral molecule, as well as several vibrational states have to be taken into account. In many cases, the prediction of accurate cross sections by *ab initio* calculations and a detailed understanding of the reaction mechanisms involved is still a challenging task and subject to ongoing investigations. The resulting DR cross section $\sigma_{\text{DR}}(E_e)$ usually shows an overall $1/E_e$ dependence (cf. Eq. (2.1)) and a rich spectrum of additional structures depending on the detailed situation in the specific molecule.

Also shown in Fig. 2.2 is the process of dissociative excitation (green arrows). Here, the system is excited to a non-binding state of the cation and then dissociates in $A + B^+$. The

incoming electron leaves the molecule after the collision, thus capable of carrying an arbitrary amount of energy out of the system. The DE process therefore shows a non-resonant character, it is possible for any electron energy reaching or exceeding the transition energy to the excited $A + B^+$ curve.

A special case of particular astrophysical importance is the collision with an electron of near-zero relative energy, $E_e \approx 0$. In this case, no excitation energy is available. The DE process then is energetically excluded, while a DR reaction is still possible also in this case of a 'horizontal' transition where practically no additional energy is brought into the system by the incoming electron. The probability for a DR reaction to happen then depends on the actual relative position of the dissociative PES of the neutral molecule and the nuclear wave function of the original cation. Even in the example shown in Fig. 2.2, where the DR at $E_e = 0$ would be classically forbidden, a transition to the neutral PES would still be possible through tunnelling (indicated by the dotted blue arrow).

Besides this *direct* DR mechanism, which is characterised by a direct transition to the dissociative neutral state, an important additional process is the *indirect* mechanism, which proceeds via intermediate steps. This mechanism is of special importance in molecules where the direct process is inhibited by lack of a dissociative curve of the neutral system in the geometric region accessible from the cation, in particular at $E_e = 0$ as sketched in Fig. 2.3. In this case a slow electron can still be captured into an energetically near-degenerate high-lying Rydberg state of the neutral molecule (blue arrows). The system then cascades down to lower electronic states
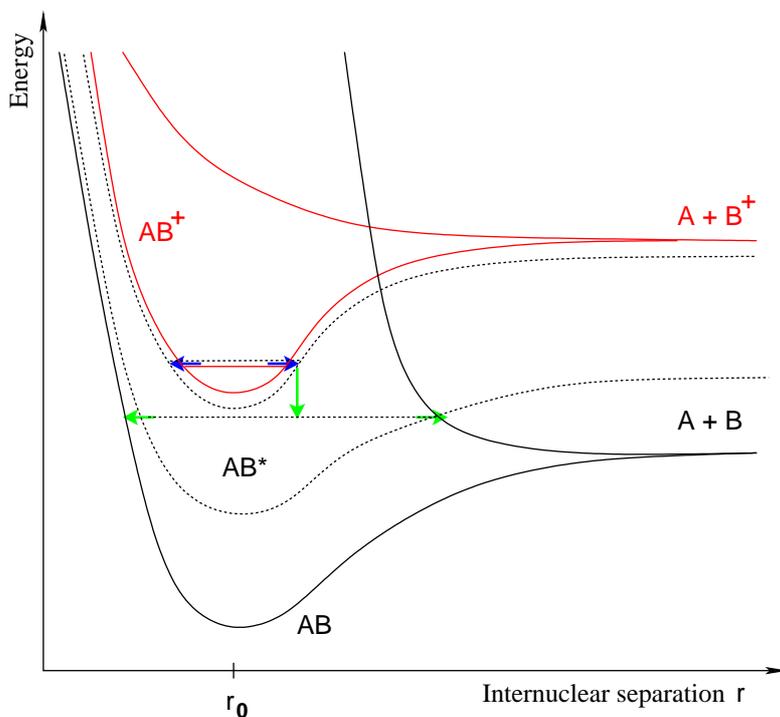
Fig. 2.3: *The indirect DR process. Black dotted potential curves represent Rydberg states of the neutral system. Blue arrows again indicate a transition involving electron capture (here for an electron energy of $E_e = 0$), green arrows depict a transition to another PES of the same system. See text for details.*

by transforming electronic energy into vibrational energy or by emitting photons (vertical green arrow), until it reaches a state with high probability of a transition to a dissociative curve (horizontal green arrows). Note that a crossing of the two curves is not necessarily needed, as such a transition can proceed also through the classically forbidden region between adjacent curves by tunnelling (left green arrow). For any molecular cation a series of Rydberg states exists, each of which gives rise to a number of vibrational levels. It is thus very likely to find one state close to the ground state of the ion, which makes this indirect mechanism a general phenomenon in the DR of molecular cations. However, it is often overruled when the much stronger direct DR process is possible.

In the example shown in Fig. 2.3, and commonly for most systems, the ground state of the neutral molecule is binding. However the production of the neutral molecule, that is an electron capture without dissociation, is in general not observed for molecular cations. The reason for this behaviour lies in the large energy difference between the cationic and neutral states, which reflects the potential energy of the free electron in the electric field of the cation. The dissociation limit of the neutral molecule thus usually lies energetically below the ground state of the cation, which allows for a dissociative recombination reaction even at vanishing electron energy, but on the other hand effectively inhibits a capture of the electron into a bound state of the neutral molecule. In other cases, like the H_3^+ molecule discussed in Chap. 4, the electronic ground state of the neutral system is dissociative and a neutral molecule does not exist.

In the case of polyatomic cations, the same principal mechanisms govern the DR process. However, the appearance of at least two additional degrees of freedom of the nuclear motion vastly complicates the picture. For an understanding of a particular reaction, the structures and possible transitions of multi-dimensional PES have to be studied here. Regarding the asymptotic behaviour of the PES for infinite separation of the fragments, in the diatomic case a simple level scheme corresponding to the electronic states of the two atomic fragments is obtained. For the breakup of a polyatomic ion, the final states can include also smaller molecules including vibrational and rotational degrees of freedom. In addition, the same PES can for large separation of the fragments possess minima at different geometries corresponding to different atomic and molecular compositions of the fragments.

This rich spectrum of new phenomena occurring for the DR of polyatomic cations is not only challenging for the theoretical treatment of such processes, but also calls for advanced experimental approaches, like for example an investigation of the dynamics on these multi-dimensional PES through an interpretation of the occurring fragmentation *geometries*. In the present work, experimental studies of the DR of the H_3^+ ion and its isotopomers will be presented. This reaction is of great interest both for astrophysical applications and as a benchmark

system for theoretical calculations, as will be discussed in Chap. 4. The present studies concentrate on the new aspects of fragmentation dynamics which come into play in the DR of polyatomic molecules.

2.3.2   Anions: Dissociative excitation and electron detachment

Electron impact on a molecular anion can, like for a cation, either result in a dissociation of the system without change of the total charge (*dissociative excitation*), or the molecule can be neutralised, in this case by *detachment* of an electron. While the dissociative excitation process has some similarities for anions and cations, the neutralisation reactions show fundamental differences for the two types of molecular ions.

The situation for dissociative excitation of a molecular anion is outlined in Fig. 2.4. As in the cation case, the anion is lifted to a higher electronic state and the colliding electron leaves the system with a reduced energy E_e'. This reaction can proceed either as a direct transition between the two anionic states (green arrows) or, for some molecules, by capture of the electron (blue arrow) into a dianionic, that is doubly negatively charged state (dotted magenta PES) [4]. In general, such states are very short-lived and the electron is released again (red arrow), leaving the system in a dissociative, singly anionic state. This process increases the reaction cross
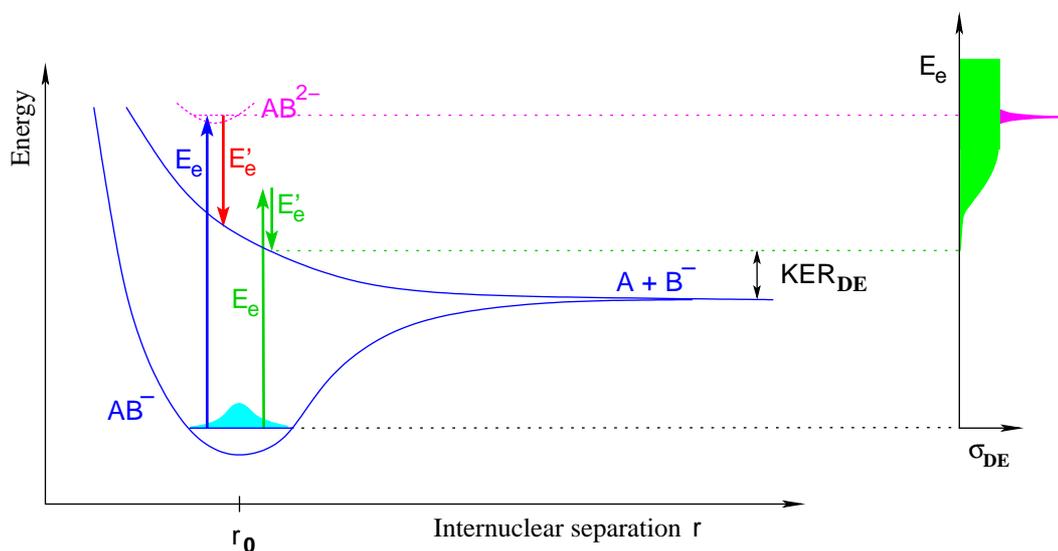
Fig. 2.4: *Dissociative excitation (DE) of a diatomic anion: Scheme of relevant potential energy curves of the anion AB^- (blue), and of a short-lived dianionic state (dotted magenta curve), which exists for some molecules. Green arrows show the direct transition to a dissociative PES, blue and red arrows the transition via temporary formation of a dianion involving the capture (blue) and auto-detachment (red) of an electron. In the right part of the figure the cross section σ resulting from the two contributions is outlined.*

section at the energetic position of the dianion and thus adds a sharp resonant structure to the energy spectrum $\sigma_{\mathrm{DE}}(E_{\mathrm{e}})$, depicted by the magenta peak in the right part of Fig. 2.4. (In a cationic system, a similar behaviour is possible if a bound state of the neutral molecule exists at a favourable energetic and geometric position.)

A difference to the cation system lies in the energy threshold for a DE reaction. To trigger an excitation of an anion, that is, to reach sufficient overlap with the bound electron to be excited, the incoming electron needs to overcome the Coulomb repulsion of the negative ion. While this is possible to a certain amount by tunnelling into this Coulomb barrier, the probability for a reaction strongly increases if the incoming electron has some excess energy available in addition to the energy needed for the actual excitation process. The *effective* energy threshold for any electron-induced reaction is thus shifted to higher energies for anions. In addition, the cross section is smeared out in the threshold region due to the smooth increase of both the probability that the incoming electron reaches a certain minimum distance to the anion, and the probability for exciting the anion at this distance. The schematic DE spectrum in Fig. 2.4 shows this modified threshold, shifted and flattened in comparison to the cationic case shown in Fig. 2.2.

The electron-induced neutralisation of an anionic molecule occurs by *detachment* of a bound electron through the collision with the free electron, see Fig. 2.5. In contrast to the resonant DR reaction neutralising cations, this process resembles the DE reaction. The two electrons emitted after the collision can carry away arbitrary amounts of energy and thus the cross section shows a threshold behaviour. Again any structure in the cross section expected from the possible transition energies is shifted to higher energies and smeared out due to the electronic Coulomb barrier and the quantum mechanical threshold law determining the probability for triggering a reaction. Also here, an additional resonant structure can appear due to the temporary formation of a dianion. The detachment reaction can in principle lead to both bound and dissociative states of the neutral molecule (see Fig. 2.5), thus a detachment with or without dissociation is possible here, in contrast to the cationic case. An overview of electron induced detachment from diatomic anions can be found in [58].

Like in the case of cations, moving on to polyatomic systems complicates the picture. The dynamics of the nuclear motion then is ruled by multidimensional PES, and the number of possible reaction products increases. The interest in molecular electron detachment reactions, besides the desire for a theoretical understanding of these fundamental processes, and some applications in plasma physics and astrophysics, is in the case of polyatomic molecules additionally strengthened by the possibility to access the transition regions of the PES governing neutral chemical reactions by electron detachment from the corresponding anion (see, e.g. [55] and references therein).
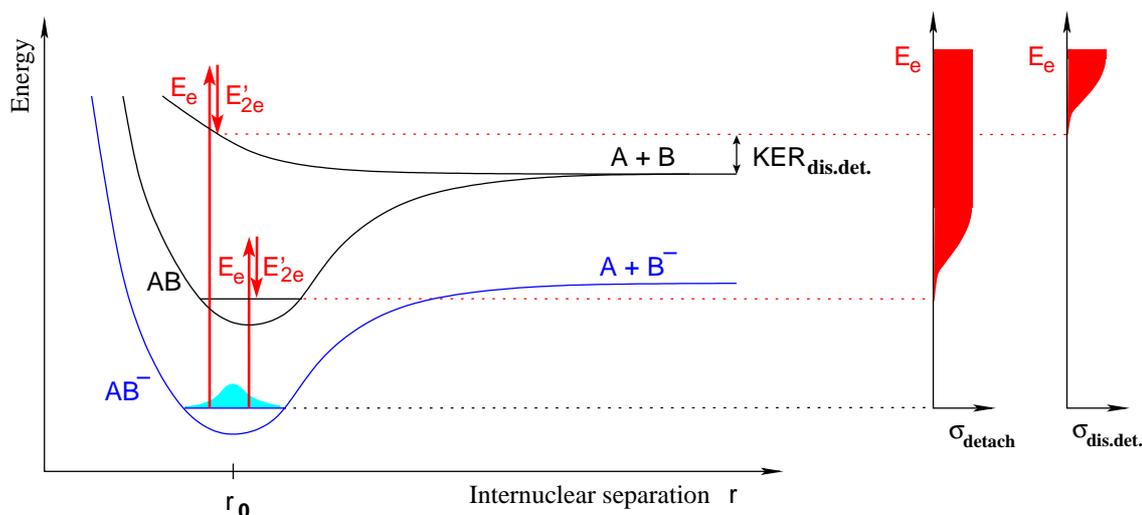
Fig. 2.5: *Electron detachment from a diatomic anion: Schematic drawing of relevant potential energy curves of the anion AB^- (blue) and the neutral AB (black). The detachment process can lead to a bound (right arrows) or dissociative (left arrows) state of the neutral molecule. In the right part of the figure the cross sections σ for detachment only and dissociative detachment are outlined.*

In this context, several experimental techniques exist, the most popular one being the preparation of the desired neutral transition state by photodetachment from the anion, in most cases combined with photoelectron spectroscopy as the detection scheme. With this technique, it is possible to investigate energy, population and lifetime of the accessible electronic and vibrational states of the neutral system. However, for geometrically unstable states, this method does in general not reveal the exit channel of the following dissociation process in terms of atomic and molecular composition.

In Chap. 5, an investigation of the breakup following electron impact detachment from LiH_2^- will be presented. This studies were done in a *fast beam* experiment, with the associated advanced possibilities of neutral fragment detection (see the next section). Particular emphasis is thus set on the identification of the final product channels of the fragmentation reaction, which was possible in this experiment.

3. Fast beam molecular fragmentation studies

The main advantage in using fast beams is the efficiency for the detection of reaction products, especially in the case of neutral fragments. In fast beam experiments at MeV or keV energies, the kinetic energy release of typical molecular fragmentation reactions is small compared to the beam energy. Thus the emerging fragments are concentrated in forward direction, which greatly simplifies the detection setups needed to collect all fragments. In addition, the high energy enables an efficient detection also of neutral fragments, which is usually not possible in low energy experiments.

Another benefit from high beam energies is the low rate of interactions with the residual gas in the vacuum system, which at low energies efficiently destroy the molecular ions. When using fast beams in combination with modern ultrahigh vacuum systems, it is thus possible to store molecular ions for typical time scales up to tens of seconds.

3.1   The ion storage ring technique

Heavy ion storage rings are successfully used in the field of molecular physics since about ten years. In this technique, the ions are accelerated to form a beam of MeV energy by means of heavy ion accelerators and confined in a closed orbit using magnetic fields. Despite some principal limitations, this technique offers several major advantages for studies of molecular fragmentation reactions, as summarised in the following.

In addition to the advantages offered by *fast* beams as given above, the use of *stored* beams, compared to single-pass techniques, opens up further possibilities. First, the long time the molecules are available for interactions strongly increases the probability that a given molecule will indeed undergo the fragmentation process to be studied. Thus a much larger *number of reactions* can be analysed for the same number of molecules produced, which offers new possibilities especially when studying processes with a low reaction rate. Second, the storage over several seconds enables a *relaxation of internal excitations* of the molecular ions which are often generated during the production process. For infrared active species, vibrational excitations decay radiatively on time scales of the order of milliseconds. A preparation of the molecules in

the vibrational ground state is thus possible here without a need for special efforts in the production and acceleration of the molecular ion beam. For relaxation processes on time scales up to tens of seconds, still an investigation of the implications of these excitations on the molecular properties under study is possible by time-resolved measurements.

Third, the use of an *electron cooler* offers further benefits. By merging an intense, co-moving beam of electrons of precisely defined velocity with the ion beam, the spatial and energetic spread of individual ion trajectories is reduced. In addition, interactions of the electrons with the molecular ions can be studied at well defined collision energies ranging from meV up to keV in the co-moving frame or reference. These interactions include electron-induced fragmentation reactions as well as a manipulation of the internal state of the molecules by electron collisions.

The technique of fast stored beams thus offers conditions well suited for studies, in particular including fragmentation studies, of molecular ions. Unfortunately the described methods cannot easily be extended to studies of neutral molecules. While the preparation of fast beams of neutral molecules in some cases is possible by acceleration of molecular anions and subsequent removal of an electron, the additional demand for stored beams requires the species under investigation to be charged. Another drawback is the inability to directly study chemical reactions in fast beams, that is, collisions of atoms or molecules at near-zero mutual velocities. This would require the preparation of co-moving fast beams of the reactants, which is again not possible for neutral species, and would imply a large technical effort also for ion-ion collisions at MeV energies.

For the wide field of interactions of molecular ions with photons or electrons, however, these limitations do not apply, and thus the advantages of the storage ring technique can be utilised in the studies presented in this work. As already noted, even chemical reactions of neutral molecules are indirectly accessible in fragmentation studies of molecular ions, as the dissociation into neutral atomic or molecular fragments following a reaction that compensates the electrical charge of a molecular ion is governed to some extend by the same mechanisms as the chemical reaction between these neutral species.

A schematic view of the general setup for studies of molecular fragmentation reactions in a storage ring is given in Fig. 3.1. A breakup of the stored molecular ions is induced for example by the interaction with a photon, an electron or by the collision with a molecule of the residual gas still present in the vacuum system. By use of detection systems mounted close to the storage ring, which record the emerging fragments, several properties of the reactions under study then can be analysed.
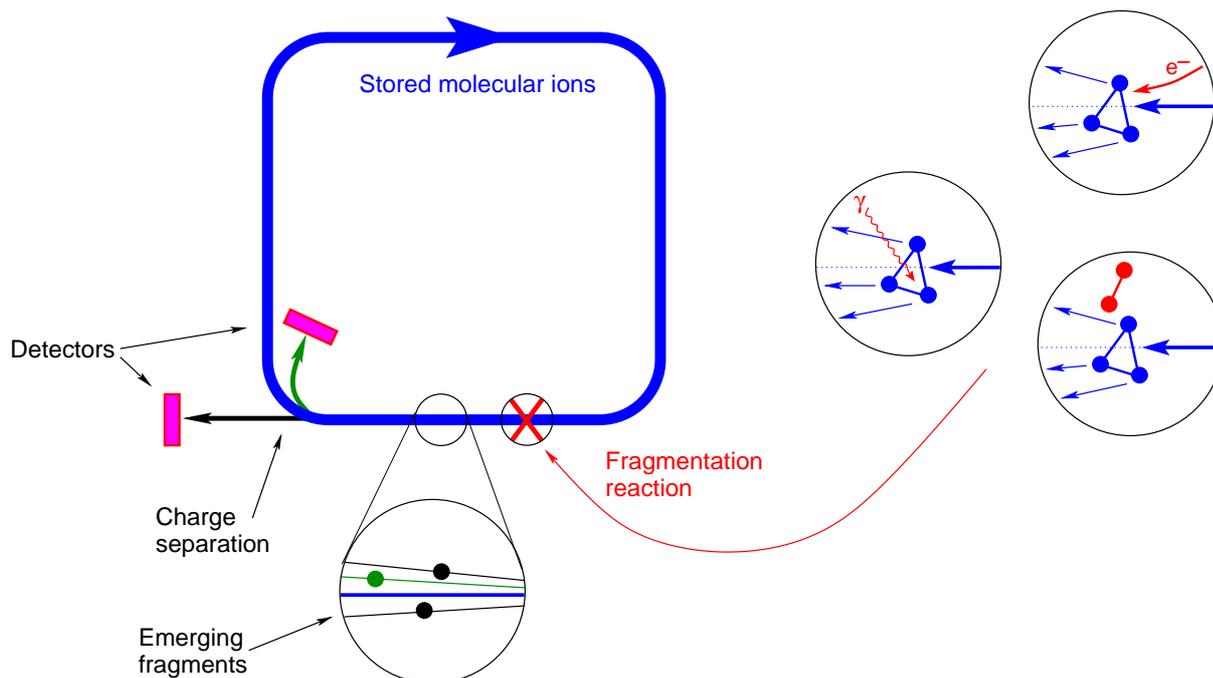
Fig. 3.1: *Schematic view of a storage ring. The products emerging from a fragmentation reaction are charge separated and recorded by different detectors. Three examples of specific fragmentation processes are given: The interaction with a photon γ, an electron e^-, and a residual gas molecule.*

3.2 Accessible properties of fragmentation reactions

In general, the fragmentation of a molecular ion can lead into several final channels. In the following, the term *channel* will be used to describe the outcome of a reaction in terms of the nuclear composition of atomic and molecular fragments, as well as the charge state of these fragments. Different internal excitations of the fragments will be denoted as the energetics within each channel. Using this definition, the properties of a molecular fragmentation reaction which can be accessed experimentally can be divided in the following classes:

- The total rate of the reaction. Usually, the *rate coefficient* α (in cm^3/sec) is given, which denotes the reaction rate per molecule, divided by the density of the reactant.

- The partial rate of each chemically different product channel or the relative branching ratios of the channels.

- The energetics of each channel. This includes any internal excitations of the fragments and the kinetic energy released in the breakup.

- In the case of a breakup into more than two fragments, an additional field of interest are the breakup dynamics as reflected by the geometry of the fragmentation.

The *total rate* can in principle be measured by a particle counting detector without any differentiation of channels. However, it might be advisable to include a certain ability of channel separation for suppression of background events. This is especially the case if the total rate measured would include channels that are only populated by background processes. Such processes can for example be collisions of the molecular ions with residual gas particles, which cannot be completely avoided even in ultrahigh vacuum systems. These background data have to be either separated from the data originating from the physical process under study on an event by event basis, or, if this is not possible, the ratio of background events as well as their signature in the properties studied have to be estimated and considered in the interpretation of the data.

Fortunately, the experimental setup at a storage ring necessarily already includes some means of channel separation, as indicated in Fig. 3.1. The magnetic dipole fields needed to keep the original beam on a closed orbit will geometrically separate different fragments according to their charge to mass ratio. This implies the need for several detectors, if fragments at all possible charge states should be detected. The reaction channels of interest often involve only neutral fragments, while charged fragments are only produced by unwanted background processes. In this situation, it is sufficient to use only one, but energy resolving detector for counting of neutral fragments. By limiting the analysis to events where the whole beam energy was deposited in this detector, breakup reactions involving charged fragments are excluded.

The measurement of *partial rates* or branching ratios requires a separation not only of 'signal' from 'background' channels but also of all signal channels with different product composition from each other. If charged fragments are involved, movable particle counting detectors can be used to probe for fragments of different charge to mass ratios. However, for the separation of different neutral channels, a dedicated detection system is required.

Next, the *energetics* of each channel can be investigated using an imaging detector. From the recorded spatial pattern of impact positions on the detector, information on the relative velocities of the fragments, and therefore on the kinetic energy transferred to each of the fragments during the dissociation process can be deduced. A measurement of this kinetic energy release often can provide information on the internal excitation of the fragments or of the incoming molecular ion.

In the case of polyatomic fragmentation reactions, a new property to be studied is the *geometry* of the breakup. From the fragmentation geometry, in particular the correlation of individual fragment energies can be studied, which is connected to the shape of the multidimensional potential energy surface driving the dissociation process. To shed more light on this aspect, which is specific to the fragmentation of polyatomic molecules, is one of the goals of this work.

All properties listed here can in principle be recorded as a function of the initial conditions of the molecular reaction. This is first of all the relative kinetic energy between the reactants, but also the internal state of the molecular ions, regarding e.g. rovibrational excitations.

As noted in Chap. 2, the specific experiments considered below focus on molecular fragmentation reactions induced by *electron impact*. The experimental techniques applied for initiating such reactions in a storage ring, as well as the detection systems available for analysing the properties of these reactions are described in the following. As seen here, important detection techniques are (a) neutral fragment imaging, where a good sensitivity to the impact positions of the fragments is needed, and (b) rate measurements employing an highly efficient, energy resolving detector. In addition, a strategy for determining the partial rates of different neutral channels is desirable.

3.3 Experimental procedures

3.3.1 The heavy ion storage ring TSR

All experiments described in this work were performed at the Test Storage Ring (TSR), which is in operation since 1988 at the Max-Planck-Institut für Kernphysik in Heidelberg, Germany [25]. A drawing of this heavy-ion storage ring is shown in Fig. 3.2. Various combinations of ion sources and accelerators are available for the production of fast molecular ion beams (typical energies $\sim$1 MeV per nucleon), which are then injected into the TSR and stored at a vacuum of $\sim 3 \cdot 10^{-11}$ mbar for times ranging up to several tens of seconds.

While different types of ion sources were used for production of molecular cations and anions, respectively, all experiments considered here employed the HSI system for acceleration of the ions. The HSI (Hoch-Strom-Injektor, High Current Injector) is a modular acceleration system consisting of two RFQ (Radio Frequency Quadrupole) resonators for simultaneous acceleration, focusing and bunching of the ion beam, and eight 7-gap resonators for further acceleration [79]. Depending on the number of modules used, beam energies ranging from 0.24 MeV up to 1.7 MeV per nucleon of the accelerated species can be achieved here.

After acceleration to the desired energy, the ion beam is guided to the storage ring. Using a multiturn injection scheme [8], currents of stored molecular ions ranging up to several μA are achieved, allowing imaging experiments even after storage times of several multiples of the beam lifetime.

In the *electron cooler* device of the TSR (see Fig. 3.2), the circulating ion beam is merged over a length of 1.5 m with a co-moving beam of cold electrons. The interaction between the two beams serves two purposes in the experiments considered here: Firstly, by elastic collisions of the (stored) ions with the (single-pass) electrons, a *phase space cooling* of the ion beam is
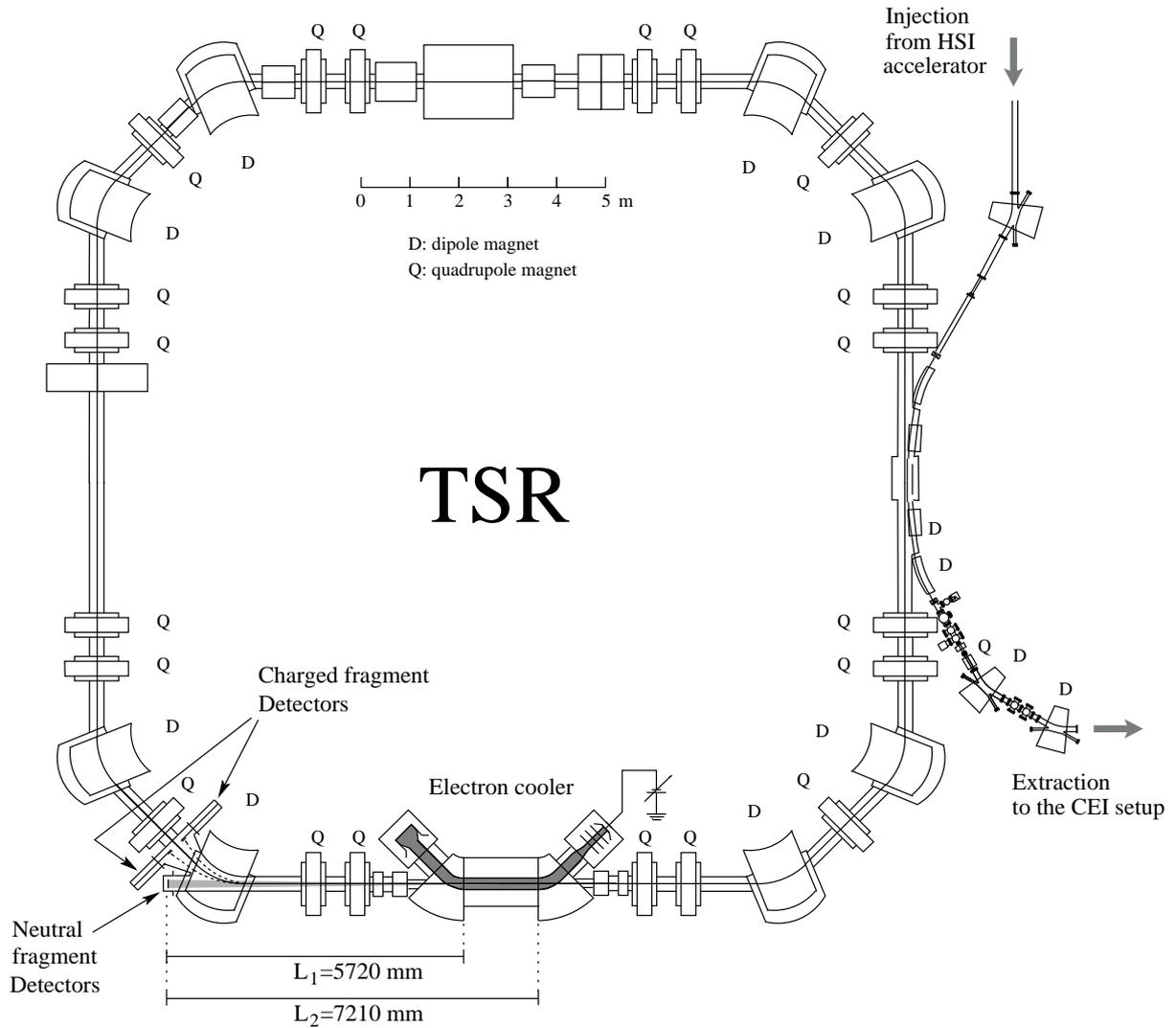
Fig. 3.2: *The Test Storage Ring TSR with electron cooler and fragment detectors.*

achieved [7]. After a cooling time of typically few seconds, the velocity of the ion beam is determined by that of the electron beam. Even more important, the spread of individual ion velocities, as expressed by the temperature connected to their kinetic energy in a co-moving frame of reference, approaches the temperature of the electron beam.

The electrons are produced by a thermal cathode, whose temperature of typically $kT_{\mathrm{cat}} \approx 110\,\mathrm{meV}$ determines the initial electron temperature. Through the acceleration to the ion beam velocity, the electron temperature in the longitudinal degree of freedom (that is, parallel to the ion beam) is reduced to a typical value of $kT_{\|} \approx 0.1\,\mathrm{meV}$. The transversal electron temperature is reduced by an *adiabatic expansion* of the electron beam in a decreasing magnetic guiding field to the order of $kT_{\perp} \approx 10\,\mathrm{meV}$. The electron beam typically has a radius of $\sim 1\,\mathrm{cm}$ and an electron density of $\sim 3 \cdot 10^6\,\mathrm{cm}^{-3}$.

Through the phase space cooling process, the relative energy in electron-ion collisions is reduced to values determined by the temperatures $T_\parallel$ and $T_\perp$. In addition, the geometrical extension of the ion beam is reduced, reaching a radius of below 1 mm in the electron cooler region. As already noted, this clean preparation of the conditions in the interaction region constitutes one of the advantages of the use of fast stored beams in fragmentation experiments.

The second purpose of the merged electron beam is to provide the electrons needed for investigations of electron induced reactions of the molecular ions. Depending on the specific problem under study, either electron and ion beams at matched velocities can be used, resulting in very low collision energies, or the acceleration voltage of the electrons can be changed after completion of the phase space cooling, allowing for a study of electron-induced fragmentation processes as a function of the relative electron energy. A more detailed description of the electron cooler device and its application in molecular fragmentation experiments can be found in [39] and references therein.

The *neutral* atomic and molecular fragments emerging from a reaction at the electron cooler region usually reach their asymptotic velocities $\sim 1~\mu$m downstream from the point of the dissociation, after gaining mutual distances large enough to exclude further interaction between the fragments. They then travel on straight trajectories close to the direction of the stored ion beam until reaching the next dipole magnet, where a charge separation takes place. While undissociated molecular ions are deflected by the magnet to follow the closed orbit, neutral fragments stay unaffected by the magnetic field and thus leave the storage ring finally arriving with macroscopic mutual distances at a dedicated vacuum chamber equipped with two different detection systems. First, a multi-hit imaging detector can be used for determining the geometry of the breakup, and second, a solid state detector is available for rate measurements. These systems are described in detail in the following sections.

If *charged fragments* are produced in the dissociation reaction, they undergo further deflections in external fields and in particular different deflections in the magnetic field of the bending dipoles depending on their charge to mass ratio. Fragments with a charge to mass ratio close to that of the original molecular ion can be recorded using movable particle counting detectors located after the bending dipole close to the stored beam trajectory. At the TSR, two such detectors are available. In molecular fragmentation experiments, usually only one of them is used for observation of singly charged fragments containing a large fraction of the mass of the original molecule. Fragments with a very small mass fraction (like single protons) or fragments with opposite charge compared to the stored molecular ions cannot be observed due to the geometry of the present setup. In the studies described here, a charged fragment detector was only used in the case of the experiments with LiH_2^-, a description is given in Sec. 5.2. Since the charged fragments also feel the focusing fields of the storage ring quadrupole magnets, their trajecto-

ries do only indirectly reflect the fragmentation geometries. Imaging measurements of charged fragments thus, if feasible at all, would require very complex evaluation procedures and were not applied here.

Drawn in Fig 3.2 is also the *slow extraction* facility, which allows a small fraction of ions to be continuously extracted from the stored beam in the TSR. These extracted ions are then guided to the Coulomb Explosion Imaging (CEI) setup, where the geometrical structure of the molecular ions can be analysed. In combination with the slow extraction from the storage ring, this provides a tool for the examination of vibrational excitations of the ions as a function of the storage time. Details on the principle of the CEI method and its implementation at the TSR can be found at [75, 81].

In the following, the detector arrangements used for the neutral fragment imaging experiments and for the determination of total and partial rates will be considered.

3.3.2 Fragment imaging measurements

The principle of the neutral fragment imaging detector is visualised in Fig. 3.3. As an example, the fragmentation of a diatomic molecular ion $AB^{(\pm)}$ into the neutral fragments A and B is shown. At the point of dissociation, the molecular ion is travelling at the beam velocity $\vec{v}_{\mathrm{beam}}$ and with an internal geometry that can be described e.g. by the distances r_A and r_B of the two nuclei from the center of mass (c.m.) of the molecule.[1] Through the dissociation process, each fragment gains a certain amount of kinetic energy E_i ($i = $ A, B) corresponding to an asymptotic velocity $\vec{u}_i$ in the co-moving c.m. frame of the molecule:

$$E_i = \frac{1}{2} m_i u_i^2 , \qquad (3.1)$$

with m_i the mass of fragment i and $u_i = |\vec{u}_i|$. The orientations of the velocity vectors $\vec{u}_i$ are determined by the orientation of the original molecule and by the dynamics of the fragmentation process. Momentum conservation here sets the restriction $\sum_i m_i \vec{u}_i = \vec{0}$.

The fragments thus move at total velocities $\vec{v}_i = \vec{v}_{\mathrm{beam}} + \vec{u}_i$ in the laboratory frame of reference until hitting the imaging detector after a flight distance L. At the impact time of the first fragment, the distances of the fragments to the c.m. have grown to macroscopic values D_i

$$D_i = \frac{u_i}{v_{\mathrm{beam}}} L . \qquad (3.2)$$

This results in impact positions on the detector surface described by the 2D projected distances R_i, as well as different impact times t_i for each of the fragments. In the experiments considered

---

1 For the description of a diatomic molecule, the internuclear distance r_{AB} would be sufficient. However, the formalism used here is easier to extend to polyatomic molecules.
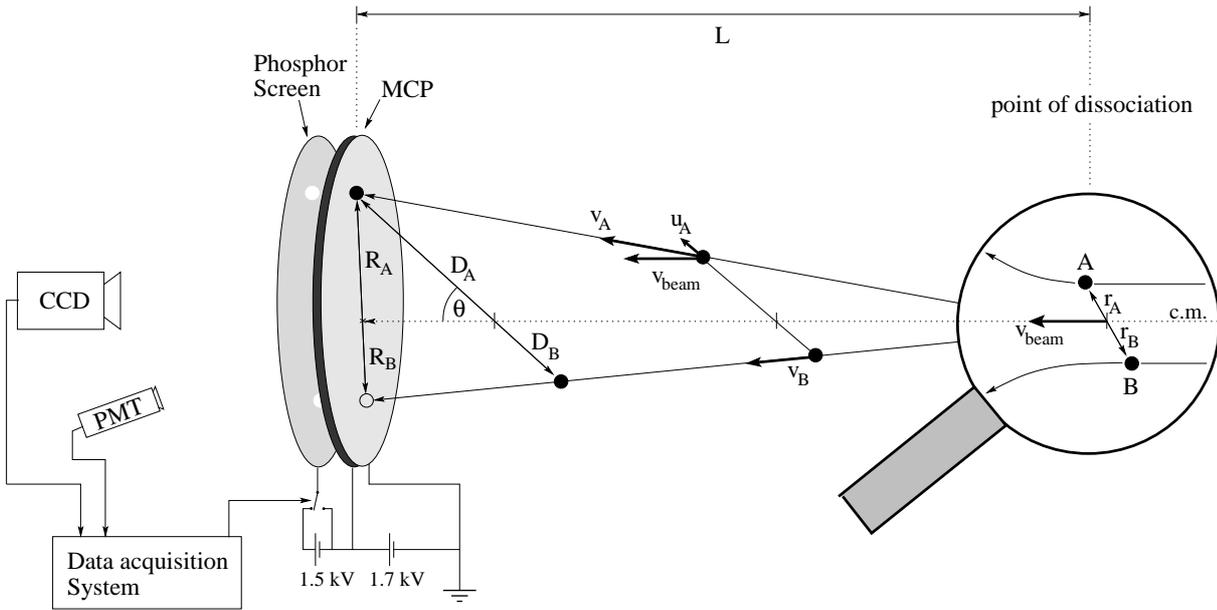
Fig. 3.3: *Schematic overview of the neutral fragment imaging system.*

here, the fragment distances occurring are much smaller than the total flight length, $D_i \ll L$. The relation of the 3D distances D_i and the projected quantities R_i and t_i can thus be approximated by a orthogonal projections of the 3D distance into the detector plane and on the beam axis,

$$R_i \; = \; D_i \, \sin \theta \,, \qquad t_i \; = \; D_i \, \cos \theta / v_{\text{beam}} \,. \tag{3.3}$$

Typical values here are projected distances of few centimeters and impact time differences of few nanoseconds.

As detailed in [3], the imaging detector itself consists of a *multi channel plate* (MCP) detector with an active area of 75 mm diameter and an attached phosphor screen. On impact of an MeV particle, an electron avalanche is created in the MCP and further accelerated to the phosphor screen where it creates a light spot. The position of this light spot is then recorded by a CCD camera located outside the vacuum system. Different cameras with a readout frequency of up to 1 kHz can be used. However, the rate of fragmenting molecules arriving at the detector can be up to the order of 10 kHz. Thus, the desired analysis of individual breakup geometries requires special precautions to avoid a recording of fragments stemming from different molecules in the same camera frame.

For this purpose, an additional photo multiplying tube (PMT) is included in the system, which creates a fast electronic signal on the appearance of a light spot on the phosphor screen. This signal is then used to switch down the voltage between the MCP and the phosphor screen, thus turning the detector blind for any further incoming particles. As the switching off time is

of the order of $1\,\mu$s, the fragments which stem from the same molecule as the one triggering the PMT and thus arrive within some nanoseconds, are not affected by the switching. On the other hand, fragments of the next dissociation event arrive after a time of typically hundreds of μs and find the detector blind.

After readout of the image from the CCD camera, the phosphor screen is switched back to high voltage. To avoid an immediate trigger signal from the PMT caused by electronic noise connected to the fast high voltage switching, a dead time of $20\,\mu$s was implemented, where a trigger signal from the PMT is not accepted. This dead time introduces a certain probability, depending on the actual event rate, of recording fragments of two dissociating molecules in the same camera frame. For the vast majority of the recorded events, however, this method allows the determination of impact positions of the fragments on a single molecule basis.

The images taken by the CCD camera are then processed by a frame-grabber connected to a VME computer, which analyses the table of light intensities per camera pixel obtained from the frame grabber and produces a list of fragment positions. These positions are at first expressed in units of camera pixels. By a dedicated calibration measurement the conversion factor to the fragment positions in mm is then obtained. For this calibration, a beam stop is moved in front of the imaging detector covering part of its active area. From the correlation of the measurable position of the beam stop (in mm) and the position of the 'shadow' observed by the imaging system (in pixels), the desired conversion factor is obtained.

Some important limitations of the detection system should be noted here, which have to be taken into account in the data analysis procedure. First, the imaging detector described here is not capable of recording the individual impact times of the fragments. Only the impact positions in the detector plane can be determined, which puts a major restriction on the possibility of reconstructing fragment velocity vectors. Second, the point of dissociation and thus the flight length L is not well defined. Electron induced fragmentation reactions as considered here can occur at any point inside the interaction region in the electron cooler. As seen in Fig. 3.2, this region has a length of $1.5\,$m which puts only a weak limitation on the actual flight length L. Third, the efficiency of the MCP is only in the order of $\sim 50\%$. Thus, in many of the dissociation events recorded, only a part of the fragments is seen. This limitation has to be considered especially when dealing with polyatomic molecules, as discussed below.

In addition, it has to be kept in mind that the imaging system generally is not able to determine the masses of the impinging fragments. As will be seen in the following, this limitation does not affect the analysis of imaging data from the fragmentation of diatomic molecules, which is a standard application of the detector setup available at the TSR [3]. Regarding the case of polyatomic molecules, which will be particularly addressed in the present work, the assignment of fragment masses is one of the problems to be solved in the analysis of imaging data.

Analysis of imaging data

As shown by Beckert and Müller [6], even for a mass-insensitive imaging detector a complete and accurate reconstruction of the fragment velocities $\vec{u}_i$ can in principle be performed, event by event, for an arbitrary number of fragments, given that certain conditions are fulfilled regarding the measured quantities, the preparation of the molecular beam, and the initiation of the dissociation process. These conditions include a 3D determination of both impact positions and impact times of the fragments on the detector, an accurately known flight length L and a good definition of the interaction region also transversal to the beam direction. In the setup considered here, these conditions can be fulfilled in some, but not all aspects. In particular, the use of a 2D imaging system not capable of determining the impact times of the fragments, and the unknown position of the point of dissociation within the electron-ion interaction region, inherent to the merged beams geometry, make it impossible to fully reconstruct the dissociation geometry from the measured data on an event by event basis.

However, a straightforward data analysis procedure exists for the simple case of the electron-induced fragmentation of diatomic molecules, which is able to extract considerable information on the dissociation dynamics from the limited data available. For neutral fragment imaging applied on the breakup of a diatomic molecule, the only channel of interest is the production of two neutral atoms, while background processes like the dissociative excitation through a residual gas collision in general produce at least one charged fragment. Thus, the simple requirement of a detection of two coincident fragments efficiently suppresses a contamination of the data stemming both from different fragmentation processes and from incomplete detection of the neutral fragments.

The only reaction property to be analysed for a diatomic breakup is the total kinetic energy release E_{kin}; the sharing of this energy among the two fragments is given by momentum conservation. Following Eqs. (3.1)–(3.3), this energy release translates into a distance $R = R_{\text{A}} + R_{\text{B}}$ of the light spots seen on the detector. As the angle θ and the flight length L are not measured, a back-calculation of E_{kin} from the measured R is not possible. However, the probability distribution $P(R)$ of impact distances accumulated for many individual fragmentation events can be compared to the distribution expected for a given E_{kin} under certain assumptions.

In particular, one assumes that the dissociation takes place (a) with equal probability over the whole interaction region, that is $P(L) = \text{const.}$ for $L_1 \leq L \leq L_2$ and (b) with an isotropic orientation of the dissociating molecule, that is $P(\cos\theta) = \text{const.}$ for $-1 \leq \cos\theta \leq 1$. Both assumptions are well justified especially in the case of zero energy of the colliding electron, where no special orientation of the molecule can be defined by the relative electron velocity vector. Using these assumptions, the $P(R)$ spectrum expected for a certain energy release E_{kin} can be expressed by an analytic function, as sketched in Fig. 3.4. The experimental $P(R)$
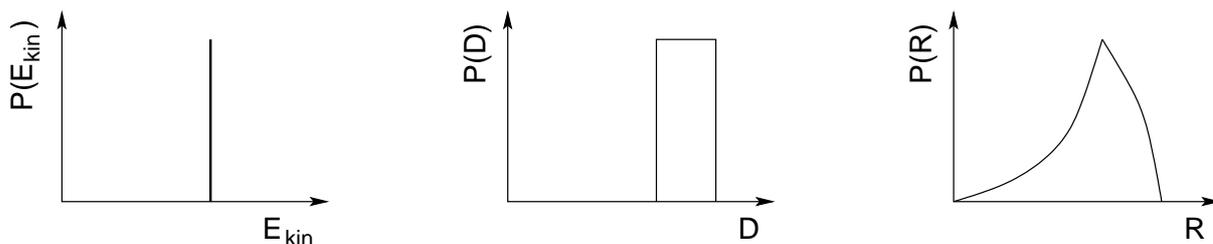
Fig. 3.4: *Sketch of the probability distributions resulting from a diatomic fragmentation reaction. The fixed energy release E_{kin} (left) translates to a rectangular distribution of 3D fragment distances $P(D)$ (center) due to the variable flight length L. The distribution of projected distances $P(R)$ (right) is additionally broadened through the isotropic orientation of the molecule.*

spectrum can then be fitted by a sum of these functions for different E_{kin}, thus yielding the probability distribution $P(E_{\text{kin}})$ of the breakup energy. A detailed description of this method can be found in [3].

Extension to studies of polyatomic molecules

In the last section, the standard methods used in fragmentation imaging studies with diatomic molecular ions have been outlined. For studies of polyatomic breakup reactions, these methods have to be modified in several aspects. A major complication in the fragmentation of polyatomic systems is the appearance of additional reaction channels, which require the application of advanced methods of channel identification in both imaging experiments and also the rate measurements discussed below, to allow a channel-resolved investigation of the properties of the dissociation process. Another new issue is the analysis of imaging data taken for a channel employing more than two fragments. The geometric information encoded in the recorded impact positions in this case is multi-dimensional, thus complicating the representation and interpretation of these data.

Both the channel identification and the representation of multi-fragment imaging data are connected to the basic problem of the assignment of masses to the fragments of each recorded event. As will be seen, this mass assignment can be done by a careful inspection of the center of mass of the observed fragments. Shortly, the well defined orbit of the molecular ions in a storage ring results in a well defined 'impact' position of the c.m. of all dissociating molecules on the surface of the imaging detector. Thus, the best mass assignment for an observed event can be found by comparing the c.m. position calculated for several tentative assignments to the known c.m. position of the beam. Together with a strict cut on the position of this best possible c.m., this method also yields an identification of the fragmentation channel for each event, as well as a suppression of different types of background.

The mass assignment found this way can further be used in the interpretation of imaging

data from multi-fragment channels, where it allows a study of the kinetic energy gained by each fragment during the breakup process. As will be shown, the sharing of kinetic energy between the fragments represents a well suited basis for the interpretation of the observed fragmentation geometries.

Being the simplest example of a polyatomic fragmentation process, the breakup of triatomic molecular ions will be addressed in this work. While these reactions are still much simpler than the fragmentation of larger systems, some important qualitative changes in the data analysis, compared to the case of diatomic fragmentation, can be investigated already in triatomic systems. As an example for the analysis of neutral fragment imaging data from a triatomic molecule, dissociative recombination experiments on H_3^+ and its isotopomers will be studied in Chap. 4, where the mentioned methods of channel separation and data representation will be discussed in detail.

3.3.3   Total and partial rate measurements

For measurements of the rate of *neutral* fragments emerging from the electron cooler, a silicon surface barrier detector can be positioned in front of the imaging detector described above. It is used here to determine both the total and the partial rates of the various breakup channels, in particular for the fragmentation studies on the LiH_2^- anion.

In contrast to the imaging system, this solid state detector has a 100% efficiency for the detection of neutral particles at MeV energies and is thus suited for determining absolute count rates. In addition, this detector is sensitive to the total energy of the impinging fragments, which are completely stopped within the active area of the detector. As the velocities of all fragments are in good approximation identical to the velocity of the stored beam, this energy resolution can be used to determine the mass deposited at the neutral fragment detector for each dissociation event. Due to the short time interval between the impact of fragments stemming from the same molecule ($\lesssim 10\,\mathrm{ns}$), only the total mass of all neutral fragments can be recorded. On the other hand, the typical time between two separate dissociation events is of the order of $\gtrsim 100\,\mu\mathrm{s}$ and thus large enough for a clean separation of individual events.

A typical energy spectrum as recorded for electron-impact fragmentation of LiH_2^- is shown in Fig. 3.5. The peaks corresponding to the impact of a total neutral fragment mass of 1, 2, 7, 8 and 9 a.m.u. are easily identified and well separated. The additional peak at the low-energy end of the spectrum (ADC channel 20–30) is generated by electronic noise and could be suppressed by setting a threshold on the signal amplitude. The small peak around ADC channel 100–110 is an artefact stemming from the geometry of the solid state detector. The active area of this detector is divided into seven vertical stripes with a width of $\sim 9\,\mathrm{mm}$ and a distance of $\sim 0.2\,\mathrm{mm}$. These stripes can be read out individually, a feature that was not used in the present
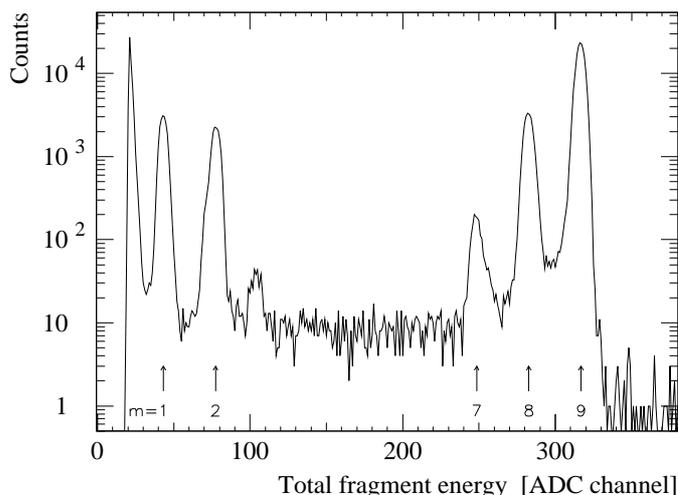
Fig. 3.5: *Typical energy spectrum recorded by the solid state detector. Arrows indicate the neutral fragment masses (in a.m.u.) assigned to events recorded with the respective energies. The spectrum was recorded for impact of 41.3 eV electrons on LiH$_2^-$.*

experiments. For fragments hitting the small spacing between adjacent active stripes ($\lesssim 1\%$ of all fragments), only a fraction of $\sim 10\%$ of the fragment energy is recorded by the detector. The mentioned peak thus corresponds to the detection of a mass of ~ 2.7 a.m.u., where a Li atom is only partly seen. In the experiments considered here, this property of the solid state detector has to be taken into account in the data analysis as a systematic error.

As seen here, the detector is able to identify the total mass of the impinging fragments, but it is not sensitive to their chemical composition. In the case of LiH$_2^-$, e.g., a total mass of 9 a.m.u. could be made up by the fragments Li + H + H, LiH + H, Li + H$_2$ or LiH$_2$. To distinguish between these channels, additional efforts are required, as discussed below.

Beside the neutral fragment detectors, an additional detector sensitive to *charged* fragments is available. As detailed in Sec. 5.2, this device is capable of measuring count rates for several types of charged fragments. An imaging setup for charged fragments is not available, as noted above.

Determination of branching ratios: The grid method

To separate dissociation channels which exhibit the same total mass of neutral fragments, a special approach is necessary. In many cases, the *grid method* described in the following can be used to determine the branching ratios of such channels, as demonstrated already in 1971 by Morgan *et al.* [52] and applied also in [77, 58, 19, 18]. The detector setup at the TSR was thus equipped with a ladder holding various grids for the experiments on LiH$_2^-$. Details of the particular setup used will be given in Sec. 5.2.

For an overview of the grid method, the simple case of the fragmentation of a diatomic molecular ion AB$^{(\pm)}$ is again chosen as an example here. Assuming that the observed fragmentation can lead to two channels, AB and A + B, the mass spectrum recorded by the solid
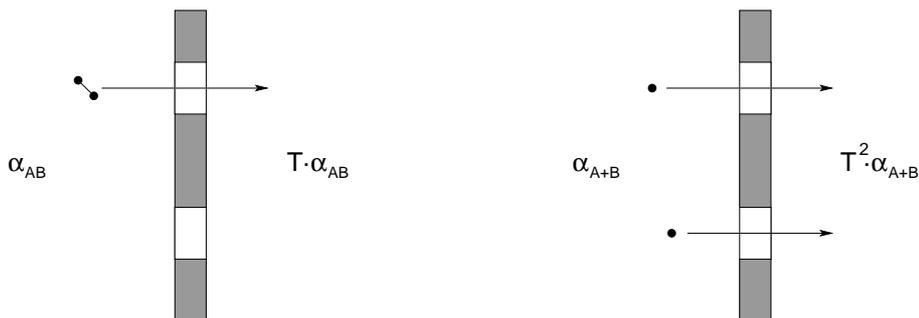
Fig. 3.6: *Visualisation of the two processes contributing to Eq. (3.4a).*

state detector will exhibit a single peak corresponding to an impact of the total mass m_{AB} of the molecule. The aim of the measurement is to determine the fractions α_{AB} and α_{A+B} of the two channels, which are normalised e.g. to $\alpha_{AB} + \alpha_{A+B} = 1$. The idea of the grid method is now to put a metal grid in front of the solid state detector which reduces in a well defined way the detection probability for each individual fragment. To achieve this, a material is chosen which can completely stop all types of fragments emerging from the reaction under study. The transmission probability T of the grid is given by the size and the distance of microscopic holes. The length scale of this pattern has to be smaller than the expected distances of the fragments to ensure an independent stopping probability for each fragment.

The mass spectrum recorded by the detector with this grid in place will then show a reduction of the full mass peak, and at he same time an appearance of additional peaks corresponding to the masses m_A and m_B of the individual fragments. The resulting count rates P_m in the peaks of mass m are given by

$$P_{m_{AB}} \;=\; N\left(T^2\,\alpha_{A+B} \;+\; T\,\alpha_{AB}\right) \tag{3.4a}$$

$$P_{m_A} = P_{m_B} \;=\; N\,T(1-T)\,\alpha_{A+B} \tag{3.4b}$$

with a normalisation factor N. (See also the schematic drawing in Fig. 3.6.) Using the the known transmission factor of the grid, these equations can easily be solved yielding the desired branching factors α_{AB} and α_{A+B}.

The accuracy of the resulting α values can in some cases sensitively depend on the exact value of the transmission T. In particular, the method is based on the assumption, that the same transmission factor T is valid for all types of fragments impinging on the grid. However, in [77] transmission measurements on grids of similar type as the ones used in the present work were reported to show small variations of the transmission factor dependent on the type of atoms used as projectiles. As the reason for these variations is unclear at present, this observation has to be taken into account as a possible source of systematic errors in the reconstruction of branching factors.

Extension to studies of polyatomic molecules

When extending these measurements of partial rates to polyatomic molecules, the increased number of dissociation channels in such systems bears an increased number of unknown variables α_i in the equations which correspond to Eq. (3.4) in the diatomic case. Thus, additional independent data in general are required for a determination of these α_i.

In the measurements of the DR of H_3^+ described in [19], Datz and coworkers collected additional data by using a 'translucent barrier'. Here the particles hitting the grid material were not completely stopped (due to the high beam energy applied), but rather lost part of their energy giving rise to a number of additional peaks in the fragment energy spectrum. Still, this method could not be used in the case of LiH_2^-, which will be considered here, since these additional peaks, which are also broadened due to inhomogeneities of the grid thickness, could not be resolved in a reaction involving fragments of too different masses.

Instead, another extension of the grid method was applied, which was not reported so far, namely the combination of several measurements using grids of different transmission factors T. However, an algebraic solution of the resulting extended system of equations, which would yield exact values for the branching factors α_i, is not in all cases possible, even when using several different grids. This is especially the case for molecular anions, where the situation is further complicated by a considerable background contribution in several channels originating from residual gas collisions. In this situation, additional considerations are necessary to gain information on the branching factors. For example, the fact that all α_i have to be non-negative can be used to obtain at least upper and lower limits for all channels.

In Chapter 5, experimental results on the fragmentation of the LiH_2^- anion are presented. For this system, the focus is set on the investigation of branching ratios. Even though a straightforward derivation is not possible here, approximative values could be obtained, which allow a clear identification of dominant channels.

4. Dissociative recombination of H_3^+ and its isotopomers

4.1 General background

The simplest polyatomic molecule is the triatomic hydrogen ion H_3^+. Its breakup into neutral fragments following dissociative recombination (DR) with low-energy electrons is therefore a natural test case for studying polyatomic fragmentation. In addition, the H_3^+ DR is of great interest in many fields ranging from fundamental quantum chemistry to applications in astrophysics and plasma physics, as will be briefly outlined in the following.

4.1.1 Properties and interactions of H_3^+

The triatomic molecular hydrogen cation H_3^+ was discovered 1911 by J.J. Thomson in a laboratory hydrogen discharge. While viewed as an exotic molecule with completely unclear binding mechanism for many years, the structure of H_3^+ is nowadays well investigated. Theoretical calculations of the ground-state potential energy surface (which is the only binding one) have reached a high level of accuracy [63, 13, 31] and the resulting spectroscopic properties are in very good agreement with laboratory spectroscopy measurements [54, 47]. The geometrical equilibrium structure, an equilateral triangle with a side length of 1.65 bohr, was in addition confirmed directly applying the Coulomb Explosion Imaging (CEI) technique [22], which was also used recently to study the relaxation of vibrational excitations of H_3^+ [38].

Since the early 1960's, H_3^+ was expected to be abundant in the hydrogen-dominated medium in interstellar space. Starting 1973 [29], it gained a central position in models of interstellar clouds. As an efficient proton-donator, it plays an essential role in the formation of larger molecules. The first observation of H_3^+ in interstellar space however took until 1996 [24]. Because of the lack of both electronically excited states and a permanent dipole moment which could give rise to allowed rotational transitions, a detection was possible only through a search for vibrational transition lines in the infrared range. Today, H_3^+ is known as an important constituent not only of both dense and diffuse interstellar clouds but also in different environments

like the ionosphere of Jupiter and other planets or the periphery of nuclear fusion plasmas [30].

The molecule is produced in the reaction

$$\mathrm{H_2^+ + H_2 \;\rightarrow\; H_3^+ + H \quad + 1.7\,eV}\,. \tag{4.1}$$

The destruction mechanism depends on the actual environment. While in dense interstellar clouds reactive collisions with other molecules like CO dominate, the main destruction mechanism in diffuse interstellar clouds, and thus the reaction crucially determining the abundance of $\mathrm{H_3^+}$ in these environments, is the dissociative recombination with low-energy electrons:[1]

$$\mathrm{H_3^+ + e^-} \rightarrow \begin{cases} \mathrm{H + H + H} & + & \Delta E^{(3)} \tag{4.2a} \\[2mm] \mathrm{H + H_2} & + & \Delta E^{(2)}\,. \tag{4.2b} \end{cases}$$
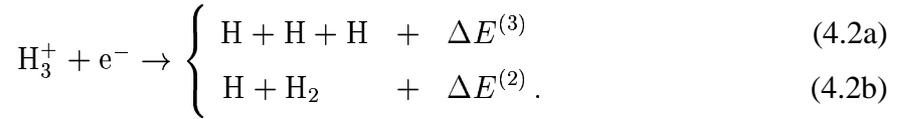
The study of this reaction is therefore motivated – besides the desire to gain a full theoretical understanding of the underlying quantum chemical mechanisms – by a great astrophysical interest in its *rate coefficient* α. This quantity is defined as

$$\alpha = \langle \sigma\, v \rangle \,, \tag{4.3}$$

with σ denoting the cross section for electron collisions leading to a dissociative recombination (4.2), and v the mutual velocity of the reactants. The averaging is done taking into account the probability distribution of v, which in interstellar clouds corresponds to a temperature of a few Kelvin. For comparison of laboratory results usually the thermal rate coefficient at $300\,\mathrm{K}$ is extracted from the data, which corresponds to the thermal distribution of electron velocities at a temperature of $300\,\mathrm{K}$.

The lifetime τ_DR of a molecular ion vs. dissociative recombination is then given by the density n_e of free electrons,

$$\tau_\mathrm{DR} = \left(\alpha\, n_\mathrm{e}\right)^{-1}\,. \tag{4.4}$$

Because of its astrophysical importance, the rate coefficient α of the DR of $\mathrm{H_3^+}$ has been extensively studied in many experiments as well as theoretical approaches. For an overview, see e.g. [45, 57] and references therein. Despite the apparent simplicity of the system and the well-known potential energy surface of the ion, the DR process, consisting of the capture of a free electron followed by a fast dissociation of the neutral system, turned out to be challenging for both experiment and theory. During the last decades, the results obtained for the rate coefficient α disagreed by up to four orders of magnitude.

The two most important experimental techniques to measure α nowadays are heavy-ion storage rings with the possibility to merge the stored molecular ion beam with a co-moving

---

1 The energy release ΔE of this exothermic reaction will be discussed in the next section.

electron beam, and afterglow experiments, where the decay of a microwave-induced plasma is analysed. Today, all results from storage ring experiments are consistent with a thermal rate coefficient of $\alpha \approx 1 \cdot 10^{-7} \, \mathrm{cm}^3 \mathrm{s}^{-1}$ at 300 K [73, 32, 20]. Recent afterglow experiments, in contrast, found $\alpha < 1 \cdot 10^{-9} \, \mathrm{cm}^3 \mathrm{s}^{-1}$ [60]. On the theoretical side, a new calculation which for the first time is able to treat this fragmentation reaction in its full dimensionality is supporting the storage ring results [35, 36].

However, to gain a full understanding of the process, the reason for the large difference between the experimental results has to be found. On this background, it is interesting to study not only the value of $\alpha(300\,\mathrm{K})$, but also other aspects of the DR reaction, as revealed by the fragmentation dynamics. The results of these extended experimental investigations can then be used for a more detailed comparison with theoretical calculations. In addition, a good control of all experimental conditions is desirable, including e.g. possible rovibrational excitations of the H$_3^+$ ions. As these excitations are believed to increase the DR rate, a possible reason for the different α values measured in storage ring and afterglow experiments might be a different distribution of rovibrational excitations in both types of experiments. As will be seen in Sec. 4.1.3, studies of the fragmentation dynamics can contribute also in this context to a better understanding of the DR process.

4.1.2   Fragmentation studies of the H$_3^+$ / H$_3$ system

In a storage ring, the rate coefficient α is usually measured as a function of the relative energy E between the molecules and the incident electrons. The thermal rate coefficient at 300 K is then obtained by a folding of $\alpha(E)$ with the desired distribution of electron energies. The full energy dependence of $\alpha(E)$ can already be used for a more detailed comparison of experiment and theory [36].

Another interesting property of the DR reaction is the branching ratio between the two reaction channels (4.2a and b). This ratio was investigated at CRYRING for H$_3^+$ [19] and found to be 3:1 in favour of the three-body channel at low electron energies ($< 25 \, \mathrm{meV}$). At higher energies an increase of the two-body fraction was observed. This behaviour can be explained by means of a statistical model based on simple phase-space assumptions [70]. Similar branching fractions were measured also for the H$_2$D$^+$ isotopomer [18].

In another series of experiments, U. Müller *et al.* [53, 50, 23] investigated the fragmentation of single Rydberg states of neutral H$_3$. These states were prepared by the neutralisation of keV H$_3^+$ ions in a cesium cell, followed by a laser-induced transition from the metastable $2pA_2''$ Rydberg state to the state to be studied. By the measurement of the fragmentation geometries, the kinetic energy release and the dependency of transition rates and fragmentation patterns on the laser frequency, the dynamics of the fragmentation of the neutral H$_3$ system when starting

	H_3^+	D_3^+	H_2D^+	D_2H^+		H_2	D_2	HD
$\Delta E^{(3)}$	4.76	4.63	4.67	4.72	D_0	4.48	4.55	4.51

Tab. 4.1: *Chemical energy release $\Delta E^{(3)}$ for the three-body decay of the isotopomers of H_3^+ following DR. For the two-body channels, the binding energy D_0 of the emerging neutral molecule has to be added, $\Delta E^{(2)} = \Delta E^{(3)} + D_0$. All energies are given in eV.*

in well defined electronic and rovibronic states then was investigated. These experiments illuminate processes which play a role also in the DR of H_3^+ with low-energy electrons. However, instead of the metastable electronic state which makes it possible to investigate dissociation reactions starting from a specific state of the neutral system, the DR reaction can proceed via a variety of high-lying Rydberg states[2] of H_3, which complicates the theoretical treatment [36].

In the experiments presented here, new aspects were studied for the DR of H_3^+. In particular, the breakup dynamics in both channels were investigated using fragment imaging techniques. Moreover, new results on the rovibrational excitation of the stored ions could be obtained. As an additional benchmark for theoretical calculations, the same studies were performed on all four stable isotopomers of the triatomic hydrogen ion, that is on H_3^+, D_3^+, H_2D^+ and D_2H^+, revealing interesting isotope effects, as described in detail in the following sections.

4.1.3 Energy considerations for the H_3^+ DR

As noted before, the DR of H_3^+ is an exothermic reaction, that can lead to two final channels (see Eq. (4.2)). The energies $\Delta E^{(3)}$ and $\Delta E^{(2)}$, which are set free by the reaction in the two-body and three-body breakup channel, respectively, reflect the change in binding energy during the transition from the initial to the final channel. As sketched in Fig. 4.1, the energy release $\Delta E^{(2)}$ in the two-body channel can be calculated from the binding energy $D_{H_3^+} = 4.37\,\text{eV}$ of the H_3^+ molecular ion [16] and the ionisation potential $I_H = 13.61\,\text{eV}$ of the hydrogen atom:[3]

$$\Delta E^{(2)} \;=\; I_H - D_{H_3^+} \;=\; 9.23\,\text{eV} \tag{4.5}$$

In the three-body channel, the energy release is reduced by the binding energy $D_{H_2} = 4.48\,\text{eV}$ of the neutral hydrogen molecule [21]:

$$\Delta E^{(3)} \;=\; I_H - D_{H_3^+} + D_{H_2} \;=\; 4.76\,\text{eV} \tag{4.6}$$

For the reactions of the three heavier isotopomers, slightly different values are obtained, as summarised in Tab. 4.1.

---

2   The $2pA_2''$ metastable state is not populated here due to its energetic position far below the H_3^+ ground state.

3   All energies are defined positive here.
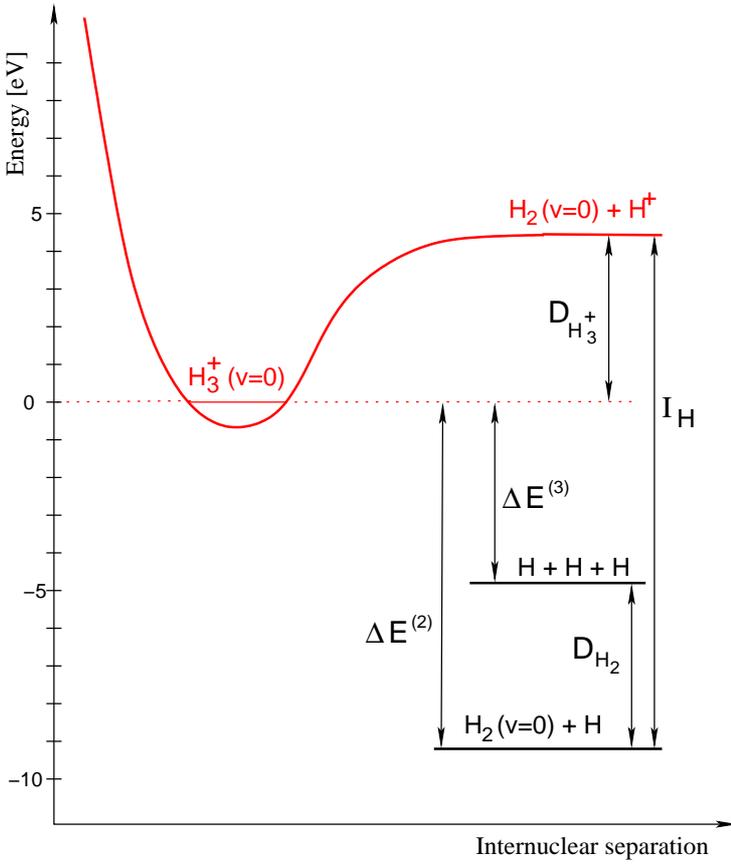
Fig. 4.1: *Scheme of energies relevant for the DR of H_3^+. D_X describes the adiabatic binding energy D_0 of the molecule X with respect to the energetically lowest fragmentation channel, that is $H_2 + H^+$ in the case of $D_{H_3^+}$. I_H denotes the ionisation potential of the hydrogen atom, $\Delta E^{(3)}$ and $\Delta E^{(2)}$ the chemical energy set free by the DR reaction in the three-body and two-body channel, respectively. The term internuclear separation here describes qualitatively the transition from the H_3^+ equilibrium geometry to a geometry where all reaction products have infinite mutual distances. The scheme is given for the electronic and rovibrational ground state of all atoms and molecules involved.*

To conserve the total energy, this reduction of the energy stored in chemical bonds has to be compensated by an increase of the energy available for internal excitations and relative motion of the fragments. In the most general case, this can be written as

$$\Delta E^{(3)} = \left(E_{\text{kin}} + E_{\text{el}}^{\text{f}}\right) \qquad\qquad - \left(E_{\text{e}} + E_{\text{el}}^{\text{i}} + E_{\text{vib}}^{\text{i}} + E_{\text{rot}}^{\text{i}}\right) \qquad (4.7a)$$

$$\Delta E^{(2)} = \underbrace{\left(E_{\text{kin}}^{(2)} + E_{\text{el}}^{\text{f}} + E_{\text{vib}}^{\text{f}} + E_{\text{rot}}^{\text{f}}\right)}_{\text{product energies}} - \underbrace{\left(E_{\text{e}} + E_{\text{el}}^{\text{i}} + E_{\text{vib}}^{\text{i}} + E_{\text{rot}}^{\text{i}}\right)}_{\text{reactant energies}} . \qquad (4.7b)$$

E_{kin} here describes the total kinetic energy of all fragments produced, measured in the co-moving center-of-mass frame of the molecule. This quantity is also referred to as the *kinetic energy release* (KER) of the reaction, and can be addressed in fragment imaging experiments, as shown in Sec. 3.3.2.

E_{el}^{f} is the total energy of any electronic excitations of the fragments produced. Here, the lowest electronically excited fragment state is the $n = 2$ state of the H atom with an excitation energy of 10.2 eV. The small energy ΔE available thus inhibits an electronic excitation of reaction products in the three-body channel, and in most cases also in the two-body channel. $E_{\text{vib}}^{\text{f}}$ and $E_{\text{rot}}^{\text{f}}$ denote vibrational and rotational excitation energies, respectively, in the final channel. These excitations are possible only in the two-body channel, where a molecular fragment is

produced.

For the energetic situation prior to the reaction, E_e describes the relative energy of the colliding electron. In the experiments considered here, a velocity-matched electron beam was used; E_e is thus determined by the electron temperature of roughly $10\,\mathrm{meV}$. The term $E_{\mathrm{el}}^{\mathrm{i}}$ in this general consideration denotes the energy of electronic excitations of the incoming molecular ion. However, as the H_3^+ ion possesses no stable, electronically excited state, this quantity can be considered zero. Vibrational excitations of the H_3^+ ions are radiatively cooled during the first seconds of storage, as was confirmed in a CEI experiment [38, 37]. The energy $E_{\mathrm{vib}}^{\mathrm{i}}$ can thus also be neglected, provided that only data taken after several seconds of storage are used in the analysis, as was done in the experiments described here.

The rotational excitation energy $E_{\mathrm{rot}}^{\mathrm{i}}$ of the H_3^+ ions cannot be measured with the CEI method. As the molecular ions are likely to be produced in the ion source in rotational excited states, and these can have rather long lifetimes especially for the infrared inactive homonuclear species, a considerable rotational excitation of the reacting molecules has to be expected. An estimation of $E_{\mathrm{rot}}^{\mathrm{i}}$ is thus one of the goals of the investigations presented here.

Given these considerations, the energy balance for the two channels can be summarised as

$$E_{\mathrm{kin}} = \Delta E^{(3)} + E_e + E_{\mathrm{rot}}^{\mathrm{i}} \tag{4.8a}$$

$$E_{\mathrm{kin}}^{(2)} = \Delta E^{(2)} + E_e + E_{\mathrm{rot}}^{\mathrm{i}} - E_{\mathrm{vib}}^{\mathrm{f}} - E_{\mathrm{rot}}^{\mathrm{f}} - E_{\mathrm{el}}^{\mathrm{f}} \tag{4.8b}$$

Because of the known total energy release $\Delta E^{(3)}$ and the small electron energy E_e, a measurement of the kinetic energy release E_{kin} in the three-body channel can yield information on the rotational excitation $E_{\mathrm{rot}}^{\mathrm{i}}$ of the stored H_3^+ molecules.

For the two-body channel, the dominant contribution to the measured kinetic energy release $E_{\mathrm{kin}}^{(2)}$ is, besides the well-known $\Delta E^{(2)}$, the vibrational excitation of the molecular fragment $E_{\mathrm{vib}}^{\mathrm{f}}$. Nevertheless, rotational excitations of H_3^+ and H_2 have to be considered also. However, a measurement of $E_{\mathrm{kin}}^{(2)}$ can still yield an approximative picture of the vibrational state distribution in the molecular fragment.

Because of the large energy release $\Delta E^{(2)}$, an electronic excitation of the atomic H fragment cannot be completely excluded for the two-body channel. As can be seen from Eq. (4.8b), and the value of $E_{\mathrm{el}}^{\mathrm{f}} = 10.20\,\mathrm{eV}$ for H($n=2$), an initial rotational or kinetic energy of at least $0.97\,\mathrm{eV}$ is needed to produce an H_2 molecule in its rovibrational ground state together with an excited H(n=2) atom. The very low kinetic energy release $E_{\mathrm{kin}}^{(2)}$ resulting from this process can be used as an efficient probe for high rotational excitations of the H_3^+ ions.

The main focus of the experiments presented in the following lies on the fragmentation patterns and the KER in the three-body dissociation channel. Results for the two-body channel were also obtained [69], but are summarised only shortly here.

Ion type	H$_3^+$	D$_3^+$	H$_2$D$^+$	D$_2$H$^+$
Beam energy [MeV]	1.43	1.44	1.92	1.20
Storage time [sec]	10	80	15	60
Precooling time [sec]	3	10	5	10

Tab. 4.2: *Beam energies and storage times used in the imaging experiments on H$_3^+$ and its isotopomers.*

4.2   Experimental setup and procedures

For the experiments on H$_3^+$ and its isotopomers, the experimental apparatus described in Sec. 3.3 was used, including in particular the heavy ion storage ring TSR, with the electron cooler device and the neutral fragment imaging detector setup. For production of the ion beam, a standard CHORDIS ion source was used. The CHORDIS (Cold or HOt Reflex Discharge Ion Source) is a hot filament source that produces molecular cations in a gas discharge driven by electrons emitted by the filaments [33]. Acceleration was achieved employing the high current injector. For each of the isotopomers, a beam energy was selected such that the fragments emerging from a DR reaction gained mutual distances of several centimeters until reaching the imaging detector, thus enabling a determination of fragmentation geometries at high resolution. The beam energies used are given in Tab. 4.2.

For each molecule, measurements were done during a beamtime of one week. Imaging data were accumulated by repeatedly injecting ions into the storage ring and recording fragmentation events during a storage time ranging up to 80 sec (see Tab. 4.2) for each injection. With this procedure, a total number of imaging events in the order of one million was collected for each molecule. On this raw data, several cuts had to be applied. For example, data taken in the precooling time in the first seconds after injection, when the phase space cooling process was not completed, have been discarded. As described below, a strict c.m. cut was additionally applied for background suppression. The number of fully identified three-body events resulting from this procedure was then in the order of 100,000 for each isotopomer.

4.3   Handling and representation of imaging data

The first step in the analysis of imaging data recorded for the breakup of a polyatomic molecule is the separation of the possible reaction channels. In the case of the DR of H$_3^+$ and its isotopomers considered here, these are the full fragmentation channel yielding three atomic fragments (4.2a) and the two-body breakup channel (4.2b), which in case of the heteronuclear isotopomers H$_2$D$^+$ and D$_2$H$^+$ consists again of two subchannels with different isotopic composition of the molecular and the atomic fragments, respectively. For each fragmentation event recorded by the imaging system, it is now necessary to identify the reaction channel which pro-

duced this event. In addition, recorded events which do not represent a *single* fragmentation reaction with *all* fragments detected have to be recognised and excluded from further analysis. In Sec. 4.3.1, the method of channel identification and background suppression applied in the present experiment will be described, which is based on an analysis of the center of mass (c.m.) position of the recorded events. This method implies an identification of the mass of each observed fragment, which will be needed also in later stages of the data analysis procedure.

After the preparation of one separate set of imaging data for each reaction channel, with each set consisting only of completely recorded fragmentation patterns for a large number of single molecules, the fragmentation dynamics in each channel can be investigated by the analysis of the corresponding set of imaging data. Regarding the two-body fragmentation channels, this analysis follows the standard procedures applied also in fragmentation experiments on diatomic molecules. An overview of the results obtained here will be given in Sec. 4.4.3.

For the analysis of the three-body fragmentation data, new considerations are necessary regarding the representation and interpretation of these multi-dimensional imaging data. In Sec. 4.3.2, a method will be described which allows the extraction of interesting physical properties of three-body breakup reactions from the recorded data.

As described in Sec. 3.3.2, important limitations of the experimental setup employed here are the use of a 2D imaging detector and the unknown point of dissociation within the interaction region. For the interpretation of three-body imaging data recorded with such a system, an important tool is a Monte-Carlo forward simulation algorithm which models the physical breakup process and the detection system in use, as will be described in Sec. 4.3.3. Using these simulated data, the sensitivity of the experiment to different properties of the physical process and of the experimental setup can be tested. In addition, the simulated data can be compared to data obtained in a real experiment, revealing information on the process studied even in situations where a direct reconstruction of the event kinematics on an event by event basis is not possible.

4.3.1   Separation of reaction channels and assignment of fragment masses

In an ideal imaging experiment, reaction channels with different fragment multiplicities could easily be separated through the number of fragments seen on the detector for each event. However, the MCP detector used in the present experiment has a limited detection efficiency for each impinging fragment (see Sec. 3.3.2). Therefore the number of fragments observed for a given event is here no sufficient criterion for an identification of the reaction channel which produced the event. For example, an event consisting of two detected fragments could well have its origin in a three-body breakup, with one of the fragments staying undetected. On the other hand, there is a small chance for event-mixing: If two dissociating molecules arrive in coincidence at the
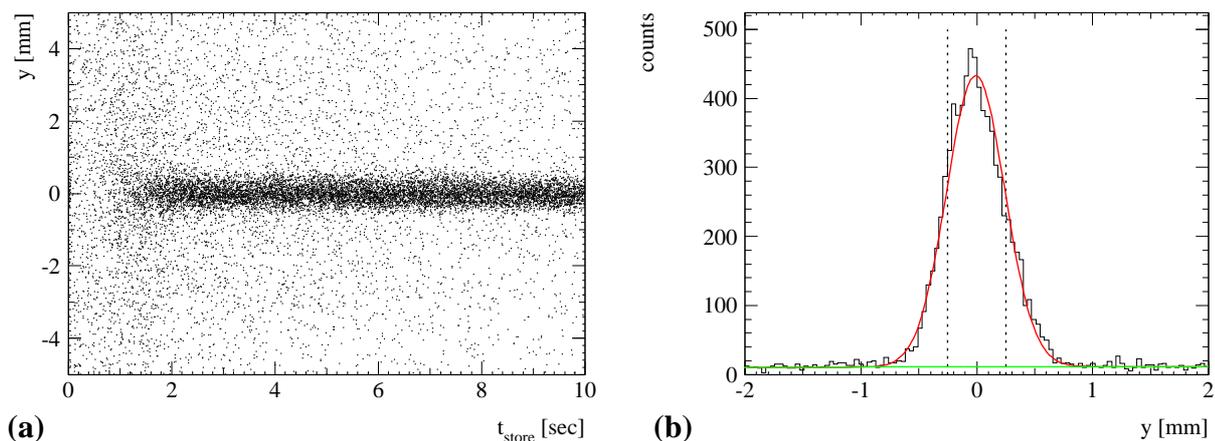
Fig. 4.2: *Distribution of the vertical center-of-mass position of three-fragment events observed for the DR of H$_3^+$: (a) evolution with storage time (b) distribution for $t_{store} \geq 3$ sec. A Gaussian fit (red) yields a width of $\sigma_y = 0.25$ mm here. The background contribution (green) is estimated to be $\approx 1\%$ within the c.m. cut indicated by the vertical lines; see text for details.*

detector, and some of the fragments are not detected, this can produce a two- or (more likely) three-body event with fragments mixed from different molecules.

To separate these various background events from 'good' events, where *all* the fragments produced in *one* breakup reaction are recorded, a convenient method is to put restrictions on the center of mass of the observed fragments. This method profits from the good beam quality usually achieved in a storage ring. After a few seconds of phase space cooling (see Sec. 3.3.1), the spatial extension as well as the divergence of the ion beam are small enough to confine the 'impact' positions of the center of mass of the fragmenting molecules on the detector to an area of <1 mm diameter, as shown in Fig. 4.2.

For the three-body breakup of a *homonuclear* molecule, the individual c.m. of a 'good' event stemming from a single, completely recorded fragmentation reaction is given by the average of the three fragment positions and will be located close to the mean c.m. of the beam. For background events resulting from event-mixing, on the other hand, the average of the fragment positions has no physical meaning and will be scattered statistically over a much bigger area on the detector. A cut for the separation of 'good' events from event-mixing background can thus be applied by evaluation of the distance between the calculated individual c.m. position of each event and the mean c.m. position of all recorded events. Only events where this distance is small enough are considered 'good' events and further analysed.

The *mean* c.m. position is determined by a Gaussian fit of the distribution of a large number of individual c.m. positions, as shown in Fig. 4.2(b) for the vertical component. Similarly, mean position and sigma width of the horizontal c.m. distribution are determined. Using these data, the evaluation of the individual c.m. position of each recorded event can be performed

by comparing its horizontal and vertical distance (δx, δy) from the mean c.m. position to the sigma widths (σ_x, σ_y) of the c.m. distribution. The quality of each observed event is therefore estimated by calculating

$$\Delta^2 \; = \; \left(\frac{\delta x}{\sigma_x}\right)^2 \; + \; \left(\frac{\delta y}{\sigma_y}\right)^2 \, , \tag{4.9}$$

Thus, Δ measures the distance of the individual c.m. from the mean c.m. in units of its standard deviation.

In the present experiments, only events with $\Delta \leq 1$ are considered good events and further analysed. This means that the individual c.m. position of a good event is required to lie within an ellipse around the mean c.m. position with the radii σ_x and σ_y. In Fig. 4.2(b), the maximal extension of this region in the vertical direction is indicated by the dotted lines.

For the interpretation of imaging data, it will be important to estimate the relative amount of background events still present within the chosen c.m. cut, as well as the physical properties deduced from these events. To estimate the number of background events passing the c.m. cut, the fit shown in Fig. 4.2(b) is performed employing a sum of two Gaussian functions. While the red line in the figure describes this sum, the green line gives the contribution of the very broad second Gaussian component. The *quantitative* contribution of background events can now be estimated by comparing the number of events (integrated over the region of the c.m. cut) in the Gaussian describing the background and in the total distribution.

To estimate the properties of these background events, that is, their *qualitative* contribution to the experimental results, an additional set of data is prepared where the factor Δ defined in (4.9) is required to fulfil $5 \leq \Delta \leq 10$. At this large distance from the mean c.m., the contribution of 'good' events can be assumed to be negligible, therefore a set of pure background data is prepared. In the analysis of breakup energetics and geometries, the contribution of background events can then be estimated by performing the same analysis steps on both the 'good' and the background data sets and taking into account the relative number of background events as deduced above.

The value of $\Delta = 1$ used as the limit in the present c.m. cut is a compromise between the need for high statistics and the desire for a background-free data set. As will be seen later, a good background suppression is essential in the analysis of certain properties of the fragment geometry distributions; therefore a rather strict c.m. cut was applied.

In principle, the same method can be used also on three-fragment events observed for the DR of one of the *heteronuclear* isotopomers to separate good events, which stem from the three-body breakup channel, from event-mixing background. However, in this case the masses of the three fragments are not equal and thus a mass assignment has to be done for the fragments of each observed event in order to calculate the individual center of mass. As sketched in Fig. 4.3, this is done by calculating the individual c.m. position for each possible assignment of masses,
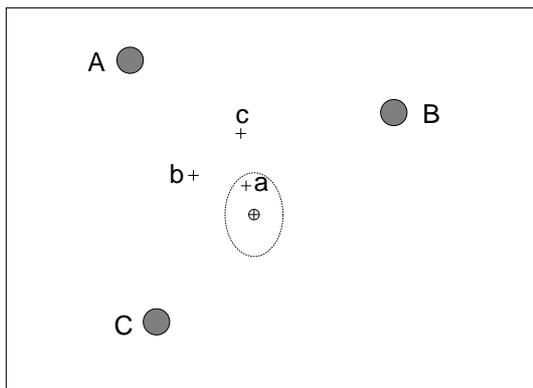
Fig. 4.3: *Center of mass analysis for D$_2$H$^+$: schematic view of a three-body event as seen on the imaging detector. A, B and C denote particle impact positions, a, b and c the three possible positions of the individual c.m. of this event, which result from the tentative identification of particle A, B or C, respectively, as the hydrogen atom. The mean c.m. position of the beam is denoted by $\oplus$, the dotted line indicates the acceptance of the c.m. cut.*

and then selecting the most probable assignment as the one with the smallest distance of the calculated c.m. to the mean c.m. of the beam. On this distance the usual cut is then applied. The assignment of masses is important not only for application of the c.m. cut, but will also be used in the subsequent analysis of breakup geometries and energetics.

With this method, an unambiguous assignment of fragment masses is possible only if the mutual separation of the different c.m. candidates is larger than the extension of the mean c.m. region described by (σ_x, σ_y). For too small fragment distances and correspondingly small distances of the three c.m. candidates, a misassignment of fragment masses is possible. Although always the 'best' c.m. candidate is chosen, that is the one with the highest probability of a correct mass assignment, in such cases where another candidate is of similar quality within the resolution of the method (being the σ width of the mean c.m. distribution), the resulting mass assignment has some probability to be wrong. This introduces a background contribution that adds to the event-mixing background. However, the described procedure for estimating the background contribution covers also these events, allowing to take them into account in the interpretation of the data.

To prepare a data set for analysis of the two-body fragmentation channel, the same method is applied on the observed two-fragment events. An assignment of fragment masses is necessary here in the case of all four isotopomers in order to calculate the individual c.m. positions. The cut on Δ then suppresses background events which here mainly stem from three-body breakup reactions where only two fragments are detected. For the heteronuclear species, the mass assignment in the two-body channel includes not only the identification of the atomic and molecular fragments, but also the assignment of each event to one of the two subchannels. This complicates the preparation of background-free data sets for the two-body reaction channels of these species (see Sec. 4.4.3).

4.3.2   Representation of three-body fragmentation data

As seen in Sec. 3.3.2, in the simple case of a diatomic molecule, only one internal degree of freedom exists. In the description of the original molecule, this corresponds to the internuclear distance r. When a fragmentation occurs, the system evolves according to a one-dimensional potential energy curve $V(r)$. Finally, a certain amount of energy is transformed to kinetic energy related to the relative motion of the two atoms. These reach asymptotically a relative velocity v, which correlates to the observed (2D) distance R of the impact positions of the two fragments on the imaging detector.

For a three-body fragmentation process, this simple picture is complicated by the appearance of additional degrees of freedom. The geometry of a triatomic molecule is at first described by the positions of the three atoms in space, which represent nine degrees of freedom. Three of these describe the overall translational position of the system as a whole, given e.g. by the position of the c.m. of the molecule. Another three coordinates define the overall orientation of the molecule, as described e.g. by the three Euler angles. These six *external* degrees of freedom are not of interest here. The three remaining, *internal* degrees of freedom define the geometry of the molecule, corresponding to the internuclear distance in the diatomic case.

The fragmentation of a triatomic molecule is thus described within this three-dimensional space of internal coordinates. The potential energy surface governing the dissociation process is a function of these three coordinates, and subsequently also the asymptotic velocities reached by the fragments and the resulting pattern of impact positions on the imaging detector are described by three parameters.

This three-dimensional internal configuration space can be parametrised in various ways, depending on the specific problem under study. In the present case, an interesting physical property of the breakup reaction to be extracted from the recorded imaging data is the total kinetic energy release E_{kin} of the reaction. As shown in Sec. 4.1.3, this energy is connected to the rotational excitations of the molecular ions, whose investigation is one of the goals of the present experiments.

The total kinetic energy release E_{kin} is calculated as the sum of the kinetic energies E_i carried by the three fragments in the co-moving c.m. frame of the molecule

$$E_{\text{kin}} = \sum_{i=1}^{3} E_i \, , \qquad E_i = \frac{m_i}{2} \, u_i^2 \, , \qquad (4.10)$$

where m_i describes the mass of fragment i, and u_i its velocity relative to the c.m. of the system. The velocities u_i are, with some important restrictions discussed later, accessible in an imaging measurement, while the fragment masses m_i are determined during the identification of three-body fragmentation events as described in Sec. 4.3.1. Thus the energies E_i can be used to parametrise the observed fragmentation patterns.

After selecting E_{kin} as one of the three coordinates to be used in this parametrisation, two internal coordinates remain, which describe the sharing of this kinetic energy among the three fragments, or the *shape* of the breakup pattern. The method of representation of these two-dimensional data has to be carefully chosen in order to avoid artificial structures created by the properties of the chosen coordinates instead of the physical process.

Dalitz plots

A method that proves efficient for this task is the use of *Dalitz plots*. As will be shown below, an uncorrelated three-body breakup would result in an uniform density of events within the kinematically allowed region of a plot of this type. Therefore, these coordinates are well suited for an unbiased representation of experimental data on the geometry in three-body breakup reactions, allowing a direct identification of fragmentation geometries preferred or avoided in the breakup process. Dalitz coordinates have already been used for representation of H_3 fragmentation data by Helm and coworkers [53]. However, the specific conditions of the present experiment demand a detailed consideration of their properties, especially because of the use of 2D imaging data and unsymmetric isotopes.

Hence, basing on the derivations by Dalitz [17] and Perkins [59] and starting from simple phase space considerations, the definition and important properties of Dalitz plots are presented in the following, before adapting them to the specific case of interest here.

For a single particle, the number of states in a phase space cell delimited by the momenta p and $p + dp$ as well as the solid angle $d\Omega$ is (up to a normalisation factor C)

$$d^3N = C\, p^2\, dp\, d\Omega\,.$$

For three particles, which are independent except for momentum and energy conservation restricting (in the center of mass frame of reference) the total momentum to zero and the total kinetic energy to E_{kin}, the number of states is

$$d^9N = C^3\, p_1^2\, dp_1\, d\Omega_1\, p_2^2\, dp_2\, d\Omega_2\, p_3^2\, dp_3\, d\Omega_3\, \delta(E_1 + E_2 + E_3 - E_{kin})\, \delta(\vec{p}_1 + \vec{p}_2 + \vec{p}_3)$$

where $E_i = p_i^2/2m_i$ is the non-relativistic kinetic energy of particle i, which has a mass of m_i. Momentum conservation allows one to integrate over the coordinates of one of the particles, thus fixing e.g. $\vec{p}_3 \equiv -\vec{p}_1 - \vec{p}_2$. For an isotropic overall orientation of the three-particle system in space, the integrals over all directions of the remaining two particles can be expressed as $\iint d\Omega_1 = 4\pi$ and $\int d\Omega_2 = 2\pi\, d\cos\theta_{12}$, where θ_{12} denotes the angle between $\vec{p}_1$ and $\vec{p}_2$, thus yielding

$$d^3N = 8\pi^2 C^3\, p_1^2\, dp_1\, p_2^2\, dp_2\, d\cos\theta_{12}\, \delta(E_1 + E_2 + E_3 - E_{kin}) \tag{4.11}$$

for the number of states in the phase space cell spanned by dp_1, dp_2 and $d\cos\theta_{12}$.

Using the non-relativistic energy-momentum relations

$$E_1 = \frac{p_1^2}{2m_1}, \quad E_2 = \frac{p_2^2}{2m_2}, \quad E_3 = \frac{p_3^2}{2m_3} = \frac{1}{2m_3} \left(p_1^2 + p_2^2 + 2p_1 p_2 \cos\theta_{12} \right) ,$$

one obtains

$$\frac{\mathrm{d}E_1}{\mathrm{d}p_1} = \frac{p_1}{m_1}, \quad \frac{\mathrm{d}E_2}{\mathrm{d}p_2} = \frac{p_2}{m_2}, \quad \frac{\mathrm{d}E_3}{\mathrm{d}\cos\theta_{12}} = \frac{p_1 p_2}{m_3} .$$

Thus, (4.11) can be written as

$$\begin{aligned} \mathrm{d}^3 N &= C' \left(\frac{\mathrm{d}E_1}{\mathrm{d}p_1} \right) \mathrm{d}p_1 \left(\frac{\mathrm{d}E_2}{\mathrm{d}p_2} \right) \mathrm{d}p_2 \left(\frac{\mathrm{d}E_3}{\mathrm{d}\cos\theta_{12}} \right) \mathrm{d}\cos\theta_{12} \, \delta(E_1 + E_2 + E_3 - E_{\mathrm{kin}}) \\ &= C' \, \mathrm{d}E_1 \, \mathrm{d}E_2 \, \mathrm{d}E_3 \, \delta(E_1 + E_2 + E_3 - E_{\mathrm{kin}}) , \end{aligned}$$

with the constant factor $C' = 8\pi^2 C^3 m_1 m_2 m_3$. Integration over the energy of the arbitrarily chosen particle 3 then yields

$$\mathrm{d}^2 N = C' \, \mathrm{d}E_1 \, \mathrm{d}E_2 . \tag{4.12}$$

Thus, if the kinetic energies of two of the three fragments are chosen as coordinates of a two-dimensional plot, a random breakup will lead to a uniform event density in the kinematically allowed region of this plot. In other words, the phase space density $\frac{\mathrm{d}^2 N}{\mathrm{d}E_1 \mathrm{d}E_2}$ is constant in this region. Obviously, this property stays conserved also for linear combinations of fragment energies, but is not valid e.g. for a plot of fragment momenta or velocities.

In order to select particular linear combinations of fragment energies as the coordinates to be used, it is advantageous to consider the symmetry of the molecular system with respect to permutations of the three atoms. For the homonuclear species H_3^+ and D_3^+, all three fragments are identical. Thus, the result of a fragmentation experiment will be symmetric under any permutation of these three fragments. Therefore, a type of representation is chosen where the sixfold symmetry corresponding to the permutation group S_3 is reflected by simple geometric symmetry properties in the two-dimensional coordinate plane. Such a representation simplifies the interpretation of experimental data, as for any structure observed it is here easy to distinguish between features which result from the trivial permutation symmetry of the system, and features that reflect physical properties of the breakup reaction.

As shown in Appendix A.1, these basic requirements lead directly (up to an arbitrary overall normalisation factor) to the *Dalitz* coordinates

$$\eta_1 = \frac{E_2 - E_1}{\sqrt{3} E_{\mathrm{kin}}}, \qquad \eta_2 = \frac{E_3}{E_{\mathrm{kin}}} - \frac{1}{3} \tag{4.13}$$

These coordinates were first introduced in 1953 by R.H. Dalitz [17] in order to analyse correlations of fragment energies in the three-body decay of τ-leptons[4] into π-mesons. Unlike

---

4   at that time considered to be 'τ-mesons'

(a)   **(b)**
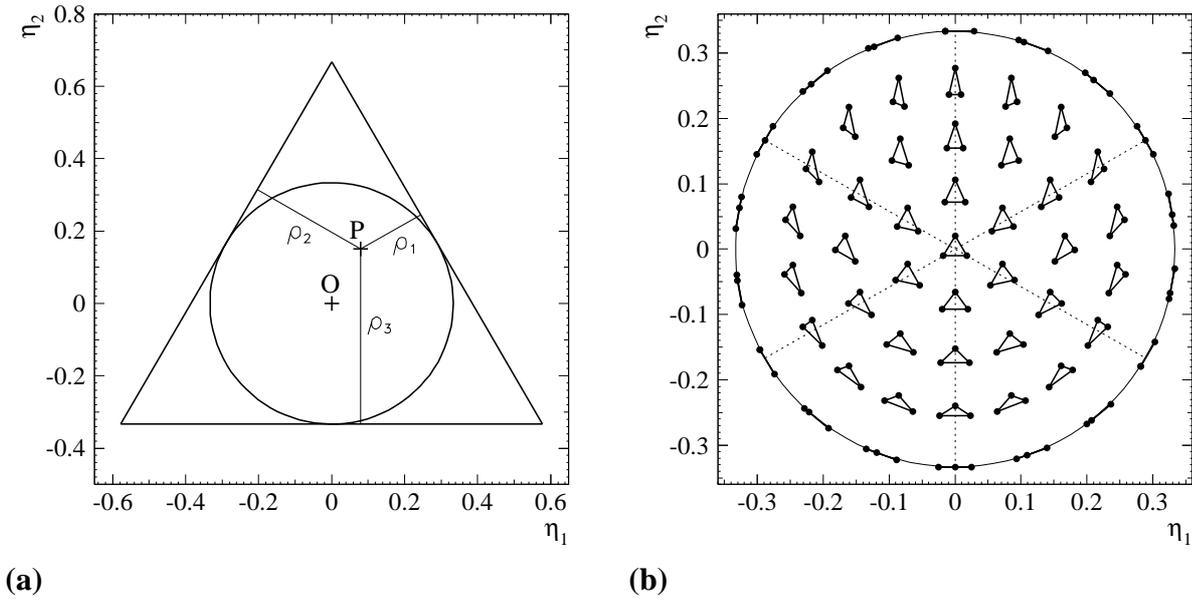
Fig. 4.4: *Dalitz plot for a fragmentation into three particles of equal mass. (a) kinematically allowed region and energetic interpretation (b) interpretation in terms of fragmentation geometries.*

the application in particle physics, the aim of this representation in the present experiments is not the finding of resonant structures corresponding to the formation of intermediate particles, but a more general investigation of preferred and avoided fragmentation geometries, which are connected to the shape of the potential energy surface driving the dissociation.

Through the normalisation to the total energy E_{kin}, the *Dalitz plot* becomes dimensionless and the geometry of any breakup into three fragments of equal mass can be represented by the same kind of plot, independent of the total energy. It is easy to show (see App. A.2) that the energetically allowed region in this plot ($E_i \geq 0$ for $i = 1, 2, 3$) is delimited by a triangle as drawn in Fig 4.4a. Momentum conservation further restricts the allowed region to the interior of a circle with radius $\frac{1}{3}$ centered at the origin O of the coordinate frame (App. A.3). An interpretation of such a plot in terms of fragment energies is that for any point P inside the allowed region, the distances ρ_i from P to the three sides of the triangle represent the relative energies of the three fragments, $\rho_i = E_i/E_{kin}$.

The geometric meaning of the Dalitz coordinates in terms of the shape of fragmentation patterns is visualised in Fig. 4.4b. Each pictogram represents the arrangement of fragment velocities (and therefore the shape as seen on an ideal detector) corresponding to one point in the Dalitz plot. The dotted lines depict symmetry axes. A reflection at one of these axes describes the exchange of two of the three identical fragments. The overall sixfold symmetry thus reflects the six possible permutations of the fragments.

In terms of polar coordinates, the *radius* (or distance from the origin) in a Dalitz plot can be viewed as a measure of the *linearity* of the fragmentation pattern. An equilateral triangular shape corresponds to the origin of the plot, while the various linear arrangements are represented at the edge of the circular allowed region. The polar *angle* of a point in the plot is connected to the *symmetry* of the corresponding fragmentation pattern, with isosceles triangles situated along the dotted lines and asymmetric shapes in between.

If the molecule studied has a lower symmetry, like D_2H^+ or H_2D^+, the Dalitz plot loses some of its symmetry properties, but still can be used as a valuable tool for displaying geometry data and for comparison of this data between different isotopomers. A plot of the standard Dalitz coordinates (4.13) still has the property of equal phase space density within the kinematically allowed region. However, the boundary of this region is stretched to an elliptical shape when the masses of the three fragments are not equal. Similarly, the geometrical interpretation of the points inside the allowed region changes.

For an easier comparison of different isotopomers, a modified Dalitz plot is used, where this stretching of the kinematically allowed region is compensated by a rescaling of the coordinates. In the molecular systems studied here, a twofold symmetry remains as two of the fragments still have equal mass ($m_1 = m_2$). For this case, the derivation in App. A.3 shows that the same circular shape of the kinematically allowed region is maintained when using the following *generalised Dalitz coordinates*:

$$\eta_1 = \sqrt{\frac{M}{3m_3}}\frac{E_2 - E_1}{\sqrt{3}E}, \qquad \eta_2 = \frac{M}{3m}\frac{E_3}{E} - \frac{1}{3} \qquad (4.14)$$

with $m = m_1 = m_2$ and $M = \sum m_i = 2m + m_3$. Obviously these definitions are equivalent to the standard Dalitz coordinates (4.13) in case of the symmetric isotopomers H_3^+ and D_3^+, where $m = m_3$. As also these generalised Dalitz coordinates are linear combinations of single fragment energies, they keep the advantage of uniform phase space density over the kinematically allowed region. The boundary of this region is again a circle of radius $\frac{1}{3}$ centered at the origin of the (η_1, η_2) plane. However, the correlation between specific points in the Dalitz plot and the geometry of the breakup is slightly changed, as can be seen in Fig. 4.5.

In summary, the three-dimensional space of internal coordinates which describes the breakup of a molecule into three fragments is chosen to be parametrised by the total kinetic energy release E_{kin} of the breakup reaction and the two dimensionless generalised Dalitz coordinates η_1, η_2 describing the sharing of this energy among the fragments. Before continuing to the implementation of these coordinates in the present experiment, a brief comparison to other types of coordinates used in similar situations is given.
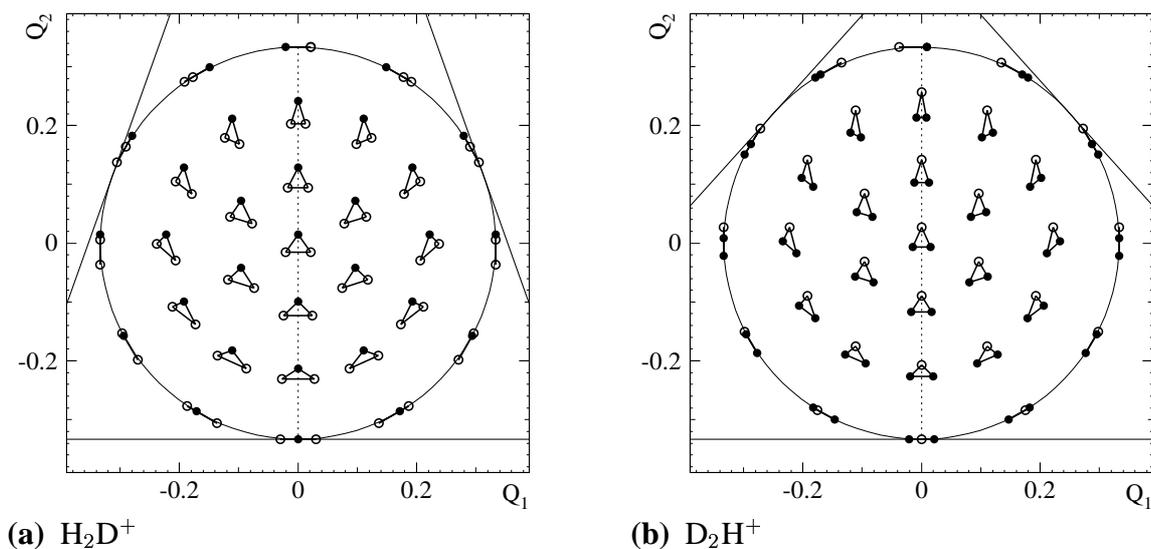
Fig. 4.5: *Geometrical interpretation of Dalitz plots for (a) H$_2$D$^+$ and (b) D$_2$H$^+$. The tangents indicate the energetically allowed region.*

Comparison to other types of coordinates

To describe the geometry and the vibrational modes of the original, bound molecular ion, a convenient choice is the use of *normal coordinates*. These coordinates have the advantage to diagonalise the Hamiltonian of nuclear motion. It is always possible to find such coordinates in regions of the configuration space where the potential energy hypersurface is harmonic in all three dimensions, which is approximatively the case in the proximity of the minimum of any binding PES, that is, for molecular geometries only slightly distorted from the equilibrium geometry. Thus, for low-lying vibrational excitations, the vibrational modes connected to the normal coordinates can be treated as separate, one-dimensional problems. For high levels of vibration implying large deviations from the equilibrium geometry, the PES can usually no longer be treated as harmonic and couplings between the vibrational modes have to be considered.

To find the normal coordinates for a given molecular geometry, it is helpful to consider the nuclear symmetry group of the molecule: The choice of *symmetry coordinates* which transform according to irreducible representations of the symmetry group, already yields a blockwise diagonal form of the Hamiltonian, reducing the diagonalisation problem to subspaces spanned by coordinates of the same symmetry. The normal coordinates finally found are a special (not always unambiguous) case of these symmetry coordinates.

In the case of H_3^+, the equilibrium geometry has C_{3v} symmetry[5]. A possible choice of corresponding normal coordinates is

$$s_a = r_{12} + r_{23} + r_{31}\,, \qquad s_x = \frac{1}{\sqrt{3}}(2r_{12} - r_{23} - r_{31})\,, \qquad s_y = r_{23} - r_{31}\,, \qquad (4.15)$$

with r_{ij} the distance between the ith and jth nucleus. All three coordinates can be scaled by an arbitrary normalisation factor. s_x and s_y correspond to a two-dimensional representation of the C_{3v} group, and can thus be replaced by any two independent linear combinations of s_x and s_y. More details on the normal coordinates of H_3^+ and their application in the description of vibrational motion can be found in [37, 36]. For the breakup reactions considered here, the PES involved consequentially are dissociative, that is, they do not possess a minimum that would allow the development of normal coordinates. A treatment of the dissociation dynamics using three independent coordinates is thus not possible.

It is interesting to note that the normal coordinates (s_a, s_x, s_y), which are obtained as an expansion of the geometry around the well defined equilibrium geometry of the H_3^+ molecule, have considerable similarities with the set $(E_{\mathrm{kin}}, \eta_1, \eta_2)$ that was obtained for an unbiased representation of fragmentation patterns, that is, explicitly without a preference of any special geometry. The origin of this parallelism is the equilibrium geometry of H_3^+, with its C_{3v} symmetry. The particular graphical representation of the S_3 permutation group chosen in the derivation of the Dalitz coordinates also exhibits this C_{3v} symmetry, which explains the structural similarity of the two sets of coordinates.

A general class of coordinates widely used in the description of molecular potential energy surfaces are *hyperspherical coordinates*. Similar to spherical coordinates which parametrise the common three-dimensional space, the generalised hyperspherical coordinates consist of one *hyperradius* describing the length of a vector and several *hyperangles* defining its orientation in a possibly multidimensional vector space.

A variety of different sets of hyperspherical coordinates has been used in theoretical treatments of the H_3 system. One example is the set used by Varandas *et. al* [74, 76], which is similar to the s_a, s_x, s_y coordinates (4.15). After defining

$$\delta = r_{12}^2 + r_{23}^2 + r_{31}^2\,, \qquad \gamma = 2r_{12}^2 - r_{23}^2 - r_{31}^2\,, \qquad \beta = \sqrt{3}\left(r_{23}^2 - r_{31}^2\right), \qquad (4.16)$$

the hyperradius ρ and the hyperangles s, ϕ are chosen as

$$\rho = \sqrt{\delta/3}\,, \qquad s = \frac{\sqrt{\beta^2 + \gamma^2}}{\delta}\,, \qquad \tan\phi = \frac{\beta}{\gamma}\,. \qquad (4.17)$$

---

5   The full molecular point group is $D_{3h} = \sigma_h \otimes C_{3v}$. However, for studying vibrational modes, which are restricted to the molecular plane and thus invariant under the σ_h operation, it is sufficient to consider the C_{3v} subgroup.

This set of coordinates is found to be convenient for the fitting of analytical PES functions to *ab initio* calculated energies, especially in the vicinity of critical geometries like equilateral ($s = 0$) or collinear ($s = 1$) arrangements of the nuclei [74]. Hyperspherical coordinates of similar type were used in recent calculations of the DR of H$_3^+$ by Kokoouline and Greene [35, 36].

The coordinate set $(E_{\text{kin}}, \eta_1, \eta_2)$ chosen for the representation of fragmentation data in the present experiment can also be viewed as a set of hyperspherical coordinates. Even though the definition of these coordinates was based on kinetic energies, as opposed to positions, these energies are closely connected to the fragments velocities and thus to their mutual distances. The various sets of coordinates used in the description of the H$_3^+$/H$_3$ system thus, despite their apparent distinctions, show very similar structures, which are mainly introduced by symmetry considerations. The detailed definitions of the coordinate sets then are adapted to the specific problems to be studied.

The experimental determination of the parameters E_{kin}, η_1 and η_2 chosen here for the description of three-body fragmentation reactions in view of the limited capabilities of the available detection system is discussed in the following.

Handling of 2D imaging data

The discussion of the representation of kinetic energy release and geometry data so far did not take into account any detector efficiencies or other limitations of the experiment. As noted in Sec. 3.3.2, two major effects have to be considered here: The unknown position of the breakup reaction within the interaction region, and the fact that only the fragment positions transversal to the beam direction are recorded by the imaging detector. These restrictions make it impossible to calculate for each recorded event the kinetic energies E_i of the fragments and thus the desired quantities E_{kin}, η_1 and η_2.

However, similar to the diatomic case, an investigation of these quantities is still possible by comparing the fragmentation patterns observed on the detector to the patterns expected under certain assumptions regarding E_{kin}, η_1 and η_2. In the diatomic case, the projected distance R between the two impinging fragments on the detector surface was used to describe the observed fragmentation pattern. Its expected distribution $P(R)$ could be given as an analytical function, using the kinetic energy release of the breakup reaction as a parameter.

In analogy to this, the coordinates $\varepsilon^{\perp}$, Q_1 and Q_2 are chosen to describe the observed fragmentation patterns in the case of a three-body fragmentation as follows: The fragment velocities u_i in the c.m. frame, which are needed for the calculation of E_i (Eq. (4.10)) and therefore also of E_{kin}, η_1 and η_2, are replaced by the measurable quantities R_i, which denote the distance of the impact position of fragment i to the impact position of the c.m. of the molecule

(cf. Sec. 3.3.2). We thus define[6]

$$\varepsilon_i^\perp = m_i R_i^2 \,, \tag{4.18}$$

the mass-weighted squared projected distances, with the fragment masses m_i given in atomic mass units. Subsequently, we get

$$\varepsilon^\perp = \sum_{i=1}^{3} \varepsilon_i^\perp \,, \qquad Q_1 = \sqrt{\frac{M}{3m_3}} \frac{\varepsilon_2^\perp - \varepsilon_1^\perp}{\sqrt{3}\,\varepsilon^\perp} \,, \qquad Q_2 = \frac{M}{3m} \frac{\varepsilon_3^\perp}{\varepsilon^\perp} - \frac{1}{3} \,. \tag{4.19}$$

The $\varepsilon_i^\perp$ are thus proportional to the transverse fragment energy: With the beam energy E_{beam}, the total molecular mass $M = \sum m_i$ in a.m.u. and the (not accurately known) flight distance L, one would get the transverse fragment energies

$$E_i^\perp = \frac{E_{\text{beam}}}{M\,L^2} \varepsilon_i^\perp \,, \tag{4.20}$$

that is, the kinetic energies corresponding to the movement of the fragments transversal to the beam axis. Because of this close relation, $\varepsilon^\perp$ will be denoted *transversal KER* in the following. The Q_1, Q_2 coordinates are dimensionless and can be viewed as *projected Dalitz coordinates*, as they describe the shape of the two-dimensional projected fragmentation pattern visible on the detector surface.

The 'missing link' between the observables $\varepsilon^\perp$, Q_1, Q_2 and the properties E_{kin}, η_1, η_2 of the fragmentation reaction is – as in the diatomic case – the correlation of the relative fragment velocities u_i and the projected distances R_i. Again, a direct reconstruction of the u_i from the measured R_i following Eqs. (3.1) and (3.2) is not possible, as the flight distance L and the orientation of the fragmenting system with respect to the detector plane cannot be determined on an event by event basis. On the other hand, the *probability distributions* also here are known for both the flight distance, which is given by position and size of the electron-ion interaction region, and the orientation angles, which can be considered isotopic. Thus, the probability distributions of the observables $\varepsilon^\perp$, Q_1 and Q_2 can be determined, which are expected under certain assumptions on E_{kin}, η_1 and η_2. By comparison to the experimentally found $\varepsilon^\perp$, Q_1 and Q_2 distributions, these assumptions can then be tested.

In particular, the probability distribution $P(\varepsilon^\perp)$ of the transversal KER $\varepsilon^\perp$ will be compared to the distributions expected for several assumptions on the distribution of the actual E_{kin}. Following Eq. (4.8a), the latter will be constructed out of the given release of chemical energy $\Delta E^{(3)}$ in the three-body channel, and different assumptions on the rotational energy $E_{\text{rot}}^{\text{i}}$ of the incoming molecular ions.

Regarding the shape of the fragmentation pattern, the experimentally found projected Dalitz plot, that is the probability distribution $P(Q_1, Q_2)$ of the projected Dalitz coordinates, will be

---

6 also arbitrarily omitting the factor $\frac{1}{2}$ for simplicity

compared to the distribution expected for an uncorrelated breakup reaction. While the distribution expected in this case for the 3D Dalitz coordinates (η_1, η_2) would be uniform, this is no longer valid in case of the projected coordinates (Q_1, Q_2).

This comparison can in the case of the two-dimensional distribution $P(Q_1, Q_2)$ not be done just by plotting the experimental and expected distributions together in one figure, as it is done for the one-dimensional $P(\varepsilon^\perp)$ distribution. Instead, the experimentally found $P(Q_1, Q_2)$ distribution will be divided by the one expected for an uncorrelated breakup process. The deviations of the resulting *weighted Dalitz plot* from uniformity then make clear for which projected geometries the number of events observed on the imaging detector is higher or lower than expected in the uncorrelated case.

The expected probability distributions are in the present case of a three-body fragmentation process not constructed as analytical functions like in the diatomic case. Instead, a Monte-Carlo simulation algorithm was developed, which produces a set of simulated events, similar to the experimental data, by taking into account the desired physical properties of the fragmentation process regarding E_{kin}, η_1 and η_2, the known probability distributions of flight length and overall orientation, as well as other properties of the experimental setup like the resolution of the imaging system.

This simulation algorithm will be described in the next section. In Sec. 4.3.4, some probability distributions $P(\varepsilon^\perp)$ and $P(Q_1, Q_2)$ resulting from the simulation code will be shown, and the sensitivity of these distributions to changes of several experimental parameters will be tested. In particular, to enable an interpretation of weighted Dalitz plots, the correlation between the actual dissociation geometries (η_1, η_2) and the observed projected geometries (Q_1, Q_2) will be investigated. Section 4.4 finally presents experimental results, analysed and interpreted according to the present considerations.

4.3.3   Monte-Carlo simulation

For the interpretation of experimental data which are strongly affected by detector effects such as the projection of a three-dimensional fragmentation pattern onto the two-dimensional detector plane, a powerful tool usually is a Monte-Carlo forward simulation algorithm. Such an algorithm first models the physical process under study and then takes into account all properties of the experimental setup, in particular the efficiency and sensitivity of the detector used.

In the present case of a three-body fragmentation reaction, the fragmentation dynamics can be described, as seen in Sec. 4.3.2, by the three coordinates E_{kin}, η_1 and η_2. The physical breakup process studied here is thus modelled in the simulation by choosing these coordinates according to certain probability distributions.

Selection of the breakup energy

For the breakup energy E_{kin}, in the simplest case just the release of chemical energy $\Delta E^{(3)}$ in the three-body channel is taken according to Tab. 4.1. To enable an investigation of rotational excitations of the molecular ions, a mechanism generating an additional rotational energy $E_{\text{rot}}^{\text{i}}$ for each simulated event was included following a simple thermal model for the probability distribution of $E_{\text{rot}}^{\text{i}}$. Each rotational state is described by the quantum numbers J of the total angular momentum and K for its projection on the axis normal to the molecular plane. The energy of this state is taken from the approximative formula

$$E_{\text{rot}}^{\text{i}}(J, K) \approx B \left[J(J+1) - \frac{1}{2}K^2 \right] \tag{4.21}$$

with the rotational constant $B = 5.33 \, \text{meV}$ for H_3^+. Possible K values for each J range from $-J$ to J, and each of these states exhibits a $(2J+1)$ multiplicity due to the possible orientations of the rotating molecule in the laboratory frame of reference. In the case of H_3^+, states with $K = 0$ and even J are spin-forbidden. This simplified treatment based on a symmetric top formula [41] reproduces the rotational levels found in a high-level *ab initio* calculation [61] within $\sim 2\%$ (for the states up to $J = 5$ considered there), an accuracy much higher than needed here. A more detailed consideration can be found in [80].

The probability of each state is now determined using a Boltzmann distribution for a given rotational temperature T_{rot}, taking into account the multiplicity of each state. The energy distribution generated according to this model can only be used for a rough estimation of the amount of rotational excitation in the experiment because of some strongly simplifying assumptions: Firstly, the distribution of rotational states produced in the ion source does not have to be thermal and a subsequent thermalisation in the storage ring is not expected for the infrared-inactive species H_3^+ and D_3^+. Secondly, the DR rate coefficient might differ depending on the rotational state, leading to a rotational distribution in the observed breakup events which is different from the population in the original beam. However, to get an estimate of the order of magnitude of the rotational excitation energy carried by the molecular ions, the present model is well suited.

Selection of the fragmentation geometry

As a second step, the shape of the fragmentation pattern is defined by selecting the values of the Dalitz coordinates η_1, η_2. For the simulation of an uncorrelated breakup, these values are chosen randomly within the kinematically allowed, circular region. To test the signature of specific dissociation geometries in the resulting probability distribution of the observables Q_1, Q_2, it is also possible to select at this point fixed values of η_1 and η_2.

After modelling the result of the physical breakup process by selecting the triple of *internal* coordinates $(E_{\text{kin}}, \eta_1, \eta_2)$, we now have to define the six *external* coordinates of the system.

Selection of the external coordinates

The external coordinates of the fragmenting molecular system are given by the three-dimensional position of the point of dissociation in space, and by the overall orientation of the system, which also accounts for three coordinates.

In case of the spatial position, only the distance L between the point of dissociation and the detector surface is of interest here, as the position of the point of dissociation transversal to the beam direction has no influence on the observed internal coordinates $\varepsilon^\perp$, Q_1 and Q_2. This flight length L is, following the geometry of the experimental setup (see Fig. 3.2), randomly chosen from the interval $[5.72\,\text{m}\ldots7.21\,\text{m}]$.

Regarding the overall orientation of the system, an isotropic distribution can be assumed, as the molecular ions are randomly oriented, and the reacting electrons are captured out of a co-moving beam of the same velocity, that is, with no preference of a specific direction. For description of the overall orientation, we thus choose a set of three Euler angles according to a random orientation.

Propagation to the detector position

After defining all coordinates relevant for description of the dissociating system, the three fragments can now be propagated to the imaging detector, that is, their impact positions can be calculated. In a first step, the individual fragment energies E_1, E_2 and E_3 are calculated from the two Dalitz coordinates η_1, η_2 and the total energy E_{kin}. Using these values and the restriction of momentum conservation, the relative fragment velocity vectors $\vec{u}_i$ can be calculated for a certain overall orientation of the system. This orientation is then randomised by a three-dimensional rotation of the velocity vectors using the chosen Euler angles.

Next, the time of flight t is calculated using the known beam velocity v_{beam} and the chosen flight distance L yielding $t = L/v_{\text{beam}}$. Subsequently, the three-dimensional position $\vec{x}_i$ of each fragment in the c.m. frame of the molecule in the moment the c.m. reaches the detector plane can be determined as $\vec{x}_i = t\,\vec{u}_i$.

Modelling of the imaging detector

To simulate the 2D imaging detector, the z-component of each $\vec{x}_i$ which is parallel to the beam direction and normal to the detector plane is discarded now, and only the x- and y-components are used to describe the impact positions.[7]

---

7   The small transversal movement during the time between the impact of the c.m. and the impact of each fragment can be neglected here.

Finally, additional properties of the imaging detector are taken into account: The limited spatial resolution of the detector is included by adding to each position component a random number taken from a Gaussian distribution centered at 0 and with a sigma width adapted to the respective camera system in use at each of the four experiments. This width was found to be in the range of 0.1–0.3 mm.

Another property of the detector to be considered is the minimum distance at which two impinging fragments can be separated. This cutoff distance was found to be in the range of 1–3 mm in the experiments considered here. To include this efficiency of particle separation into the simulation, a minimum tolerable distance d_{min} is calculated for each event following a Gaussian distribution with the center at ~ 3 mm and a sigma width of ~ 1 mm (adapted to the setup in each of the four experiments). If the distance between any two of the three fragments of an event is smaller than d_{min}, the event is discarded.

The simulation algorithm does not model the background contribution due to event mixing and misassigned fragment masses. For each simulated event all three fragments are assumed to be detected, and their masses are assumed to be known (that is, assigned correctly). As described in Sec. 4.3.1, the contribution of this background in the experimental results can be derived directly from the data recorded experimentally, which renders unnecessary a background modelling in the simulation algorithm.

From this point on, the simulated data is further transformed in the same way as the experimental data: For each event, the transversal distances R_i of each fragment from the center of mass are calculated, followed by the transversal KER $\varepsilon^\perp$ and the projected Dalitz coordinates Q_1 and Q_2.

4.3.4 Simulation results

In the following, probability distributions of the observables $\varepsilon^\perp$, Q_1 and Q_2 which result from the simulation algorithm will be discussed regarding their sensitivity to various parameters of the experimental setup and the physical breakup process.

Simulated distributions of the transversal KER

As noted before, the distribution $P(\varepsilon^\perp)$ will be used to estimate the amount of rotational excitations in the ion beam through a comparison of experimental data with simulation results for different assumptions on the rotational excitation (see Sec. 4.4.1). To evaluate the significance of this comparison, it is important to consider the effect of other experimental parameters, besides the rotational energy, on the shape of the $\varepsilon^\perp$ distribution. In this section, a simulation of the three-body breakup following the DR of H_3^+ is used as an example. The beam energy
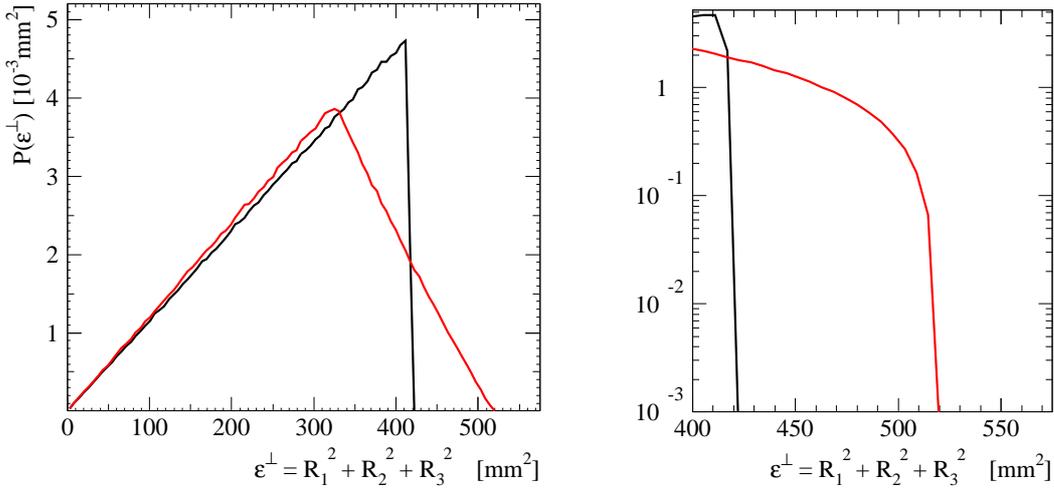
Fig. 4.6: *Simulated transversal KER in the three-body breakup of H$_3^+$. Black: Assuming an ideal 2D detector, and a point-like interaction region. Red: For a realistic extension of the interaction region.*

was set to 1.4 MeV, which is, as the other parameters used in the following, a typical value for experiments at the TSR.

Figure 4.6 (black curve) shows the result of a simulation assuming an ideal 2D detector (that is, infinite resolution and $d_{min} \equiv 0$) and a well defined point of dissociation (zero length of the interaction region). The breakup process is described here by a fixed energy release $E_{kin} = 4.76$ eV and a random dissociation geometry. The projection effect of the 2D detector is clearly visible: While an ideal 3D detector would yield a constant value for the corresponding sum of the squared 3D distances of 420 mm^2 for each event, the transversal KER recorded by the 2D detector follows a broad distribution extending from $\varepsilon^\perp = 0$ to $\varepsilon^\perp = 420$ mm^2.

The next parameter to be considered is the finite length of the interaction region of electron beam and ion beam. The inclusion of this length into the simulation corresponds to a folding of the $\varepsilon^\perp$ distribution with the nearly rectangular-shaped probability distribution of the squared flight length L^2 between the point of dissociation and the detector; the resulting $P(\varepsilon^\perp)$ is shown in Fig 4.6 (red curve). It should be noted that the end-point of the distribution is shifted to higher $\varepsilon^\perp$, but still well defined, as visible in the semi-logarithmic representation.

In Fig. 4.7 (green curve), a typical value for the particle separation efficiency ($d_{min} = 3$ mm, $\sigma_{d_{min}} = 1$ mm) is included in the simulation. As expected, $P(\varepsilon^\perp)$ is reduced for small $\varepsilon^\perp$, while the overall shape as well as the end-point of the distribution remain unaffected. As a last step, the camera resolution is included (Fig. 4.8, blue curve) with a typical value of 0.3 mm. This causes a slight smearing of the whole $\varepsilon^\perp$ distribution, visible mainly at the maximum and near the end-point which is again shifted to higher $\varepsilon^\perp$ and exhibits a considerable slope now.

Finally, the influence of the dissociation geometry on the observed transversal KER is
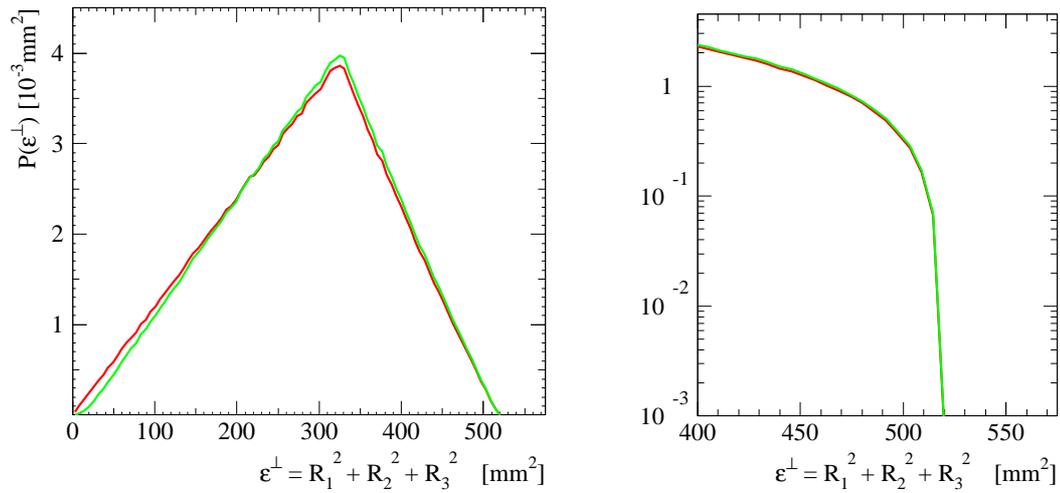
Fig. 4.7: *Simulated KER in the three-body breakup of H_3^+. Red: As in Fig. 4.6. Green: After inclusion of the particle separation efficiency.*
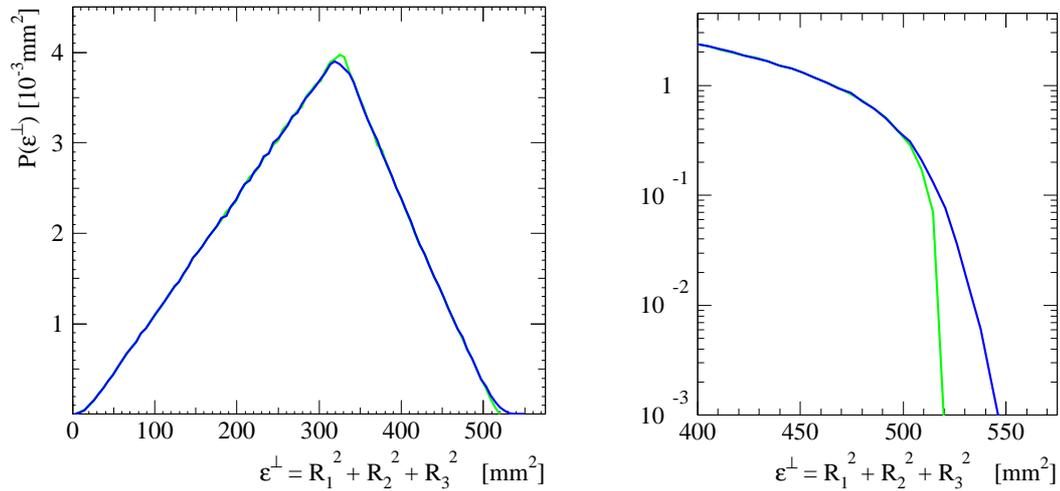
Fig. 4.8: *Simulated transversal KER in the three-body breakup of H_3^+. Green: As in Fig. 4.7. Blue: After inclusion of a typical value for the camera resolution.*

shown in Fig. 4.9. Simulation results are compared for three different fixed geometries (red, green, blue) and for the uncorrelated breakup as assumed before (black). In the overall shape of the $P(\varepsilon^\perp)$ distribution, huge differences are visible between different breakup geometries. For the equilateral-triangular shape (green), there exists no orientation of the fragmenting system which would allow all fragments to hit the same spot on the detector. Thus, $\varepsilon^\perp = 0$ is not possible for this geometry and the corresponding $P(\varepsilon^\perp)$ distribution starts at higher values of $\varepsilon^\perp$. Similarly, the distributions obtained for other geometries can be explained.

Despite the strong sensitivity of the overall shape of $P(\varepsilon^\perp)$ on the dissociation geometry, the semilogarithmic plot reveals that the end-points of all distributions are close together and
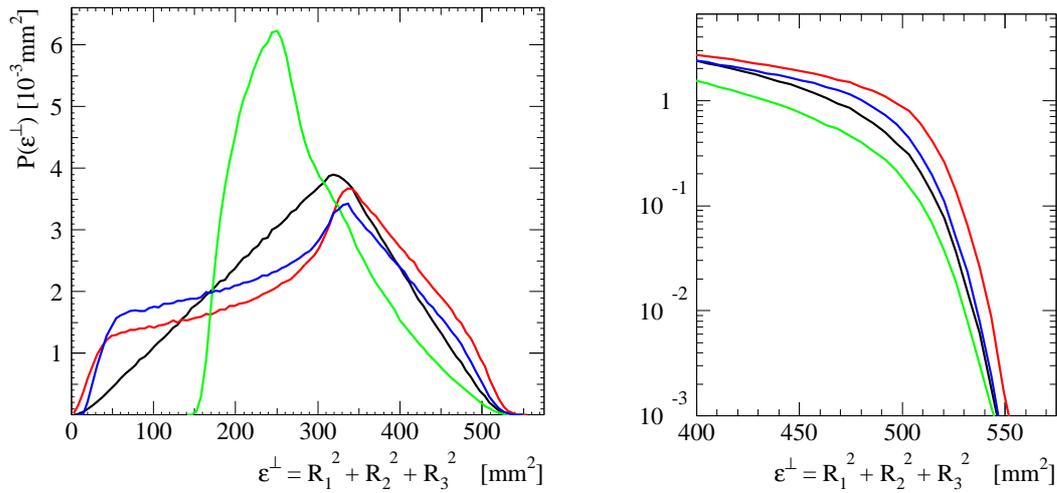
Fig. 4.9: *Simulated transversal KER in the three-body breakup of H_3^+ for different breakup geometries. Black: Random geometries (as in Fig. 4.8). Red, green, blue: Assuming a fixed geometry as indicated by the pictograms.*

also the slopes of the $P(\varepsilon^\perp)$ curves are comparable in this region. This opens up the opportunity to investigate rotational excitations of the H_3^+ molecules even without detailed knowledge of the breakup geometry. The most important signature of rotational energy is found in the end-point region of the $P(\varepsilon^\perp)$ distribution, as will be shown in Sec. 4.4.1 together with the experimental results.

Simulated distributions of the projected Dalitz coordinates

For the geometry information as displayed by Dalitz plots, the uncertainty in the flight length L is irrelevant, as L only affects the overall size of the fragmentation pattern as expressed by $\varepsilon^\perp$. However, the use of a 2D detector at first destroys the advantageous property of the Dalitz type representation to show a uniform event density in case of an uncorrelated breakup. This circumstance is visualised by simulation results for an uncorrelated breakup of H_3^+ in Fig. 4.10. For a hypothetical 3D detector capable of recording the $P(\eta_1, \eta_2)$ distribution, the expected result is shown in Fig. 4.10(a). The detector was assumed here to be able to determine the exact impact times of all fragments. The circular area of the Dalitz plot is then uniformly filled except for small statistical fluctuations and a reduction of the event density close to the geometries where the impact positions of two fragments are very close together (marked by the arrows), an effect of the assumed particle separation efficiency of the detector.

Figure 4.10(b) shows the same uncorrelated breakup reaction, but now simulated for the existing 2D detector system and thus displayed in a *projected* Dalitz plot. Obviously, the $P(Q_1, Q_2)$ distribution is far from being uniform. Along the edge of the circle, correspond-
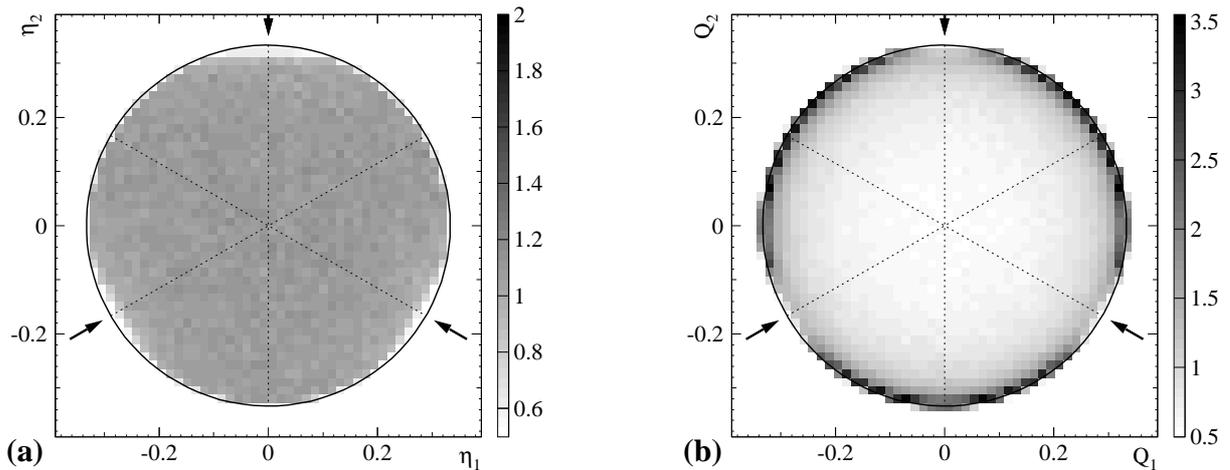
Fig. 4.10: *Dalitz plots for the simulation of an uncorrelated breakup of H_3^+. (a) $P(\eta_1, \eta_2)$ distribution as it would be obtained from a 3D detector, (b) projected Dalitz plot as expected from the 2D detector used in the experiment. Arrows mark the three points along the edge of the circle, which correspond to a geometry with two fragments at the same position. Both plots are normalised such that a uniform filling would yield a constant value of 1.*

ing to a linear shape of the projected fragmentation pattern (cf. Fig. 4.4(b)) the event density obtained is up to a factor 3.5 higher than expected for a uniform filling of the phase space. On the other hand, in the center of the projected Dalitz plot, corresponding to an equilateral shape of the projected fragmentation pattern, the density is reduced by a factor of 2.

While this constitutes a significant deviation from uniformity, an analysis of experimentally observed fragmentation patterns using the (Q_1, Q_2) coordinates can still be performed by the use of *weighted* Dalitz plots as introduced in Sec. 4.3.2. Through the division of the projected Dalitz plot representing the experimental data by the same distribution obtained from a simulation of uncorrelated breakup events, it is possible to identify projected geometries which are preferred or avoided due to the physical breakup process.

The last step necessary for an interpretation of these weighted Dalitz plots is now an analysis of the correlation between the (η_1, η_2) and (Q_1, Q_2) coordinates for specific geometries. Some examples are shown in Fig. 4.11. In the left column, the (η_1, η_2) geometries used in the simulation are marked in a standard 3D Dalitz plot. The right column shows the corresponding simulation results in the form of *weighted Dalitz plots*. The small pictograms visualise the 3D fragmentation geometry corresponding to the (η_1, η_2) values used.

As expected, the weighted Dalitz plots show a certain smearing around the position of the actual 3D geometry due to the fact that a fixed 3D geometry can lead to several projected geometries, depending on the orientation of the system. However, it is noteworthy that the weighted 2D distributions all show clear peaks at the original 3D geometries. Thus, a preference
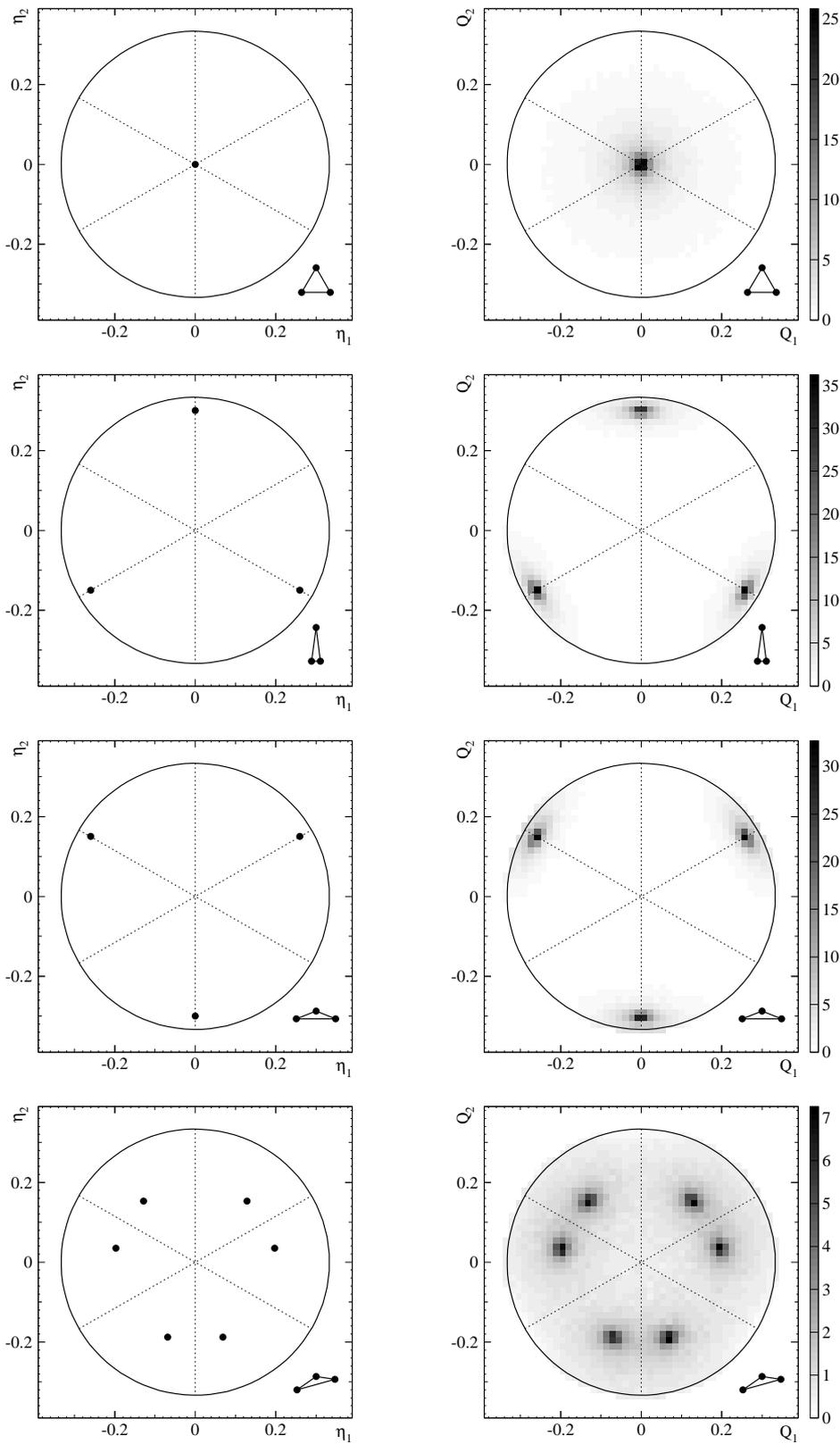
Fig. 4.11: *Simulated fragmentation patterns for specific geometries of H$_3^+$. Left column: (η_1, η_2) values used in the simulation, right column: resulting weighted Dalitz plots, normalised to show a constant value of 1 in case of a uniform filling.*

or avoidance of a certain geometry by the physical fragmentation process would manifest itself in an increased or decreased event density around this geometry also in the weighted Dalitz plot.

Strictly speaking, for an unambiguous interpretation of weighted Dalitz plots some more information is needed. In particular, for any geometry observed in the weighted Dalitz plot, it would be interesting to know the probability of each (η_1, η_2) geometry for being the origin of the observed events. However, this would imply an inversion of the response function describing the transition from (η_1, η_2) to (Q_1, Q_2), which would represent a huge computational effort when aiming at a considerable resolution.

Another possibility to test the significance of weighted Dalitz plots is given by the Monte-Carlo image restoration technique described in [69]. With this method, an unfolding of the experimental projected geometry distributions is achieved for H_3^+ and D_3^+, yielding basically the same results as the weighting scheme presented here. However, the image restoration technique bears some risk of creating artefacts in the restored 3D Dalitz plots, especially in the case of the heteronuclear isotopomers H_2D^+ and D_2H^+. Therefore, weighted Dalitz plots will be used in this work for the presentation of experimental data on all four isotopomers.

4.4 Experimental Results

After developing appropriate methods regarding the data analysis and representation, in this section the experimental results obtained by application of the described techniques will be shown. The presentation concentrates on the results of the fragment imaging experiments regarding the three-body fragmentation channel, as here new techniques were required exceeding the standard analysis procedures applied in fragmentation experiments on diatomic molecules. Other experimental results obtained for the four isotopomers of the H_3^+ ion will be shortly summarised.

4.4.1 Kinetic energy release in the three-body channel

The transversal kinetic energy release $\varepsilon^\perp$ observed experimentally for each of the isotopomers H_3^+, D_3^+, H_2D^+ and D_2H^+ is now compared to the results of simulations adapted to the respective experimental conditions. To estimate the rotational energy present in the experiment, simulations were done assuming three different rotational temperatures: $kT_{\rm rot} = 0\,{\rm eV}$ (that is, $E_{\rm rot} \equiv 0$), $kT_{\rm rot} = 230\,{\rm meV}$ and $kT_{\rm rot} = 500\,{\rm meV}$.

Figure 4.12 shows the comparison for H_3^+. The experimental data are reasonably well described by the simulation assuming $kT_{\rm rot} = 230\,{\rm meV}$, revealing a considerable rotational excitation of the ion beam. Small differences in the overall shape of the $\varepsilon^\perp$ distributions can
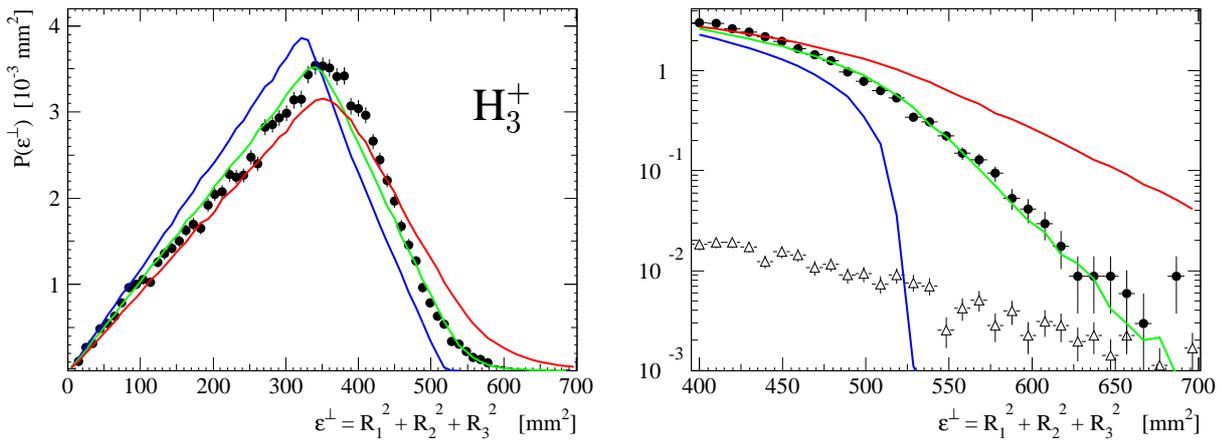
Fig. 4.12: *Kinetic energy release in the three-body breakup of H_3^+. The distribution $P(\varepsilon^\perp)$ is plotted for experimental data taken after 3–10 s of storage (full circles). The lines represent simulations assuming a rotational temperature of $kT_{rot}=0\,eV$ (blue), 230 meV (green) and 500 meV (red). Open triangles depict the estimated background contribution in the experiment.*

be attributed to the distribution of dissociation geometries. As will be seen in Sec. 4.4.2, linear symmetric geometries are preferred for a certain fraction of events. Thus, a deviation from the simulation result for random geometries can be expected, as indicated by the red curve in Fig. 4.9.

In the end-point region of the $\varepsilon^\perp$ distribution, which was shown to be barely sensitive to the breakup geometry, a very good agreement is found between the experimental data and the simulation for $kT_{rot} = 230$ meV. However, keeping in mind the very simple model of a thermal distribution of rotational excitations and a DR rate coefficient independent of rotations, the resulting value of 230 meV can be viewed only as a rough estimate of the rotational energy in the H_3^+ beam.

An additional uncertainty comes from the transformation of the measured fragment distances from camera pixels to mm. While statistical fluctuations of the measured distances (i.e. the resolution of the camera) are included in the simulation, an error in this transformation factor would lead to a systematic stretching of the whole $\varepsilon^\perp$ distribution. In the present experiments, this factor could be determined with an accuracy of $\sim 1\%$, which corresponds to a change of kT_{rot} of roughly 25 meV.

The comparison for D_3^+ (Fig. 4.13) gives basically the same result as found for H_3^+. Also here, the molecular ions carry a strong rotational excitation. In this experiment, data taken at very long storage times of up to 80 sec are available. The comparison of $\varepsilon^\perp$ distributions recorded at two different ranges of storage time shows indications for a slight cooling of the rotational excitations: For long storage times (open circles in Fig. 4.13), the peak of the $\varepsilon^\perp$
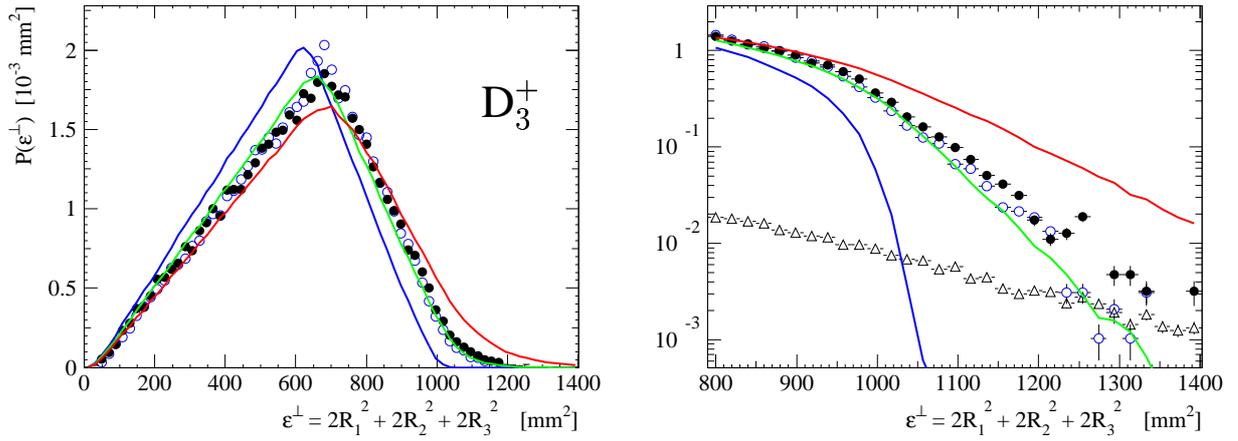
Fig. 4.13: *Kinetic energy release in the three-body breakup of D_3^+. The distribution $P(\varepsilon^\perp)$ is plotted for experimental data taken after 10–25 s of storage (full circles) and 45–80 s of storage (blue open circles). The lines represent simulations assuming a rotational temperature of $kT_{rot} = 0\,eV$ (blue), 230 meV (green) and 500 meV (red). Open triangles depict the estimated background contribution in the experiment.*
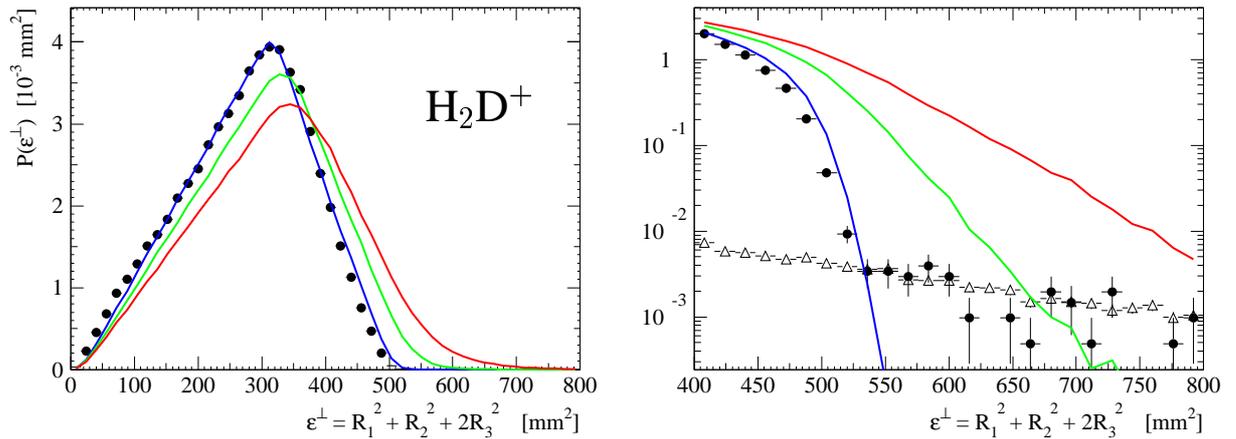
Fig. 4.14: *Kinetic energy release in the three-body breakup of H_2D^+. The distribution $P(\varepsilon^\perp)$ is plotted for experimental data taken after 5–15 s of storage (full circles). The lines represent simulations assuming a rotational temperature of $kT_{rot} = 0\,eV$ (blue), 230 meV (green) and 500 meV (red). Open triangles depict the estimated background contribution in the experiment.*

distribution is sharper and the slope in the end-point region is steeper, both indicating a slightly lower rotational temperature than for the short storage times (full circles).

For the two heteronuclear isotopomers H_2D^+ and D_2H^+, a completely different behaviour is observed (Figs. 4.14 and 4.15). The experimental data (full circles) here are consistent within the uncertainties with a rotationless simulation (blue curve). The dissociation events observed at $\varepsilon^\perp$ values higher than the end-point of this simulated data set can well be explained taking into account the background in the experimental data due to event-mixing or misassignment of the
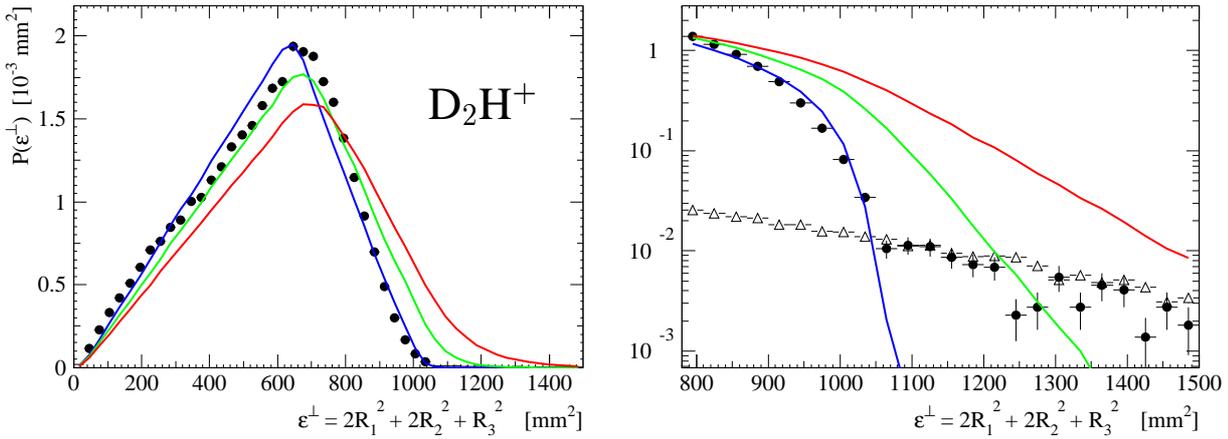
Fig. 4.15: *Kinetic energy release in the three-body breakup of D$_2$H$^+$. The distribution $P(\varepsilon^\perp)$ is plotted for experimental data taken after 10–60 s of storage (full circles). The lines represent simulations assuming a rotational temperature of $kT_{\rm rot}=0$ eV (blue), 230 meV (green) and 500 meV (red). Open triangles depict the estimated background contribution in the experiment.*

H and D fragments. As described in Sec. 4.3.1, this background contribution can be estimated from the experimental data (open triangles). The data recorded in the high-$\varepsilon^\perp$ region obviously has its origin in this misassignment background.

Because of the uncertainties in the experiment, a rotational excitation of the ions cannot be completely excluded. Taking into account especially the uncertainties in the calibration of camera pixels per mm and in the spatial resolution of the camera, an upper limit on the order of $kT_{\rm rot}=75$ meV can be deduced from the present experiments for the rotational temperatures of H$_2$D$^+$ and D$_2$H$^+$. For both molecules, no storage time dependence of the $\varepsilon^\perp$ distribution could be observed.

Additional evidence for rotational excitations of the ion beam was found in the analysis of two-body breakup events for the homonuclear isotopomers H$_3^+$ and D$_3^+$ (Sec. 4.4.3) and in measurements of the DR rate coefficient α (Sec. 4.4.4). An interpretation of the experimental findings presented here in the light of recent theoretical calculations will be given in Sec. 4.5.

4.4.2   Breakup geometry in the three-body channel

The geometry distribution of the three-body breakup for the four isotopomers is shown in Figs. 4.16 and 4.17 represented by weighted transversal Dalitz plots as introduced in Sec. 4.3.2. After assignment of the fragment masses as described in Sec. 4.3.1, the data set for each molecule was here additionally symmetrised with respect to permutations of identical fragments, to avoid artificial structures introduced by the arbitrary numbering of these fragments during the processing of the CCD camera image. A consideration of the shape of background
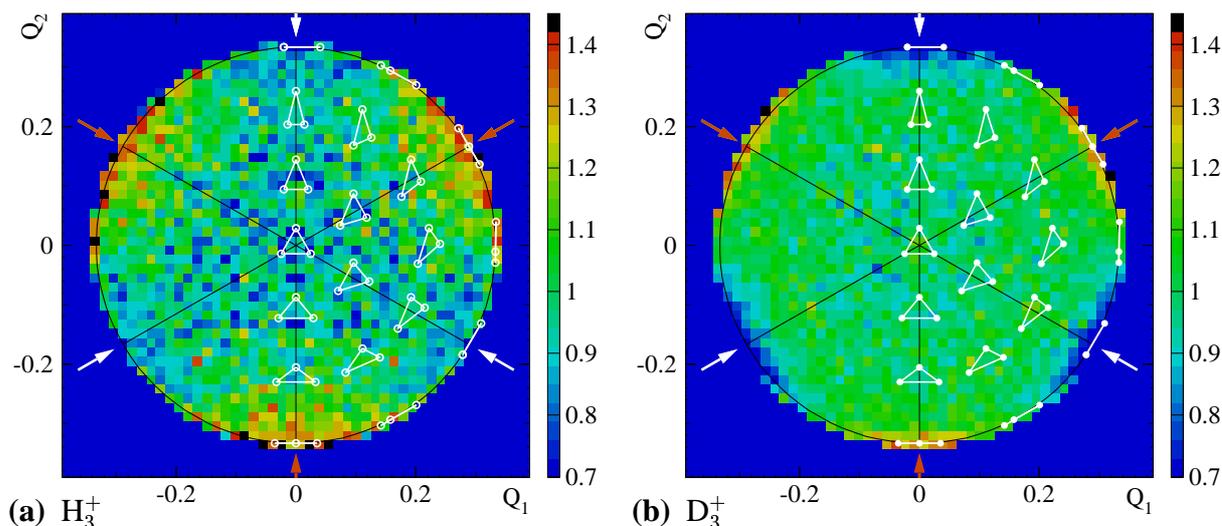
Fig. 4.16: *Weighted Dalitz plots, as introduced in Sec. 4.3.2, for the experimentally observed three-body breakup of the homonuclear isotopomers H_3^+ (a) and D_3^+ (b). The plots are normalised to yield a value of 1 for an uncorrelated breakup. Black lines denote symmetry axes.*
The small pictograms give the projected geometry of the breakup as seen on the detector, for selected points of the Dalitz plot. The arrows mark special linear geometries at the circumference of the circle: White: The two-body breakup geometry, where two of the three fragments have zero distance. Red: The linear symmetric case, where the central fragment stays at rest, while the two outer fragments have equal absolute velocities, momenta and energies in the c.m. frame of the system.

events, as was done for the KER results, is not needed here, since the small ($\sim 1\%$) contribution of background events has a significant influence on the experimental results only when considering structures represented by only a small fraction of the experimental data. This was the case when analysing the high-energy tails of the $P(\varepsilon^\perp)$ distributions, but as will be seen does not apply for the geometry distributions discussed here.

In all four plots, a clear preference of linear symmetric breakup geometries is visible, with the central particle preferably being a D atom for the heteronuclear isotopomers.

For the homonuclear species, the Dalitz plots shown in Fig. 4.16 exhibit a sixfold symmetry reflecting the six possible permutations of the three identical particles. In both cases, a tendency to linear breakup geometries (plotted along the circumference of the circle) is observed in strong contrast to the shape of the molecular ion before the breakup, which is that of an equilateral triangle for all isotopomers (corresponding to the origin of the Dalitz plot). In addition, configurations close to the symmetric case where one fragment stays at rest in the co-moving c.m. frame, while the other two have momenta of equal magnitude and opposite direction (indicated by the red arrows), are in favour compared to geometries where two of the fragments are close together (that is, near the two-body fragmentation geometry indicated by
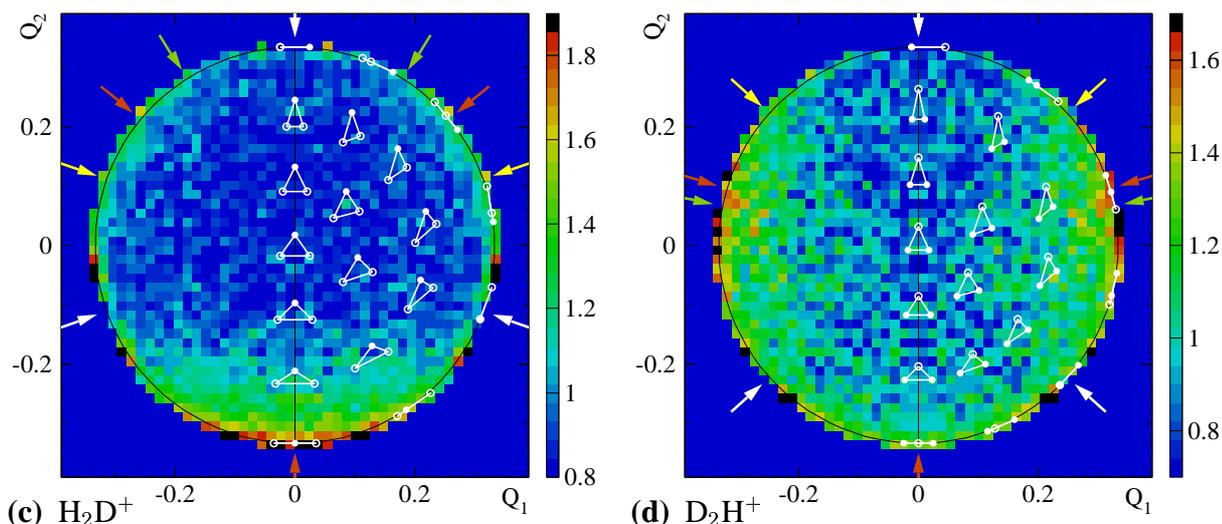
Fig. 4.17: *Weighted Dalitz plots for the experimentally observed three-body breakup of the heteronuclear isotopomers H$_2$D$^+$ (a) and D$_2$H$^+$ (b). The small pictograms give the projected geometry of the breakup as seen on the detector, for selected points of the Dalitz plot. Open circles represent H, full circles D atoms.*
The arrows mark special linear geometries at the circumference of the circle: White: *The two-body breakup geometry, where two of the three fragments have zero distance.* Red: *The linear symmetric case, where the two outer fragments have equal absolute velocities in the c.m. frame.* Yellow: *The case of equal momenta of the two outer fragments; here the center fragment stays at the c.m. position.* Green: *Equal energies of the two outer fragments.*

the white arrows).

It has to be pointed out that this avoidance of small fragment distances is not an artefact introduced by the detector efficiency. The limited ability of the camera to separate fragments impinging at small mutual distances is reducing the acceptance of the detector only for geometries very close to the two-body geometry. In addition, the weighting procedure provides a first-order correction of any geometry-dependent detector efficiencies. As was seen in Fig. 4.11 (second and third row), geometries in the vicinity of the two-body configuration on one hand, and close to the linear geometry on the other hand, are equally well represented by a weighted Dalitz plot.

Comparing the results for H$_3^+$ and D$_3^+$, the overall anisotropies of the breakup geometry appear to be weaker in the case of D$_3^+$ (the same colour scale was chosen for these two molecules for easier comparison). Interesting details are found for two geometries: Firstly, close to the two-body geometries, the reduction of the observed event rate is much stronger for D$_3^+$ than for all other isotopomers. Secondly, for equilateral geometries, a slightly increased event rate is observed for D$_3^+$ in contrast to H$_3^+$, where the distribution exhibits a small dip at this geometry.

The latter effect is not very pronounced in the weighted transversal Dalitz plots presented here, but was observed also when using the Monte Carlo restoration method [69].

In case of the heteronuclear species, the symmetry of the system is reduced to the exchange of the two identical fragments manifesting itself in a single symmetry axis along Q_1=0 in the weighted Dalitz plots, Fig. 4.17. According to the generalised definition of the Dalitz coordinates for $m \neq m_3$ (4.14), also the geometrical interpretation of points in the plots changes. This is taken into account in the positioning of the pictograms and arrows in the figures. In the case of a linear breakup geometry with the two outer fragments being of different mass, there are now three possible definitions of a *symmetric* breakup: The outer fragments can be required to possess equal absolute values of velocity, momentum or energy with respect to the center of mass. These geometries are indicated now by red, green and yellow arrows, respectively.

The experimental data again show a preference of linear, symmetric geometries. For H_2D^+, the H-D-H configuration with the D fragment at rest is most likely, while only a small increase of the probability distribution is found at other linear geometries, including the various symmetric H-H-D configurations. Compared to the case of H_3^+, the trend to a linear breakup appears more pronounced here than the trend to a symmetric breakup. The distribution for D_2H^+ peaks close to the linear D-D-H configuration with symmetric energies of the outer fragments, which is also close to the symmetric velocity case, but clearly different from symmetric momenta. At the D-H-D configuration, only a much smaller increase of the event rate is observed.

The preference of linear symmetric dissociation geometries thus appears to be a general feature shown by all four isotopomers. For the heteronuclear species, a quantitative difference of this preference for geometries exhibiting a central H or D atom could be expected. However, the *complete absence* of such a peak for linear symmetric geometries with a central H atom is surprising.

The observed deviations from an uncorrelated breakup geometry have some effect on the transversal KER distributions $P(\varepsilon^\perp)$ discussed in Sec. 4.4.1. The simulation results shown there for comparison with the experimental data were obtained assuming uncorrelated breakup geometries, which turns out to be different from the experimental situation. On the other hand, the use of correlated 3D geometries in the simulation, which are adapted to the experimental findings would imply a *quantitative* analysis of the structures observed in the experimental Dalitz plots, which is not provided in a reliable way by the weighting method.

However, the conclusions reached in Sec. 4.4.1 concerning the rotational excitation still hold, as they are based especially on the behaviour of the $P(\varepsilon^\perp)$ distribution at large $\varepsilon^\perp$, where the influence of the breakup geometry was shown to be only a minor perturbation.
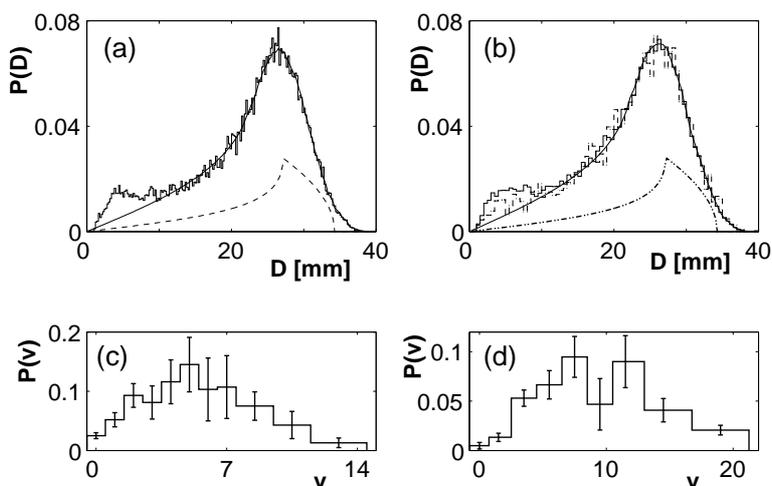
Fig. 4.18: *Distributions of observed fragment distances D in the two-body breakup of H$_3^+$ (a) and D$_3^+$ (b). Dashed lines show the expectation for a single vibrational state of the molecular fragment, solid lines are a fit to the experimental data which are shown as histograms. The dashed histogram in (b) represents data taken after a longer storage time. (c) and (d) show the vibrational state population resulting from the fit. Figure taken from [42].*

4.4.3 Kinetic energy release in the two-body channel

The KER in the two-body breakup channel can in principle be analysed with standard techniques usually applied for fragmentation experiments with diatomic molecules [3]. In the case of the two-body breakup of a triatomic molecule, however, as an additional step each event used in the analysis has to be verified to origin indeed in the two-body breakup process rather then in the three-body process with one of the fragments remaining undetected. This channel identification is done by a cut on the c.m. position of each event as described in Sec. 4.3.1.

For the homonuclear isotopomers, the KER in the two-body channel could thus be analysed (see Fig. 4.18). From the observed spectrum of fragment distances, the vibrational excitation distribution of the emerging molecular fragments could be deduced. In addition, an increased event rate at very small KER values was found for both H$_3^+$ and D$_3^+$. These events could be attributed again to a substantial rotational excitation of the molecular ion beam. Ions with a very high rotational energy of $\gtrsim 1\,\mathrm{eV}$ have the possibility to dissociate into H$_2$ + H($n = 2$), leaving the atomic fragment in an electronically excited state. For rotational excitation energies close to the threshold for this process, the resulting KER is very small, as observed in the experiment. For the case of D$_3^+$, the dashed histogram in Fig. 4.18(b) again indicates a slight cooling of the rotational excitations. A detailed description of the analysis of the two-body channel for H$_3^+$ and D$_3^+$ is given in [69].

For the heteronuclear isotopomers, the separation of the two-body channel from background in the form of partly detected three-body events becomes much more difficult. In each of these cases, two two-body channels with different composition of the molecular fragment exist. This leads to up to four possible c.m. positions for each pair of fragments detected and thus to a much higher chance for a background event to accidentally pass the c.m. cut. For these reasons, a clean channel separation was not possible for the heteronuclear species and no further information

could be gained from an analysis of two-body events.

4.4.4 Rate coefficient measurements

For a further investigation of rotational excitations, a separate series of experiments was performed where the DR rate coefficient α was monitored over long storage times for H_3^+ and D_2H^+. In both cases, a dependence of α on the storage time was observed, which could be interpreted as the result of a storage time dependent distribution of rotational excitations in combination with a dependence of α on these rotational excitations. For D_2H^+, some indications for a thermalisation to the ambient 300 K blackbody radiation were found [43]. In addition, measurements performed after a long time of interaction with a strong beam of cold electrons suggest the preparation of a subthermal rotational state distribution. In the case of H_3^+, similar effects of electron interactions were observed, suggesting also here the possibility of a rotational cooling of the ensemble by low-energy electron collisions. The influence of collisions with higher energetic electrons as well as residual gas particles on the rotational distribution is currently under investigation. More details on these rate coefficient measurements can be found in [43, 83].

4.5 Comparison to theory

4.5.1 Rotational excitations

The different behaviour of the homonuclear vs. the heteronuclear isotopomers concerning rotational excitations can be understood taking into account the different symmetry properties of these molecules. The strongly exothermic formation reaction (4.1) can be expected to produce all isotopomers in highly rovibrationally excited states. The level of excitations found in storage ring experiments then depends on the lifetime of the excited states compared to typical storage times ranging from few seconds up to several tens of seconds.

For the homonuclear species H_3^+ and D_3^+, the center of mass coincides with the center of charge of the molecule. These molecules therefore do not possess a permanent electrical dipole moment which would allow for the de-excitation of rovibrational excitations via emission of electrical dipole radiation. The resulting high lifetimes of rovibrational excitations can be modelled in the case of H_3^+ [38] using *ab initio* calculations of transition rates [54]; a similar behaviour can be expected for D_3^+. This model predicts the relaxation of vibrational excitations within the first seconds of storage, which was confirmed in a Coulomb Explosion Imaging experiment [38]. For the rotational excitations, a significant population of high-lying states (average energy 260 meV) was calculated to remain even after a hypothetical, very large storage

time of 30 min [37].

A certain effect on the rotational distribution might be expected also from the constant interactions with the electron beam, on one hand by selective depletion of strongly recombining states and on the other hand by inelastic electron scattering processes, which were e.g. found to dominate the vibrational cooling of H$_2^+$ and D$_2^+$ [40]. Indeed, a small reduction of the contribution from rotationally excited states is observed in the data taken after long storage times for D$_3^+$. However, a considerable excitation involving even high-lying states is still found even after more than one minute of storage.

For the heteronuclear species H$_2$D$^+$ and D$_2$H$^+$, the situation is different. While the geometric structure including the electronic wave functions is similar for all isotopomers, the center of mass is shifted for these species due to the different nuclear masses. This results in an permanent electrical dipole moment and thus allowed transitions between rovibrational states exist. The transition rates calculated e.g. for D$_2$H$^+$ indicate typical decay times in the order of 10 ms for vibrational excitations, while rotational lifetimes are expected to be $\lesssim 1$ sec at excitation energies $\gtrsim 120$ meV, and $\gtrsim 10$ sec at $\lesssim 60$ meV [49]. The observation of a rotational temperature below 50 meV (corresponding to an average excitation energy of ≤ 75 meV) after several seconds of storage is thus in good agreement with the theoretical expectations.

4.5.2 Breakup dynamics

The observed preference of linear symmetric breakup geometries in the three-body channel can tentatively be connected to the potential energy surfaces of the neutral H$_3$ system as used by Kokoouline and Greene [36]. Figure 4.19 shows the lowest of these PES using normal coordinates similar to Eq. (4.15). The origin of the plot represents the equilateral equilibrium geometry of H$_3^+$, which is the starting point of the dissociation process. Similar to Dalitz plots, linear configurations would be represented along the edge of the kinematically allowed region in the (Q_x, Q_y) plane, which in this case corresponds to a triangular shaped area slightly exceeding the range shown in Fig. 4.19. Isosceles geometries in this plot correspond to ϕ values of $90°$, $-30°$ and $-150°$. A linear symmetric geometry would for example be represented by the point $(Q_x, Q_y) = (3.77, 0)$.

The DR process is described here as follows: After the incoming electron is captured into a Rydberg state of H$_3$ which is geometrically and energetically close to the H$_3^+$ ground state, the system is believed to descend down to the 2pπ surface, which is energetically open for dissociation, by transferring energy into the vibrational degrees of freedom.

Remarkably, the lowest 2pπ_1 surface has, at the initial value of s_1 (which can be viewed as a hyperradius), its minima at the geometry of an isosceles triangle with the largest angle measuring $\sim 80°$. A similar behaviour is observed for the 3pπ_1 Rydberg state (see [36]), which
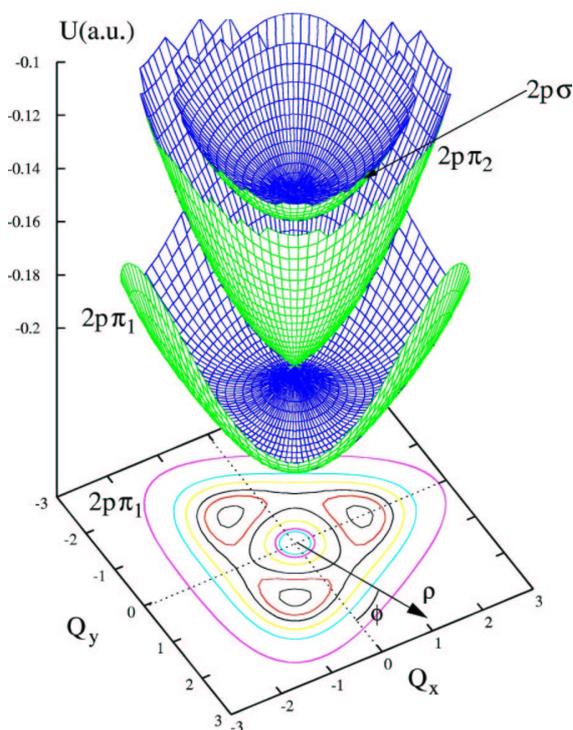
Fig. 4.19: *The three lowest PESs of H_3 in dimensionless normal coordinates describing the shape of the triangular arrangement of the nuclei. $(Q_x, Q_y) = (fs_x, fs_y)$ with $f = 2.64$ bohr^{-1} and the s_x, s_y defined in Eq. (4.15). The third coordinate s_a which describes the overall size of the system was fixed at $s_a = 3r_{ref}$ with the equilibrium internuclear distance $r_{ref} = 1.65$ bohr of the H_3^+ ion. Picture taken from [36].*

is probably an intermediate state during the descent. The final breakup geometry reached at macroscopic separation of the fragments of course depends not only on the shape of this two-dimensional cut of the PES at the initial value of s_1, but also on the development of the $2p\pi$ surface for higher hyperradii. However, from the theoretical data available now, the kinetic energy available for the nuclei at least in this part of the surface seems to be higher for deformed shapes, which break the original symmetry of an equilateral triangle but maintain an isosceles shape while moving to a more obtuse angled triangle. In this light, the experimental observation of a tendency towards linear symmetric geometries may appear not too surprising.

For the heteronuclear species, besides the same preference of linear symmetric breakup geometries, a breakdown of the symmetry under permutation of the fragments was observed in the experiment, with the central position in the linear arrangement being preferably assumed by a D atom. In first approximation (that is, in the Born-Oppenheimer case), the electronic surfaces of the anionic as well as the neutral system should be identical for all isotopomers. On the other hand, the non-Born-Oppenheimer Jahn-Teller coupling was found to play a crucial role in the theoretical treatment of the DR process for H_3^+ [36]. Thus the appearance of asymmetries in the PES seems possible for H_2D^+ and D_2H^+, which could be connected to the observed symmetry breaking. Another possible explanation is that, even when assuming a completely symmetric PES, the force driving the breakup, which is initially equal for all fragments, will cause a much smaller acceleration when acting on a heavy D fragment than for a H fragment, thus breaking the

fragment permutation symmetry. Depending on the behaviour of the PES at the slightly changed geometry, this effect could be amplified, finally leading to a strong preference of arrangements with a D fragment at the central position and possibly even to the complete disappearance of any peak at linear-symmetric shapes with a central H atom, as observed in the experiment.

For a more instructive comparison with theory, concerning both the preference of linear symmetric geometries and the symmetry breaking in the heteronuclear isotopomers, detailed calculations of the fully three-dimensional wave packet propagation would be needed for all four isotopomers on their respective PES.

4.6   Conclusions

The dissociative recombination of the four isotopomers of the H$_3^+$ molecular ion was investigated in a series of experiments employing fast, stored beams of these ions. The breakup energetics and geometries in the two- and three-body dissociation channels were investigated using neutral fragment imaging techniques. With the help of advanced methods of data analysis which are necessary in the present case of fragmentation experiments on polyatomic ions, new results could be obtained regarding the internal excitation of the stored molecular ions and the dynamics of the fragmentation process.

Through a detailed analysis of the kinetic energy release in the three-body fragmentation channel, a significant rotational excitation was revealed for the homonuclear species H$_3^+$ and D$_3^+$ but not in case of the heteronuclear H$_2$D$^+$ and D$_2$H$^+$ molecules. This excitation can have a substantial influence on storage ring measurements of the rate coefficient α of this astrophysically important DR reaction. Therefore the diagnostics and the control of rotational excitations has become an important issue in storage ring experiments on H$_3^+$, concerning the production of the ions, the evolution of such excitations during the time of storage, and the consequences regarding DR reactions studied with these ions (see, e.g. [37, 38, 43, 48]).

Regarding the fragmentation geometry in the three-body channel, a clear preference of linear symmetric fragmentation patterns was observed for all four isotopomers. For both heteronuclear molecules, an additional symmetry breaking was found in the preference of a D atom at the central position in this linear arrangement. These results are expected to serve as additional benchmark tests for detailed theoretical models of the DR process.

The picture is completed by the data obtained from the two-body fragmentation channel for H$_3^+$ and D$_3^+$. These support the finding of high rotational excitations of the homonuclear ions and, with the vibrational excitation spectrum of the emerging molecular fragments, provide an additional detail of the studied reaction for comparison with theory.

5. Electron-impact detachment from LiH$_2^-$

5.1 Introduction

As a second example for the fragmentation of a triatomic molecular ion, the dissociative electron-impact detachment from LiH$_2^-$ is studied. As described in Chap. 2, the electron detachment process is in many aspects different from the dissociative recombination reaction as investigated for H$_3^+$ in Chap. 4. However, also in this case the electron collision results in a change of the charge state of the molecular system. Thus, the potential energy surfaces (PES) which determine the evolution of the molecular geometry are abruptly changed from the anionic ground state PES, on which the system had relaxed to a state close to the equilibrium geometry, to a neutral PES, which then drives a dissociation of the system, as will be seen.

Although, similar to H$_3^+$, LiH$_2^-$ is a very fundamental small molecule (it is the simplest heteronuclear triatomic system apart from the isotopic variants of H$_3^+$), the prior knowledge on the specific reaction under study is much more limited here than in the H$_3^+$ case. For H$_3^+$, the new investigations concentrated on a detailed analysis of the fragmentation dynamics within the known final channels and on the diagnostics of excitations of the original molecular ion. In contrast to that, the fragmentation of the LiH$_2$ system after electron detachment from the LiH$_2^-$ anion was studied experimentally for the first time here. Even though some theoretical work is available, no conclusive prediction was possible as to which exit channels (in terms of charge states and molecular compositions of the fragments) would occur in the experiment. The studies on LiH$_2^-$ thus focus on the determination of possible exit channels of the electron detachment process, as well as measurements of their relative contribution under various experimental conditions.

5.1.1 Previous studies of the LiH$_2^-$ system

The LiH$_2^-$ ion has raised interest in theoretical and experimental fields for various reasons. Because of its relatively simple structure, it served as an example in studies of the structure and the reactions of several classes of molecules. Senekowitsch and Rosmus [65] studied the structure of LiH$_2^-$ as an example of a molecular anion which is formed in a reaction of a molecule

exhibiting a permanent electrical dipole moment (LiH) with an anion (H$^-$). For the first time, they calculated (in 1987) the molecular anion to be stable, with a linear H-Li-H equilibrium structure. Earlier calculations by Preuss and Diercksen in 1967 had resulted in a metastable structure [62].

Another point of view was adopted by Boldyrev and Simons [9], who investigated molecular anions of MH$_{k+1}^-$ type, where M is a nontransition atom (e.g. Li, Na, Be, Mg) with a maximal formal valence of k. The corresponding neutral species MH$_{k+1}$ thus are hypervalent and, in general, unstable. The additional electron of the anionic species was found to be bound by as much as several eV and to stabilise the system against dissociation. This behaviour is attributed to the insertion of the electron into a binding HOMO[1] distributed over several hydrogen atoms.

The instability of the neutral LiH$_2$ system makes not only the structure of LiH$_2^-$, but especially also the electron detachment from the anion an interesting test case, as the dynamics of the subsequent dissociation process are determined by the same potential energy surfaces which govern the neutral reaction LiH + H $\leftrightarrow$ Li + H$_2$. This reaction plays an important role in the chemistry of the early universe [68], where a considerable abundance of LiH could have far-reaching consequences up to the erasure of anisotropies in the cosmic background radiation through Thomson scattering. As one of the simplest chemical reactions, it has also some benchmark character and is subject of ongoing experimental [15] and theoretical [46, 34] studies.

In a recent calculation, Sharp and Gellene [66] studied the LiH$_2^-$ ion in the context of the reaction of up to three hydrogen molecules with Li$^-$ as well as the isoelectronic B$^+$. Besides the known structure of the covalently bound anion, another minimum of the anionic ground state PES was found, giving rise to the very weakly bound electrostatic complex Li$^-$(H$_2$) [14].

This variety of theoretical approaches reveals a large interest in the LiH$_2^-$ / LiH$_2$ system. On the other hand, experimental results available up to now are limited to the mass-spectroscopic detection of the anion [26] and very recent studies of the neutral reaction Li($2p$) + H$_2(v\!=\!1)$ $\rightarrow$ LiH($X\,^1\Sigma^+$) + H [15]. Therefore an experimental study of the electron detachment from the anion is expected to yield valuable new results for comparison and addition to the theoretical work.

5.1.2 Energy levels of the LiH$_2^-$ / LiH$_2$ system

A schematic overview of some energy levels relevant for the LiH$_2$ and LiH$_2^-$ system is given in Fig. 5.1, using the energies listed in Tab. 5.1. The covalently bound LiH$_2^-$ molecule is stable against both autodetachment of an electron and dissociation into smaller fragments. The

---

1   Highest Occupied Molecular Orbital
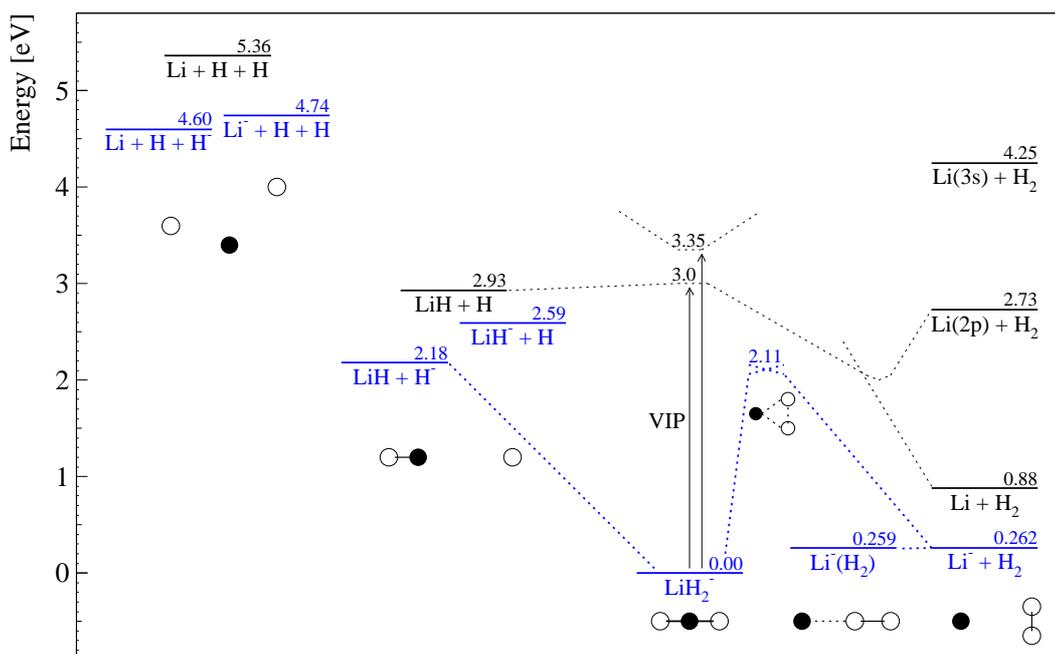
Fig. 5.1: *Energy levels in the LiH_2^- anion (blue) and the LiH_2 neutral system (black). All energies are given relative to the LiH_2^- molecule assuming the rovibrational ground state for all molecules and infinite separation of unbound fragments, using the values listed in Tab. 5.1. The pictograms visualise the nuclear geometries of some configurations, with the filled circle denoting the Li atom. For unbound fragments, the mutual orientation is arbitrary. VIP denotes the vertical ionisation potential at the LiH_2^- equilibrium geometry. The dotted lines schematically indicate important properties of some calculated PES.*

equilibrium geometry was found to be linear symmetric with a Li-H bond length of 3.3 bohr [66].

The adiabatic dissociation energy D_0 of LiH_2^- into $Li^- + H_2$ is calculated to be only 0.26 eV. However, to reach this dissociation channel, a significant barrier in the potential energy surface has to be overcome. On this three-dimensional PES, the minimum energy pathway which connects the LiH_2^- and $Li^- + H_2$ geometries follows the C_{2v} symmetry of an isosceles triangle and reaches a maximum energy of 2.11 eV at a conical intersection of the two lowest electronic surfaces of the anionic system [66]. While these two surfaces have the same symmetry (A') with respect to the C_S group corresponding to a general triangular arrangement of the nuclei, and thus avoid any crossing, in the special case of isosceles geometries considered here, which is described by the C_{2v} group, the symmetry properties of the two PES are different (A_1 and B_2) and thus a crossing is allowed. Interestingly, this crossing takes place at the geometry of an equilateral triangle, which – apart from the symmetry breaking by the additional inner electronic shell of the Li atom – corresponds to the same C_{3v} symmetry which also governs the crossing of the two lowest PES of H_3 (cf. Fig. 4.19).

Quantity	Species	Value [eV]	Reference
Electron affinity	H	0.754	[5]
	Li	0.618	[5]
	LiH	0.34(1)	[64]
Dissociation energy^a D_0	H$_2$	4.478	[21]
	LiH	2.429	[72]
	LiH$_2^-$	0.262^b	[66]
	Li$^-$(H$_2$)	0.0028^b	[14]
Vertical ionisation potential (VIP)	LiH$_2^-$	3.0(1)	[9]

a Including any zero-point energies.
b With respect to the Li$^-$ + H$_2$ channel.

Tab. 5.1: *Energies relevant for the LiH$_2$ and LiH$_2^-$ system.*

At a linear geometry close to the Li$^-$ + H$_2$ configuration, the electrostatic complex Li$^-$(H$_2$) is predicted, which has a dissociation energy as low as 3 meV [14]. For the separation of one of the hydrogen atoms from the LiH$_2^-$ molecule, leading to the LiH + H$^-$ asymptotic channel, an adiabatic dissociation energy of $D_0 = 2.2$ eV can be deduced from the values given in Tab. 5.1. For this transition no energy barrier was reported. Facing these energetic constraints, the LiH$_2^-$ molecule can thus expected to be stable, with an excitation energy of more than 2 eV needed to initiate a fragmentation.

A neutralisation of this anionic system can be achieved through the detachment of an electron from one of the two valence orbitals, labelled $1\sigma_u$ and $1\sigma_g$ in the $D_{\infty h}$ symmetry corresponding to the linear symmetric geometry of the anion. Through this electron detachment, the wave function describing the nuclear conformation of the anion is vertically projected on a PES of the neutral LiH$_2$ system, eventually starting to propagate to one of the dissociative channels.

The vertical ionisation potential (VIP) of LiH$_2^-$ describes the energy needed for a transition, at the geometry of the anion, to the lowest lying neutral PES (corresponding to the detachment of a $1\sigma_u$ electron), and was calculated to 3.0±0.1 eV [9]. The neutral PES reached by this transition has no minimum at the anion geometry, and the system is expected [9] to dissociate into the Li + H$_2$ channel. Again, an intersection of the two lowest states is involved, as schematically shown in Fig. 5.1. The second two-body dissociation channel, LiH + H, has an energy very close to the VIP. Here a more detailed description of the neutral PES would be necessary to estimate the possibility of a dissociation into this channel.

The detachment of an electron from the $1\sigma_g$ orbital needs the slightly higher energy of 3.35 eV [9] and leads to a neutral PES which exhibits a local minimum at the anion geometry.

However, the lifetime of such an electronically excited state can be expected to be at most in the nanosecond range. Thus, a transition to the neutral ground state PES and a subsequent fragmentation of the system will take place shortly after the detachment process and an observation of this bound, exited LiH_2 state in the experiment is not expected.

The three-body fragmentation channel $Li + H + H$ has an asymptotic energy of $5.4\,eV$. Therefore a dissociation into this channel would require a transition into a highly excited PES of the neutral system, which would have to allow the nuclear wave packet to reach large separations of all three fragments before changing to a lower lying electronic PES. Such a situation cannot be achieved in the simple picture of the sudden removal of one electron, but needs a more complicated interaction involving more than one of the electrons of the anion.

In summary, the dissociative electron detachment of LiH_2^- is expected to lead mainly to the $Li + H_2$ dissociative channel. However, taking into account the limited *a priori* knowledge on the interaction process and the neutral potential energy surfaces involved, other dissociation channels cannot be excluded. Moreover, the role of dissociative excitation reactions which could produce negative fragments is difficult to estimate. Senekowitsch and Rosmus [65] give a vertical excitation energy of $2.4\,eV$ for the transition to the first electronically excited anion state from the LiH_2^- ground state. Depending on the structure of this excited PES, this transition could then give rise to a dissociation into neutral and negative fragments.[2]

An important goal of the present experimental investigation of this reaction therefore will be the identification of the channels mainly contributing to the dissociation process.

5.2 Experimental setup

For the experiments on LiH_2^- presented here, the setup at the TSR as described in Sec. 3.3.1 was used. A major change compared to the standard setup was the reversal of the polarity of all magnetic and electrostatic steering and focusing devices, which was necessary for acceleration and storage of the negative ions.

The LiH_2^- ions were produced using a standard cesium sputtering negative ion source of MISS type which was modified for operation with the high current injector. Acceleration was achieved again using only the two RFQ modules, reaching a final energy of $4.5\,MeV$ for this ion. The ions were then stored in the TSR for up to $15\,sec$ and overlapped with a co-moving electron beam at the electron cooler (see Sec. 3.3.1).

Regarding the fine tuning of the settings of the storage ring and the electron cooler, some technical difficulties had to be overcome. Usually, the exact positioning and focusing of the ion

---

2   New calculations (see Sec. 5.4.1) yield an excitation energy of $3.3\,eV$. The excited anionic PES is found above the first neutral PES, thus auto-detachment of an electron and the breakup into neutral fragments is possible.
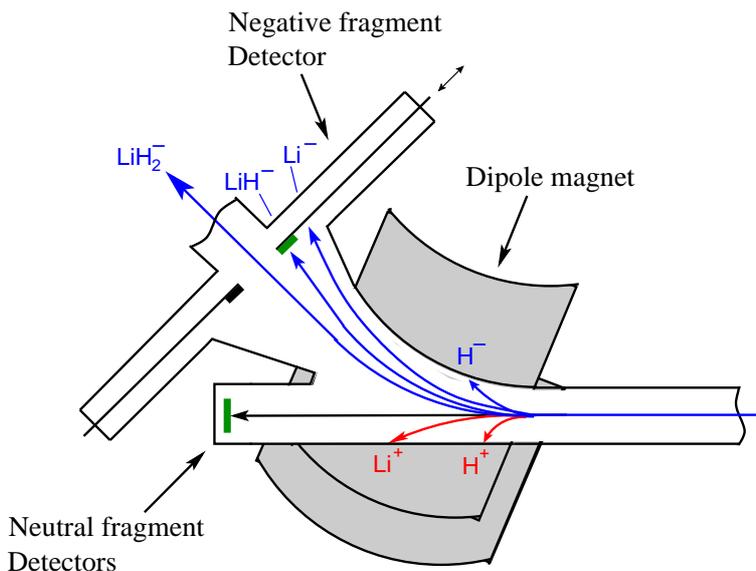
Fig. 5.2: *Sketch of the detector region at the TSR. Trajectories of negative (blue), neutral (black) and positive (red) species are plotted. The negative fragment detector can be moved to be sensitive to either LiH$^-$ or Li$^-$ ions.*

beam as well as the mutual alignment of ion and electron beam is done employing a high ion current of several μA to get a clear signal from the various diagnostic devices which monitor position and energy of the ion beam. As such strong beams are in general difficult to produce for molecular ions, a customary workaround is the use of a so-called *pilot* beam of atomic ions of the same charge to mass ratio as the desired molecules. Atomic beams can be produced at high currents and thus the settings of the storage ring can be optimised using this beam. After this, the molecular ions are injected into the such prepared storage ring.

In case of the present experiment on LiH$_2^-$, no atomic ion beam of the same charge to mass ratio was available. Therefore, a beam of Li$^-$ was used as a pilot beam. The momentum of this beam was set as close as possible to the momentum of the planned LiH$_2^-$ beam by selecting the number of 7-gap RF cavities used during the acceleration (cf. Sec. 3.3.1). Thus the magnetic steering and focusing fields had basically the same effect on both the pilot beam and the molecular beam, and only the few electrostatic steering elements had to be changed when moving to the molecular beam after optimising all settings with the pilot beam.

With this procedure, it was possible to store the LiH$_2^-$ beam and to achieve some phase space cooling by the overlapped electron beam. However, because of the exceptionally low ion current in the order of few nA, it was not possible to monitor or optimise the beam quality in terms of energy spread or spatial extension. Therefore it has to be expected that the alignment of the molecular ion momenta inside the electron cooler is less well-defined than it was found e.g. in the case of H$_3^+$. Hence it should be kept in mind that the flight paths of fragments stemming from electron-induced dissociation reactions and the resulting impact positions of the c.m. at the detector setup might show a broader distribution in the present experiment.
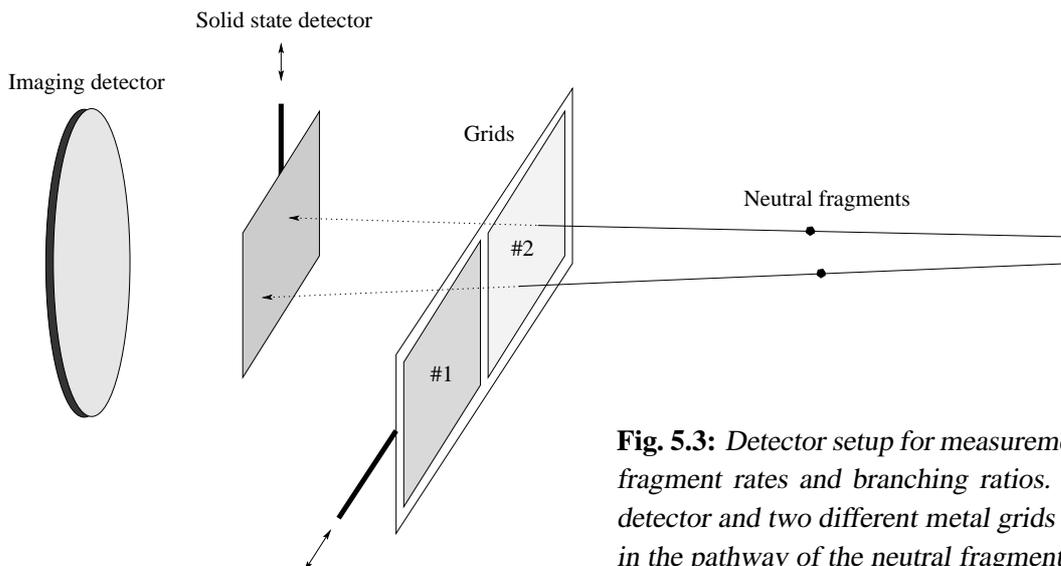
Fig. 5.3: *Detector setup for measurements of neutral fragment rates and branching ratios. A solid state detector and two different metal grids can be moved in the pathway of the neutral fragments.*

In addition to the neutral fragment detectors, an additional *negative fragment detector* was used here, which is located inside the storage ring after the first dipole magnet downstream from the electron cooler (see Fig. 5.2). At this position fragments emerging from the electron cooler region with negative charge and lower mass than the stored ions could be detected. The movable detector could be adjusted to be sensitive to Li^- or LiH^- fragments, while the detection of H^- fragments was not possible due to their strong deflection in the magnetic field. Similarly, no positive fragments could be recorded, as the currently available setup includes no detectors for reaction products of opposite charge compared to the stored beam. The anion detector used here is a combination of scintillator crystal, light guide and photo-multiplier and is described in detail in [82].

For the determination of branching ratios (cf. Sec. 3.3.3), two different grids were implemented in the neutral detector setup which can be moved directly in front of the solid state detector, as shown in Fig. 5.3. The correct position of the desired grid and of the solid state detector with respect to the pathway of neutral fragments coming from the electron cooler region can be confirmed by observing the 'shadow' of these devices on the imaging detector.

Important parameters of the grids used are summarised in Tab. 5.2. A small size and distance of the holes was chosen for both grids to ensure a reliable separation of fragments also at small mutual distances. In the present experiment, a spatial fragment separation in the order of the grid hole size would correspond to a kinetic energy release of only $\sim 100\,\mu$eV. Thus, for any realistic fragmentation reaction the fragments will be spread over a region of the grid large enough to ensure an independent stopping probability for each fragment.

The thickness of both grids was chosen large enough to completely stop any fragment hitting the grid structure. The most critical point here is the stopping of the 3.5 MeV lithium

Grid no.	#1	#2
Nominal transmission	0.7	0.23
Measured transmission	0.641(6)	0.274(6)
Material	nickel	stainless steel
Thickness	5 μm	51 μm
Hole diameter	64 μm	76 μm
Hole distance	12 μm	76 μm

Tab. 5.2: *Relevant parameters of the two grids used for the determination of branching ratios*

atoms. However, with a maximum range of 3.5 μm in nickel [56], these are safely stopped also by the thinner grid. The transmission factors for both grids were determined by measuring over several hours the count rate of alpha particles emitted from a standard americium alpha source, and comparing the results obtained with the solid state detector alone to the results with one of the grids in front of the detector.

Operation of the electron cooler

In contrast to the DR experiments presented in Chap. 4, where electron and ion beams at matched velocities were used only, the reactions to be studied here require significant relative energies of the electrons. To provide these energetic electrons, and at the same time maintain the phase space cooling which is provided by a velocity-matched electron beam (cf. Sec. 3.3.1), the following timing scheme was applied regarding the relative electron energies (also called *wobbling* of the electron cooler).

During the first 2 sec after injection of the ion beam into the storage ring (the so-called *precooling phase*), the electron beam is kept at the same velocity as the ion beam to achieve phase space cooling. After this, the acceleration voltage of the electrons is switched in a fast, repeating cycle between three different values, corresponding to three different relative energies of the electrons in the c.m. frame of the ions.

Regarding this relative electron energy, two terms have to be differentiated: First, the *detuning energy* E_d, which is defined as the kinetic energy which corresponds to the average of the electron velocities $\vec{v}$ in the c.m. frame of the ions

$$E_\mathrm{d} = \frac{1}{2} m_\mathrm{e} \langle \vec{v} \rangle^2 \ . \tag{5.1}$$

The averaging is performed according to the thermal distribution of electron velocities. The case of matched velocities is defined by $\langle \vec{v} \rangle = 0$ and thus $E_\mathrm{d} = 0$. On the other hand, the *average electron energy* in the ion c.m. frame is given by

$$\langle E \rangle = \frac{1}{2} m_\mathrm{e} \langle \vec{v}^{\,2} \rangle \ , \tag{5.2}$$

which is different from zero even in the case of matched velocities. However, the average electron energy in this situation is very close to zero, given by the electron temperature of $kT \approx 10 \, meV$. In the following, the detuning energy is used to describe the setting of the electron cooler, keeping in mind that the actual energies for single electrons can slightly differ from that value.

In the *measurement step* of each wobbling cycle, the detuning energy is set for 25 msec to the value E_e at which a study of fragmentation reactions is desired. During this step, the relevant absolute and channel-resolved fragmentation rates are measured. The energy E_e applied during the measurement steps is usually changed for each new injection of ions into the ring, resulting in the accumulation of a complete energy spectrum of the measured quantities.

During the *reference step* following each measurement step, a fixed detuning energy E_r is applied over 25 msec. The main purpose of this step in the present experiment is to provide a signal which is proportional to the number of ions stored in the ring. At the very small beam currents used during measurements with molecular ions to prevent saturation effects or even damage in the detector system, the standard devices for monitoring the beam current in general are not sensitive. Thus, the neutral fragment count rate at a fixed electron energy is used as a reference signal. However, this yields only a relative measurement of the ion beam current. An absolute calibration would require the determination of the constant factor between this signal and the beam current, which was not possible in the present experiment. The reference energy for all measurements considered in this chapter was set to the arbitrarily chosen value of $E_\mathrm{r} = 41.3 \, \mathrm{eV}$.

Finally, a *cooling step* is applied with electron and ion beam again at matched velocities. This step ensures that the good definition of orbit and energy of the ion beam is maintained, and corrects for any disturbing influence of the electrons at the two other steps, especially when applying electrons at low, but non-zero relative energy in the measurement step. As will be seen, in the case of negative ions the fragmentation rate measured during this step can additionally be used for an estimation of the background rate due to residual gas induced fragmentation reactions.

These three steps are repeated continuously, with a time span of 25 msec each, up to a maximum storage time of 15 sec in the present experiment.

5.3   Experimental results

Using the neutral and negative fragment detectors available at the TSR, the production of both types of fragments in collisions of LiH_2^- ions with electrons was investigated under various experimental conditions. At the negative fragment detector, a signal was found only in the very

first milliseconds after injection of the molecules into the storage ring. In particular, a rate of several kHz was measured that could be attributed to the impact of Li$^-$ ions. These short-time phenomena will be described in Sec. 5.3.3.

At longer storage times, ranging from some msec up to several seconds, only neutral fragments were observed. Typical count rates again were in the order of few kHz. The detailed investigation of this production of neutral fragments will be described in the following.

5.3.1 Total cross section for production of neutral fragments

As discussed in Sec. 2.3.2, the reaction of a molecular anion on the impact of an electron should strongly depend on the relative energy of this electron. Below a threshold energy somewhat higher than the VIP (in the present case 3 eV), no effect of the electron impact is expected. At higher energies, detachment and excitation processes become possible which can produce neutral fragments.

An inspection of the energy dependence of the total cross section for production of neutral fragments by electron impact thus yields first informations on the processes involved: The opening of each new reaction pathway should manifest itself in an increase of this cross section, while the observation of resonant structures would indicate a temporary capture of the free electron, that is, the formation of a dianion [58].

The count rate of neutral fragments as measured by the solid state detector of course not only depends on the probability of each molecular ion to undergo a dissociation into neutral fragments, but also on the number of ions available in the storage ring. This number can exhibit considerable variations from injection to injection and thus for the measurement at different E_e. As a first step in the derivation of the desired cross section, the neutral fragment rate thus has to be normalised to the ion current. As seen above, a measurement of the ion current on an absolute scale is not available; the normalisation is therefore done by calculating the ratio r of the neutral fragment count rate R_{meas} at the *measurement* steps of the electron cooler cycle (that is, with the electron energy set to E_e) and the corresponding rate R_{ref} at the *reference* steps (electron energy $E_r = 41.3$ eV):

$$r(E_e) = \frac{R_{meas}(E_e)}{R_{ref}} \, . \tag{5.3}$$

This ratio describes the *yield* of neutral fragments per molecular ion. Its natural dimension would be sec^{-1}, but here it is expressed in units of the yield $r(E_r)$ at reference energy. The experimentally measured energy spectrum $r(E_e)$ of this neutral fragment yield is shown in Fig. 5.4 for moderate electron energies E_e.

As visible in the Figure, a certain neutral fragment yield is observed already for $E_e = 0$, staying constant up to an electron energy of ~ 5 eV. This constant level suggests that electrons
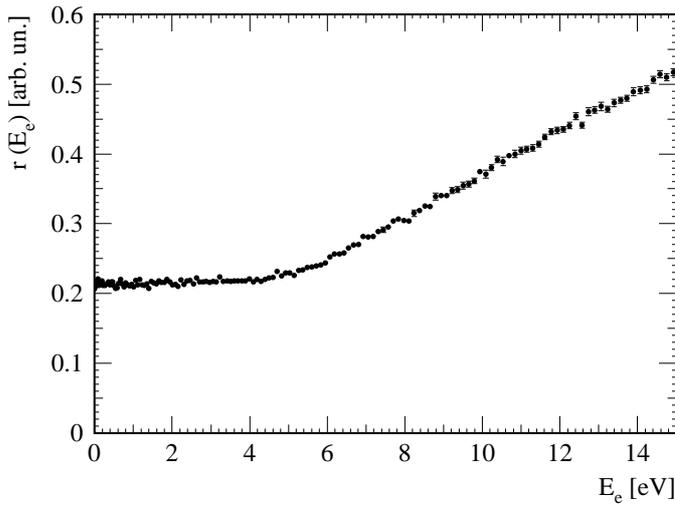
Fig. 5.4: *Total yield r of neutral fragments per molecular ion, as a function of the electron energy E_e. The absolute scale of r was arbitrarily chosen to fulfil $r(E_r) = 1$.*

at low energy, as expected, do not contribute to the dissociation of LiH_2^- molecules into neutral fragments. The yield observed at these low E_e can be attributed to collisions of the molecular ions with residual gas molecules still present in the ultrahigh vacuum of the storage ring. At the MeV beam energies considered here, such collisions can easily remove an electron from the anion leading to the production of one or more neutral products.

In the measurement shown in Fig. 5.4, the contribution of residual gas background amounted to 22% of the yield at the reference energy E_r. To account for variations in the residual gas pressure, this background contribution can be continuously monitored during the measurement using the rate R_{cool} recorded during the *cooling* step of the electron cooler cycle.

To further analyse the effect of electron impact on the anion, the background rate $r(0\,eV)$ is now subtracted from the total rate $r(E_e)$. The resulting electron induced rate can then be normalised to the electron density n_e (in cm^{-3}), yielding the rate coefficient α (in cm^3/sec) for the production of neutral fragments by electron impact:

$$\alpha(E_e) = \frac{r(E_e) - r(0\,eV)}{n_e} \tag{5.4}$$

This quantity is connected to the cross section σ through the relation

$$\alpha(E_e) = \langle \sigma v \rangle_{E_e} \tag{5.5}$$

with the averaging according to the distribution of relative electron velocities v at the given detuning energy E_e. At the detuning energies of several eV considered here, the effect of the electron temperature is small, and the cross section σ can be approximated by the average cross section σ_{av}:

$$\sigma_{av}(E_e) = \frac{\langle \sigma v \rangle_{E_e}}{\langle v \rangle_{E_e}} = \frac{\alpha(E_e)}{\langle v \rangle_{E_e}} \propto \frac{\alpha(E_e)}{\sqrt{E_e}} \ . \tag{5.6}$$
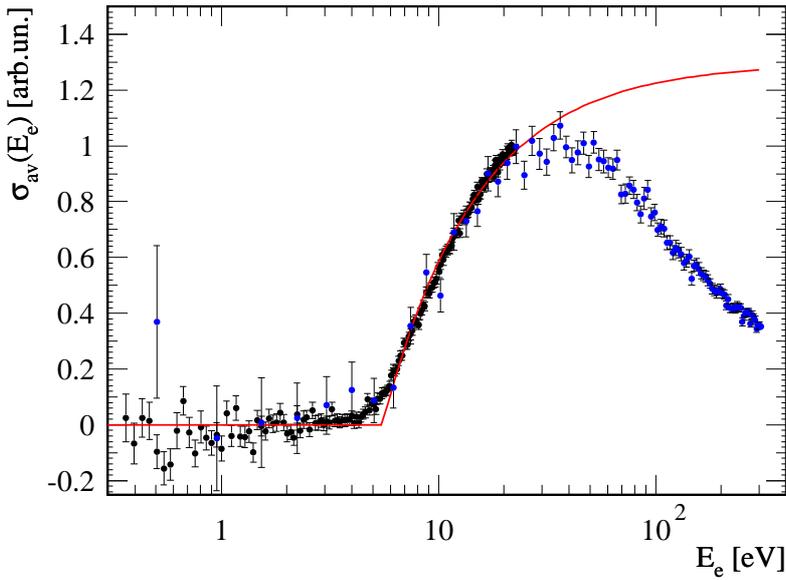
Fig. 5.5: *Average cross section σ_{av} for the production of neutral fragments by electron impact as a function of the electron energy E_e. Circles: Experimental data (two independent sets of data are shown in black and blue), Red line: Fit to a classical reaction model, Eq. (5.7).*

The measured shape of $\sigma_{\mathrm{av}}(E_e)$ is shown in Fig. 5.5. Again an arbitrary normalisation ($\alpha(E_r) = 1$) was chosen, as the absolute cross section could not be determined. From the threshold at $E_e \approx 5\,\mathrm{eV}$, the cross section rises without further structure up to a maximum at $E_e \approx 40\,\mathrm{eV}$, and then decreases towards higher electron energies.

The behaviour near the threshold energy is compared to a classical reaction model [78] developed for the description of the electron-impact detachment of electrons from atomic anions. This model assumes a constant probability p for a detachment reaction, given that the electron gets closer to the anion than a reaction radius R, which (in atomic units) corresponds to a threshold energy $E_{\mathrm{th}} = 1/R$. The model thus predicts a cross section of

$$\sigma(E) = \begin{cases} p\pi R^2 \left(1 - \frac{E_{\mathrm{th}}}{E}\right) & (E > E_{\mathrm{th}}) \\ 0 & (E \leq E_{\mathrm{th}}) \end{cases} . \tag{5.7}$$

The red line in Fig. 5.5 represents a fit of this model to the experimental data in the region $E_e = 0 - 20\,\mathrm{eV}$, using the threshold energy E_{th} and an overall normalisation factor as fit parameters. Despite the fact that this model is strongly simplifying the situation in a polyatomic molecule, the quality of the fit is comparable with that obtained for atomic [78] and diatomic [58] anions and a reasonable threshold energy of $E_{\mathrm{th}} = 5.5\,\mathrm{eV}$ is found.

For the deviation between the experimental data and the fitted curve in the threshold region, several reasons are possible:

- The observed structure could result from quantum phenomena like tunnelling, which are not covered by the classical reaction model.

- Because of the extended geometrical structure of the LiH_2^- molecule with the negative charge mainly located at the terminal H atoms [65], the cross section near the threshold can be expected to depend on the orientation of the molecule with respect to the incoming electron, an effect which would smear out any sharp structures in the cross section in a measurement employing an unpolarised ion beam.

- Another perturbing effect could be changes in the geometry due to vibrational motion, which was suspected to play a role already for diatomic anions [58]. In the case of LiH_2^- a radiative decay of vibrational excitations is possible via electrical dipole transitions, allowing a fast thermalisation to the surrounding temperature of 300 K. However, the different nuclear conformations possible in the remaining lowest vibrational states could possibly still cause a smearing of the threshold energy for electron detachment.

- An experimental effect which is likely to produce artificially structures like the one observed here is the so-called *toroid contribution* to the cross section. In the two regions of the electron cooler, where the electron beam and the ion beam are merged and separated by a bending of the electron beam in a magnetic toroid field, the electrons possess an increased energy in the c.m. frame of the ions due to the angle between the two beams. This leads to a contamination of the signal measured at low E_e by fragmentation events stemming from higher energetic collisions in the toroid regions, which can cause a smearing of sharp structures in the cross section and thus explain the observed behaviour.

- Finally, the observed structure could have its origin in the contribution of different potential energy surfaces to the dissociation process. As shown in Sec. 5.1.2, the removal of a valence electron from LiH_2^- can lead to two different electronic states of the LiH_2 system with an energy difference of only 0.35 eV.

Facing the various effects listed here, the threshold energies for these two possible detachment processes cannot be resolved by the present cross section measurement. Thus, both processes have to be considered possible pathways in the observed detachment reaction. However, further steps or resonances in the cross section are not observed. This suggests that higher PES do not contribute significantly to the observed fragmentation reaction, and that no intermediate dianion are formed.

The deviation of reaction model and experimental data at high energies is expected, as here the assumption of constant reaction probability p is no longer valid.

5.3.2 Branching ratios between different channels

The total mass of neutral fragments

After the investigation of the *total* cross section for reactions producing any neutral fragments, the next step in the characterisation of the processes involved now is a closer study of the *types* of fragments emerging from the breakup.

The absence of any charged fragments at the negative fragment detector for storage times longer than some msec, as well as the observed dependence of the cross section for production of neutral fragments on the electron energy suggest that the main reaction mechanism is the detachment of an electron from one of the two valence orbitals, followed by a dissociation into neutral fragments. Thus, the complete mass of the LiH$_2^-$ molecule summing up to 9 a.m.u.[3] is expected to reach the neutral fragment detector for each fragmentation event. However, an experimental verification of this expectation is advisable. As will be seen below, some disturbing effects are thinkable which can reduce the number of fragments that reach the detector. Considering the atomic composition of the LiH$_2^-$ molecule, an observation of neutral fragment events with a total mass of 1, 2, 7 or 8 thus in principle also appears possible.

As described in Sec. 3.3.3, the solid state detector used in the measurement of neutral fragment rates is capable of determining also the total mass of neutral fragments for each recorded event. Already in the exemplary spectrum of Fig. 3.5, a clear dominance of mass 9 was observed, confirming the above expectation, but a certain contribution was found also for lower masses. In Fig. 5.6, the fraction of each of these masses in the total neutral event rate is now followed as a function of the electron energy E_e. The strong dominance of mass 9 is obvious over the whole energy range investigated, reaching values up to $P_m \approx 0.9$ for high electron energies. Thus, for a large majority of breakup events all emerging fragments are neutral. This observation provides further evidence that detachment, as opposed to dissociative excitation, is governing the electron-induced fragmentation of LiH$_2^-$.

The energy dependence of the mass fractions P_m can be approximatively described by two plateau-like structures for $E_e \lesssim 5$ eV and $E_e \gtrsim 20$ eV, respectively. The transition between these plateaus is correlated to the change in the total yield of neutral fragments as observed in Fig. 5.4 and can be interpreted as a transition from pure residual gas background at $E_e < 5$ eV to a predominantly electron induced signal at higher energies. The increased $m = 9$ fraction for the electron dominated signal could reflect different breakup processes for electron and residual gas collisions. On the other hand, before drawing this conclusion, a number of phenomena have to be considered, which can reduce the mass observed at the neutral fragment detector.

First, the design of the solid state detector available at the neutral fragment chamber causes

---

3   All masses here and in the following are given in atomic mass units (a.m.u.).
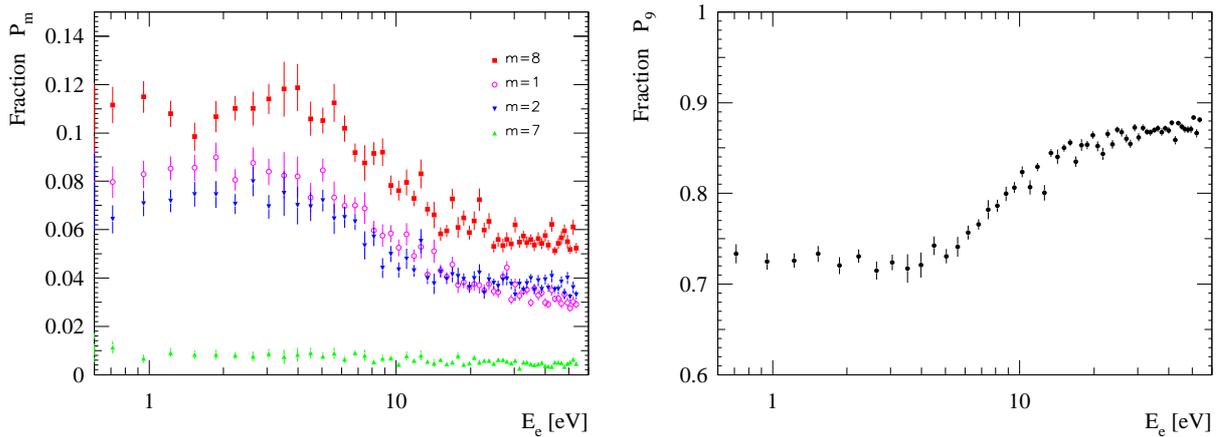
Fig. 5.6: *Fraction P_m of the observed neutral events, for which a total mass of $m = 1, 2, 7, 8$ a.m.u. (left) and $m = 9$ a.m.u. (right) was detected, as a function of the electron energy E_e.*

a slightly reduced efficiency, as described in Sec. 3.3.3. In the present study, this results in a certain probability for each fragment of mass 1 or 2 to be neglected by the detector. In the same way, fragments of mass 7, 8 and 9 can be mistaken for mass 1, if they hit an area of reduced sensitivity. The probability for such a false detection is difficult to determine, as it depends on the exact impact position of a fragment, which in turn can be correlated to several other experimental parameters. From experiments on other molecules, however, this probability can be estimated to be in the order of $\sim 1\%$.

Second, neutral fragments produced in a dissociation reaction might geometrically miss the detector. This in turn can have several reasons:

- A high kinetic energy release of the fragmentation reaction might result in a large separation of the fragments which exceeds the size of the active area of the detector.

- The fragmenting molecule cold possess an initial momentum vector that is not pointing exactly at the neutral fragment detector. Because of the limited beam quality achieved in the present experiment (see Sec. 5.2) the observation of dissociation events stemming from such molecules cannot be excluded.

- In addition, a considerable amount of misaligned dissociation events has to be expected from residual gas collisions. These are possible not only inside the interaction region in the electron cooler, but in principle along the whole ion beam orbit. In the sections of the storage ring which are adjacent to the electron cooler, the ion beam is aligned similar, but not exactly in the same way as inside the interaction region. Therefore, fragmentation events originating from these sections have a high probability for depositing some, but not all of the neutral fragments at the designated detector.

Finally, the physical process under study might indeed produce also charged fragments, which are deflected by the TSR dipole magnet before reaching the neutral fragment detector, as sketched in Fig. 5.2. The production of Li^- and LiH^- fragments can be excluded, as the negative fragment detector was sensitive to these species and no contribution was found at the long storage times considered here. Other types of charged fragments (that is, H^- ions or any cations) could not be studied in the experimental setup available.

In summary, the total mass of neutral fragments observed for a dissociation event can be reduced by several experimental effects. Therefore, the observed mass fractions are still consistent with the assumption that electron impact on LiH_2^- does not produce any charged fragments. On the other hand, a certain contribution of processes which do produce charged fragments cannot be excluded. However, as none of the experimental effects listed above is capable of *increasing* the detected mass of neutral fragments, an upper limit of $\approx 10\%$ can be given for the contribution of such processes.

The observed energy dependence of the neutral mass fractions can be interpreted as a transition from residual gas background to an electron dominated signal. No evidence for an energy dependence of the electron induced fragmentation reaction itself is found.

After discussion of the total mass of all neutral fragments, the next question to be addressed now is the atomic composition of these fragments, which will reveal the contribution of different exit channels in the electron-induced fragmentation of LiH_2^-.

Atomic composition of the neutral fragments

In Sec. 3.3.3, the grid method for the determination of branching ratios in the fragmentation of molecules was introduced. This method is mainly used in the DR of molecular cations [77] and in fragmentation reactions of diatomic anions [58]. In all these cases, the number of channels which have to be considered as possible outcome of the fragmentation reaction is limited to 3–4. The desired branching ratios can then be calculated from the measured data in a straightforward manner.

In the present experiment, as seen above, a number of experimental effects can reduce the number of fragments observed at the detector and thus induce the detection of *artificial* channels which are not produced by the breakup reaction studied. On the other hand, the limited *a priori* knowledge on the fragmentation process does not allow a reliable prediction of possible *physical* channels.

Thus, all combinatorially possible configurations of free atoms and bound molecules, consisting of up to one Li and two H atoms have to be considered as possible channels that might

contribute to the rate observed by the neutral fragment detector. These are in total ten channels:

$$
\begin{array}{llllll}
\mathrm{LiH_2} & (\alpha_1) & \mathrm{LiH} & (\alpha_5) & \mathrm{H_2} & (\alpha_8) \\
\mathrm{LiH + H} & (\alpha_2) & \mathrm{Li + H} & (\alpha_6) & \mathrm{H + H} & (\alpha_9) \\
\mathrm{Li + H_2} & (\alpha_3) & \mathrm{Li} & (\alpha_7) & \mathrm{H} & (\alpha_{10}) \\
\mathrm{Li + H + H} & (\alpha_4) & & & &
\end{array}
\tag{5.8}
$$
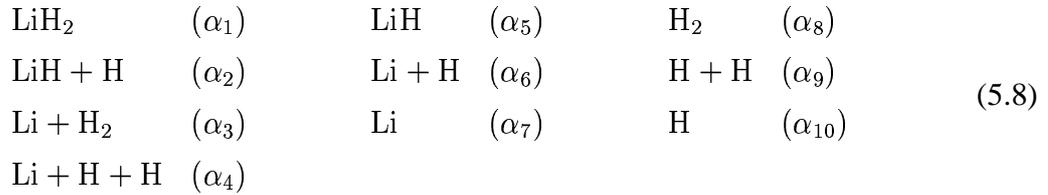
with the coefficients α_i denoting the branching fraction of each channel ($i = 1..10$), that is, its relative contribution to the rate of neutral fragments. The goal of the grid method is now to determine each of these branching factors α_i. This is done here by comparison of the neutral mass fractions $\{P_m\}$ measured under application of several different grids. In this case, special care has to be taken to achieve a consistent normalisation of the $\{P_m\}$ for all grids. The algorithm used for this reconstruction is described in App. B. In short, the data available turn out to provide insufficient independent information to enable an algebraic solution of the involved system of equations, even when combining the measurements with several grids. The reconstruction algorithm thus additionally makes use of the fact that all α_i have to be non-negative. That way it is able to derive upper and lower limits for all branching factors.

The measurement of the energy-dependent mass fractions shown in Fig. 5.6 was thus repeated for each of the two grids, that were moved in front of the solid state detector. The branching factors α_i obtained by the reconstruction algorithm from these data are shown in Fig. 5.7 in the energy range $E_\mathrm{e} = 0\text{--}60\,\mathrm{eV}$.

The by far dominating channel in the background- as well as the electron-dominated energy range is the breakup into $\mathrm{LiH + H}$ with a fraction around 75% at high energies. The contributions of all other channels are of the order of few percent and in most cases even consistent with zero. The energy dependence of the α_i, where visible at all, can again be interpreted as result of the transition from pure background to predominantly electron induced breakup reactions. For example, the decrease observed in α_5 (LiH) and α_{10} (H) when going to higher electron energies can be explained by the assumption that these channels are observed due to an incomplete detection of a fragmentation into the $\mathrm{LiH + H}$ channel, which is more likely in the background-dominated energy region. The energy dependence of the observed branching factors thus again is in agreement with the assumption that the relative contribution of fragmentation channels to the *electron-induced* dissociation reaction does not depend on the electron energy.

To get a more quantitative picture, the same reconstruction was done using the mass fraction data collected during the *cooling* and *reference* steps of the electron cooler cycle, that is at two fixed electron energies of $E_\mathrm{e}{=}0$ and 41.3 eV. Because of the large number of events recorded at these energies, statistical errors are much smaller here. In addition, a tentative background correction can be performed. The observed α_i values can be expressed as a composition of
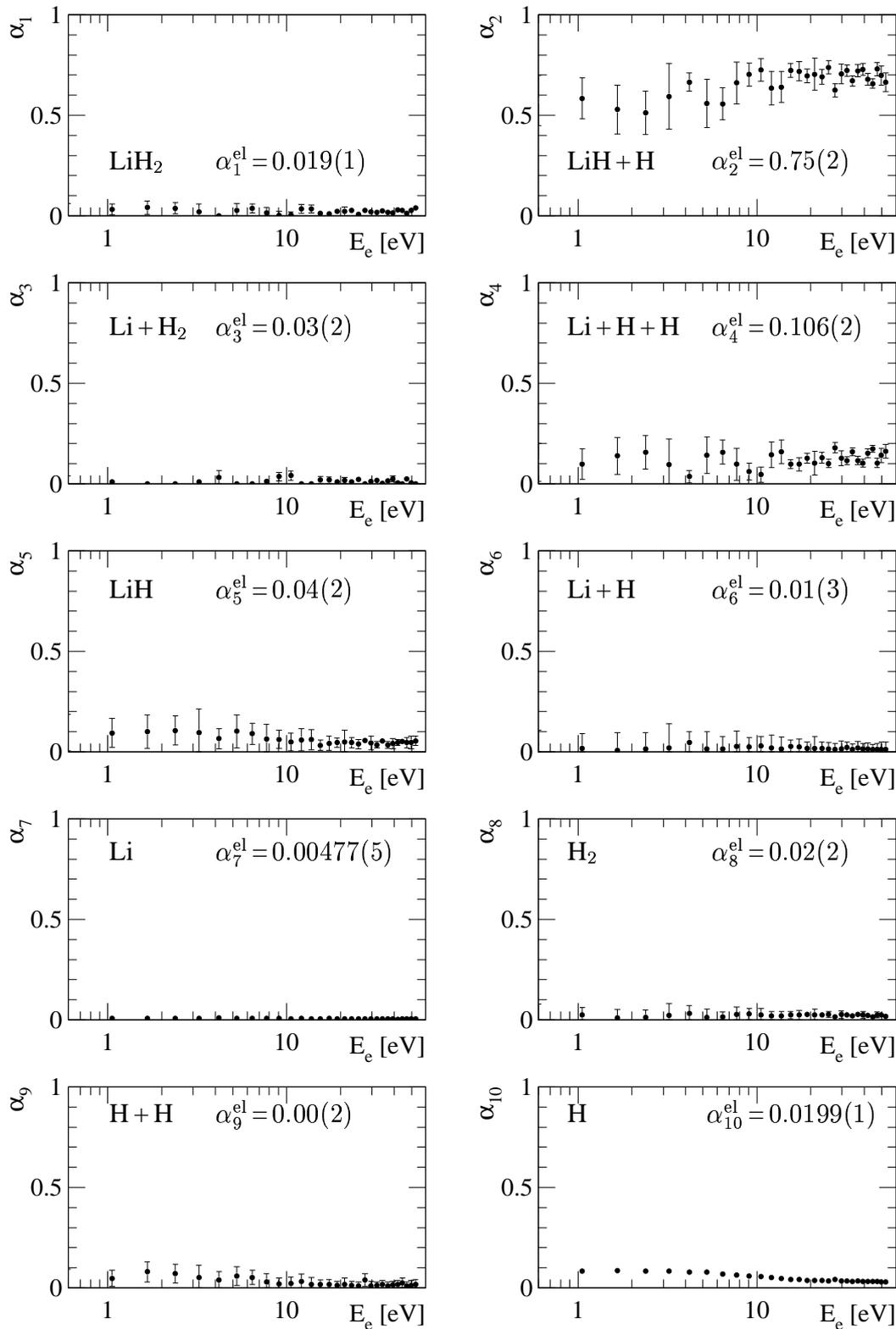
Fig. 5.7: *Branching factors α_i obtained using the grid method as a function of the electron energy E_e. The error bars given include statistical errors as well as the systematic uncertainty of the reconstruction process. The α_i^{el} values cited describe the branching factors for electron-induced processes only, as obtained from Eq. (5.11). See text for a discussion of additional sources of errors.*

contributions from residual gas background (bgr) and electron induced processes (el) as follows:

$$\alpha_i \;=\; \frac{R_{\mathrm{el}}\,\alpha_i^{\mathrm{el}} + R_{\mathrm{bgr}}\,\alpha_i^{\mathrm{bgr}}}{R_{\mathrm{el}} + R_{\mathrm{bgr}}} \tag{5.9}$$

Assuming now that at cooling energy only background induced fragmentation is observed ($R_{\mathrm{cool}} = R_{\mathrm{bgr}}$ and $\alpha_i^{(\mathrm{cool})} = \alpha_i^{\mathrm{bgr}}$), and that the signal at reference energy is composed of background plus electron induced processes ($R_{\mathrm{ref}} = R_{\mathrm{bgr}} + R_{\mathrm{el}}$), we obtain for the branching factors measured at reference energy

$$\alpha_i^{(\mathrm{ref})} \;=\; \frac{\left(R_{\mathrm{ref}} - R_{\mathrm{cool}}\right)\alpha_i^{\mathrm{el}} + R_{\mathrm{cool}}\,\alpha_i^{(\mathrm{cool})}}{R_{\mathrm{ref}}} \;, \tag{5.10}$$

and thus for the electron induced process

$$\alpha_i^{\mathrm{el}} \;=\; \left(\alpha_i^{(\mathrm{ref})} - \frac{R_{\mathrm{cool}}}{R_{\mathrm{ref}}}\alpha_i^{(\mathrm{cool})}\right) \Big/ \left(1 - \frac{R_{\mathrm{cool}}}{R_{\mathrm{ref}}}\right) \;. \tag{5.11}$$

The total contribution of background events $\frac{R_{\mathrm{cool}}}{R_{\mathrm{ref}}}$ can be obtained only from a measurement without grid. Assuming this value of 22% (see Sec. 5.3.1) to be valid in all measurements, an approximative background subtraction is possible using Eq. (5.11).

The background corrected branching factors α_i^{el} found using this method are also given in Fig. 5.7. Despite the small statistical and reconstruction errors for some of the channels, several other sources of errors have to be taken into account. Besides the already noted sensitivity properties of the solid state detector, these are mainly the uncertainty in the measurement of the transmission factors of the two grids, and in particular the transferability of these measurements employing alpha particles to the present experiment. As noted in Sec. 3.3.3, small variations of the transmission factor dependent on the type of projectiles might be possible, which could result in errors in the order of few percent in the reconstruction of branching factors.

For the interpretation of the results obtained here regarding the physical breakup process, an additional uncertainty that has to be taken into account are the various effects which can reduce the number of fragments detected for a fragmentation reaction, as discussed already for the interpretation of the total neutral mass spectra.

In spite of these uncertainties, the present experiment allows the derivation of approximative branching factors for the electron induced fragmentation of LiH_2^-. In particular, an important result is the clear dominance of the $\mathrm{LiH} + \mathrm{H}$ channel which rejects the theoretical prediction. All other channels, both for the production of only neutral and charged fragments, are consistent with zero within the uncertainties of the experiment, albeit small contributions from these channels cannot be excluded completely.

As already noted, direct evidence for the production of charged fragments was found only at very short storage times. These observations will be discussed in the following section.
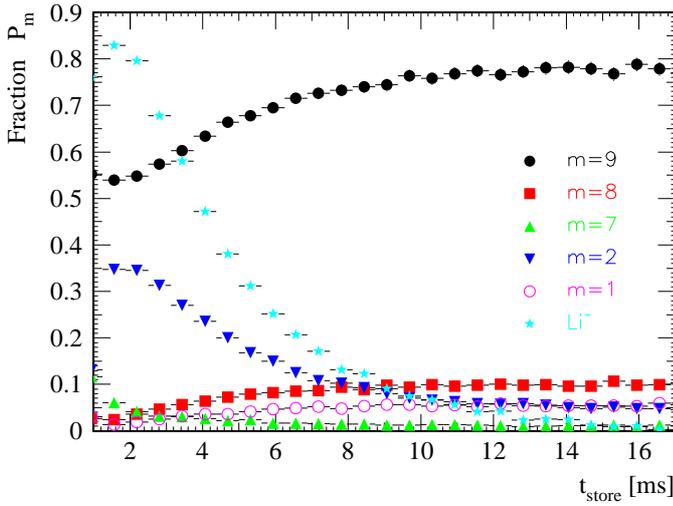
Fig. 5.8: *Fraction P_m of events with a total mass $m = 1$, 2, 7, 8, 9 of detected neutral fragments and contribution P_{Li^-} of Li^- ions (relative to the total neutral event rate) as a function of the storage time t_{store}. The electron energy E_e was fixed to 41.3 eV.*

5.3.3   Observations at short storage times

In the fist milliseconds after injection of the molecular ions into the storage ring, the impact of Li^- ions was observed at the negative fragment detector. To further investigate these special fragmentation events after very short storage times, a series of specific experiments was performed, where data from both the neutral and the negative fragment detectors were recorded with a microsecond time resolution.

As the phase space cooling of the ion beam (see Sec. 4.2) is finished only after several seconds, experiments during the first milliseconds of storage have to be performed with an translationally hot ion beam. Besides a higher relative energy between the colliding ions and electrons, this also causes a larger spread of the momentum vectors of the molecular ions, leading to a higher probability of geometrical particle losses, that is, the recording of events where one or more fragments miss the neutral fragment detector even though they are neutral. The accuracy of a measurement of branching factors will thus be even lower here than for the experiments at longer storage times described so far, especially for the $m < 9$ channels. Nevertheless, it is interesting to observe qualitatively the behaviour at short storage times.

At the very short time scales to be considered here, the usual *wobbling* scheme regarding the electron energies (see Sec. 5.2), which works on a time scale of several tens of milliseconds, could not be applied. Instead, two separate measurements were performed, keeping the electron cooler at a constant detuning energy of 0 eV and 41.3 eV, respectively.

Neutral mass fractions

The fractional contribution of events with different total masses of neutral fragments, observed for $E_e = 41.3$ eV, are shown in Fig. 5.8. In addition to the neutral mass fractions P_m, the count

rate at the negative ion detector is plotted, normalised also to the sum of all events involving neutral fractions. From the position of the anion detector, the negative fragments could clearly be identified as mass 7, that is Li^- ions. At the position corresponding to mass 8 (LiH^-), no ions were detected at any storage time.

The negative ion rate P_{Li^-}, even though normalised to the total neutral rate, can only tentatively be compared to the neutral mass fractions P_m regarding the absolute scale, as the two detectors in use can have different detection efficiencies, and no coincidence condition was set. While the surface barrier detector used for neutral fragment detection is assumed to have a 100% detection efficiency, a lower value has to be expected for the anion detector, due to technical problems found in the operation of this new detection system [82]. On the other hand, Li^- ions react to some extend on the magnetic steering and focusing elements of the storage ring. Therefore, the probability to collect fragments of dissociation reactions that took place outside the electron cooler is much higher for the anion detector than for the neutral fragment detector, thus increasing the anion count rate. Despite this uncertainties in the absolute count rate, the temporal evolution of the Li^- signal can still be analysed and gives a valuable addition to the neutral fragment data.

After $\sim 12\,\text{msec}$ of storage, the fractions observed in Fig. 5.8 approach constant values. No further changes were found for storage times up to $80\,\text{msec}$. Taking into account the increased probability of geometrical losses, these asymptotic values are comparable to the distribution at long storage times (Fig. 5.6). In the first few msec after injection, however, the neutral mass fractions significantly differ from this distribution, showing now a strong contribution of $m = 2$ and a considerable increase of the very small $m = 7$ signal. At the same time, a high count rate of Li^- fragments is observed.

For the very first 1–$2\,\text{msec}$ after injection of the ion beam, no clear interpretation of the recorded data is possible, as here the so-called *injection flash*, consisting of a large number of ions which did not reach stable orbits in the storage ring, is saturating the detectors.

Branching ratios

To clarify which dissociation channels contribute to the observed neutral mass fractions, the grid method was used as described in Sec. 5.3.2 and branching factors α_i were determined as a function of storage time. For better visibility of the count rate variation of each channel, the obtained branching factors α_i are multiplied with the strongly time dependent total neutral rate R, yielding the partial rates $R_i = \alpha_i R$. These partial rates are shown in Fig. 5.9 for the dominant neutral channels, together with the count rate of Li^- ions. Channels with low contribution are not shown, their maximum partial rate is indicated by the dashed lines. Two different electron energies were used, $E_e = 0\,\text{eV}$ and $E_e = 41.3\,\text{eV}$, as indicated in the figure. Error bars are
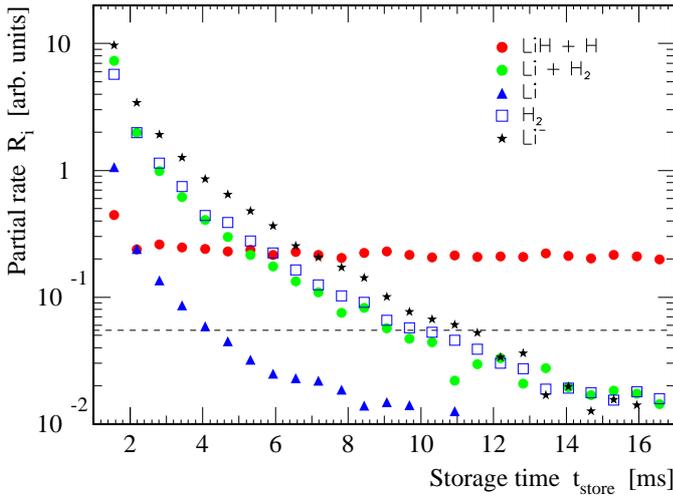
$$E_e = 0 \, \text{eV}$$
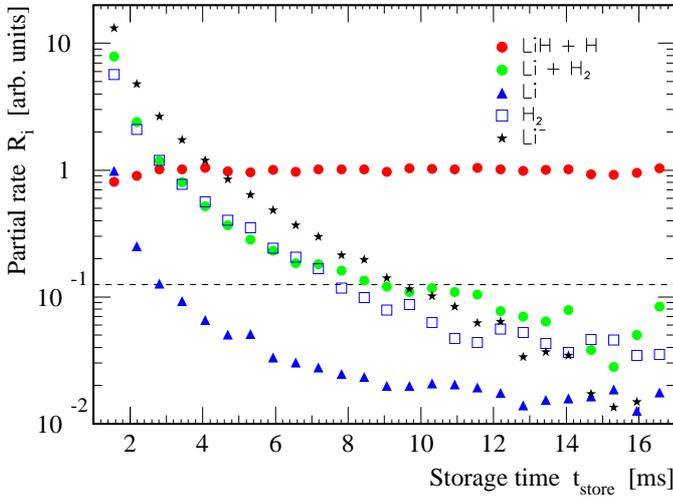
$$E_e = 41.3 \, \text{eV}$$

Fig. 5.9: *Partial rates $R_i = \alpha_i R$ of the dominant neutral breakup channels and Li^- rate as a function of the storage time t_{store}. The electron energy E_e was kept at a fixed value as indicated. Dashed lines symbolise the contribution of neutral channels not shown here.*

omitted here for clarity, the different uncertainties again sum up to errors of several percent.

For both electron energies, the partial rate of the LiH + H channel, which is dominating at long storage times, is basically constant even in the first milliseconds after injection. An additional contribution to the neutral signal at very short storage times comes from the Li + H_2 and H_2 channels. Their count rates are initially up to a factor of 10 higher than for the LiH + H channel, but decrease very rapidly following a roughly exponential decay with a lifetime of 2.8 ± 0.1 msec. The same behaviour is exhibited by the Li^- ion rate, which strongly suggests that the observed H_2 and Li^- fragments originate from the same dissociation channel $LiH_2^- \rightarrow Li^- + H_2$. Remarkably, the same lifetime for the decay of the partial rate was observed not only for H_2 and Li^-, but also for the Li + H_2 channel.

The experiment thus shows a complete change of the dominant dissociation channel in the first milliseconds of storage, which can only be attributed to changes in the internal state distribution of the molecular ion beam. The only external condition that could introduce a storage

time dependence of the branching factors is the phase space cooling of the ion beam. This process, however, acts on the much longer time scale of few seconds and furthermore can only change (by focusing the ion momenta to the neutral fragment detector) the detailed branching factors especially when comparing $m = 9$ to $m < 9$ channels. The observed appearance of an additional $m = 9$ channel at short storage times, in combination with a constant rate at the channel dominating for longer times, cannot be explained by changes in the alignment or focusing of the ion beam. Hence it is obvious that a *transient state* of the LiH_2^- ion is the origin of the observed decay into the $Li^- + H_2$ and $Li + H_2$ channels (called *transient channels* in the following).

Characterisation of the *transient state*

A remarkable property of the two transient channels is the fact that they exhibit the same absolute count rate[4] as well as the same decay time, suggesting that both channels stem from the same transient state of the anion, and that this state can dissociate via both the anionic and the neutral channel with equal probability.

Some more characterisation of the transient state can be deduced from the comparison of the decay time of the count rate in the transient channels to the overall beam lifetime, which was measured to be 1.6 ± 0.1 sec at $E_e = 0$. Thus, the decay rate of the transient state is found to be a factor of 570 ± 40 higher than the rate of residual gas induced dissociation the molecule exhibits at longer storage times, in a condition that will be called the *stable state* in the following for distinction from the short-lived *transient state*.[5]

However, the observed decay of the transient state might occur via two processes, the fragmentation of the molecule or a transition to the stable state. While the total decay rate is given just by the observed 2.8 msec lifetime of the fragmentation signal in the transient channels, an estimation of the relative contribution of the two decay modes requires a more detailed analysis of the fragmentation count rates, as described in App. C.

Based on the experimental data available, it can be concluded that at least 25% of the transient state population decays via fragmentation of the molecule rather than a transition to the stable state. An upper limit cannot be given here, thus also the complete absence of a transition to the stable state would be in agreement with the experimental findings.

From this follows the remarkable observation that the fragmentation of the molecule is at least two orders of magnitude faster for the transient state than for the stable state. For the initial

---

4   Even though the Li^- rate cannot be compared directly to the neutral fragment rates, the agreement of the $Li + H_2$ and H_2 rates allows this observation.

5   The term *state* used here does not stand for a state in the sense of quantum mechanics. The internal properties of a molecule which might determine its possible fragmentation channels and thus its attribution to one of the two states will be discussed later.

population of the transient state, the same estimation yields a fraction in the order of 5–25% of the total ion beam (see App. C).

Effect of electron impact

To estimate the influence of electron interactions on the decay of these transient state ions, it is now interesting to compare the partial rates in the transient channels for the two measurements at $E_e = 0$, where the electrons cannot approach the anion due to the mutual Coulomb repulsion, and at $E_e = 41.3\,\text{eV}$, where a dominance of electron-induced fragmentation reactions was observed for the stable state.

For a direct comparison of the two situations, the dissociation rates per molecular ion would be needed instead of the absolute count rates observed here. However, this would require a determination of the number of ions present in the storage ring during the measurement. As for the experiments at long storage times, this ion current is too low to be accessible for an absolute measurement. In the present case, even a relative calibration for comparison of the two measurements at different E_e is difficult. The dissociation rate at a common reference electron energy E_r, which is usually used as a measure of the ion current, can only be recorded in experiments working at longer time scales, where a *wobbling* of the electron cooler energy during the measurement is possible (see Sec. 5.2). Nevertheless, the behaviour at $E_e = 0$ and $E_e = 41.3\,\text{eV}$ can tentatively be compared assuming that the yield of dissociation events in the LiH + H channel depends on E_e in the same way for the measurements at long and short storage times. In particular, the yield of LiH + H at $E_e = 0$ is assumed to be 22% of the yield at $E_e = 41.3\,\text{eV}$ as found in Sec. 5.3.1. The normalisation of the two data sets shown in Fig. 5.9 is thus chosen such that the partial rate of LiH + H at $E_e = 0$ amounts to 22% of the rate at $E_e = 41.3\,\text{eV}$.

Comparing now the partial rates in the transient channels for the two electron energies, only a relatively small increase of the order of $10 - 20\%$ is found for $E_e = 41.3\,\text{eV}$, indicating a minor, possibly even zero contribution of electron-impact to the fragmentation of the transient state of LiH$_2^-$.

Furthermore, the same lifetime of 2.8 msec is found for the signal from the transient channels, independent of the electron energy. Thus, the total decay rate of the transient state (including also transitions to the stable state) turns out to be unaffected by the presence of high-energetic electrons. Combining these two observations, the transition rate from the transient to the stable state can also be concluded to be only weakly influenced by electron-impact, provided that such a transition exists.

In conclusion, a transient state of the LiH$_2^-$ molecule was found to be present in the first

	Transient state	Stable state
Fragmentation channels	$Li + H_2$ and $Li^- + H_2$	$LiH + H$
Total decay rate Γ ($E_e = 0$)	$360 \pm 15 \, sec^{-1}$	$0.63 \pm 0.04 \, sec^{-1}$
transition rate Γ_{trans} to the stable state	$\lesssim 270 \, sec^{-1}$	—
fragmentation rate Γ_{frag}	$\gtrsim 90 \, sec^{-1}$	$0.63 \pm 0.04 \, sec^{-1}$
Result of electron impact ($E_e = 41.3 \, eV$)	none observed	increase of Γ ($\times 4.5$)
Initial population	~ 5–25%	~ 75–95%

Tab. 5.3: *Observed properties of the transient and stable states of LiH$_2^-$.*

milliseconds after injection of the ions into the storage ring. While the nature of this state, as well as its decay mechanisms are yet unclear, a tentative characterisation can be given based on the experimental data, as summarised in Tab. 5.3.3. A discussion of possible interpretations of this state will be given in Sec. 5.4.

5.4 Comparison to theory

5.4.1 Calculation of potential energy surfaces

To clarify the processes underlying the breakup reactions observed experimentally, preliminary *ab initio* calculations of the potential energies of the neutral and anionic systems were done at selected geometries, in addition to the existing theoretical work (see, e.g. [65, 66, 14]). The calculations have been performed in collaboration with the group of R. Schinke, Max-Planck-Institut für Strömungsforschung, Göttingen, Germany. The quantum chemistry code MOLPRO [51] was employed, running on a cluster of IBM-RS6000 machines located at the GWDG (Gesellschaft für wissenschaftliche Datenverarbeitung mbH Göttingen). Calculations of MRCI[6] type were done with the standard basis set AVTZ for hydrogen, and VTZ+2(SPD) for lithium.

To parametrise the three-dimensional space of nuclear geometries, the coordinates ϕ, r and x are chosen as follows: ϕ describes the H-Li-H bond angle (see Fig. 5.11), while the hyperradius r and the symmetry coordinate x are defined by

$$r = \frac{r_1 + r_2}{2} \qquad \text{and} \qquad x = \frac{r_1 - r_2}{r_1 + r_2}, \qquad (5.12)$$

with the Li-H bond lengths r_1 and r_2. While r denotes the overall *size* of the atomic system, x and ϕ are dimensionless and have the function of hyperangles describing the *shape* of the

---

6 Multiconfiguration Reference internally contracted Configuration Interaction

$C_{\infty v}$ $(\phi = 180°)$

Fig. 5.10: *Calculated potential energy surfaces for the neutral LiH$_2$ (black) and the anionic LiH$_2^-$ system (blue). Energies of the two lowest states are given as a function of x, with ϕ set to 0 and r optimised for each point.*
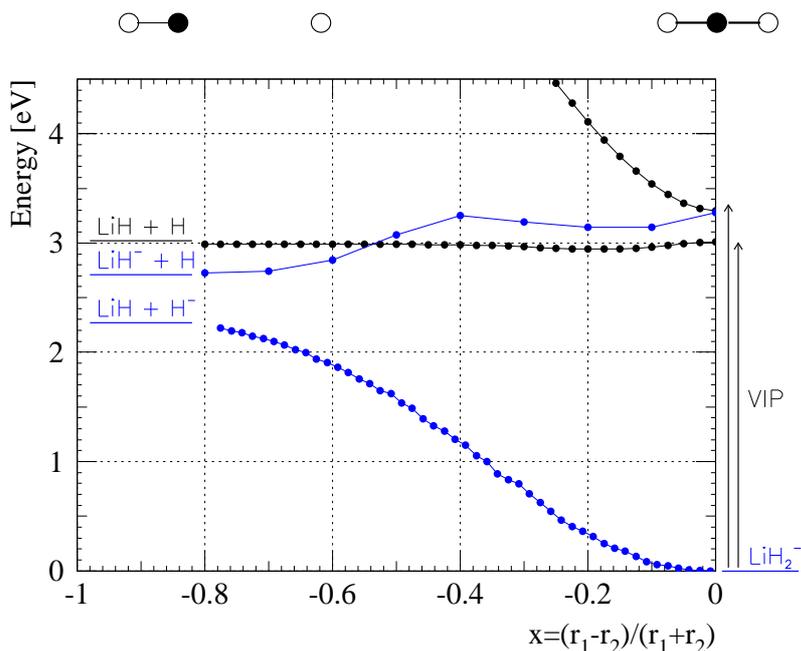
system. Phase space considerations like for the three-body breakup of H$_3^+$ are not necessary here, as the coordinates used here serve only for representation of the potential energy surfaces, not for a detailed study of three-body fragmentation dynamics.

To visualise now the behaviour of these three-dimensional PESs, two-dimensional subsets of the coordinate space are defined by setting one of the hyperangles to a fixed value. The potential energy is then plotted as a function of the second hyperangle with the hyperradius r optimised for minimum energy at each point (separately for each plotted PES). In particular, two such subsets are discussed, which describe the transition from the LiH$_2^-$ equilibrium geometry to the geometries of the two asymptotic channels which were observed in the experiment, namely LiH + H and Li + H$_2$.

Figure 5.10 shows a cut relevant for the transition to the LiH + H asymptote. The bond angle ϕ is fixed to 180° here, thus restricting the parameter space to linear geometries, corresponding to $C_{\infty v}$ symmetry. The LiH$_2^-$ equilibrium geometry is described by $x = 0$, as visualised at
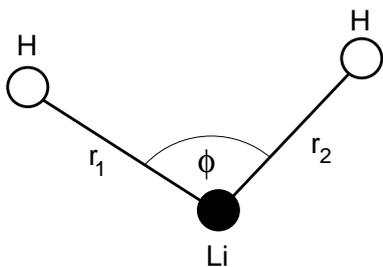
Fig. 5.11: *Definition of the bond lengths r_1, r_2 and the bond angle ϕ used in the description of the LiH$_2$ geometry.*
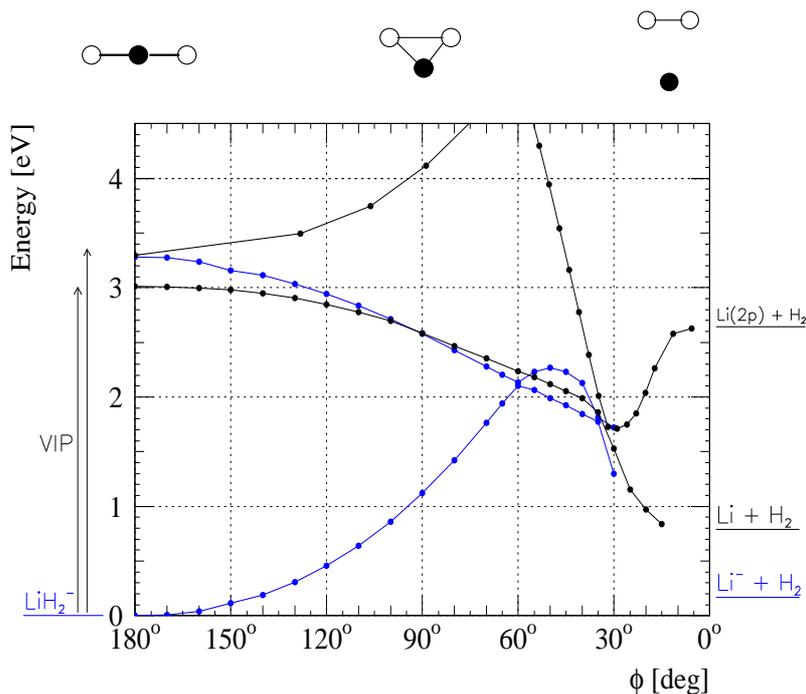
Fig. 5.12: *Calculated potential energy surfaces for the neutral LiH$_2$ (black) and the anionic LiH$_2^-$ system (blue). Energies of the two lowest states are given as a function of ϕ, with x set to 0 and r optimised for each point.*

the top of the figure. For $|x| \to 1$, one of the Li-H distances diverges, corresponding to the LiH + H asymptote. As the two hydrogen atoms are identical, the whole system is symmetric with respect to a change of the sign of x. In Fig. 5.10, only the $x < 0$ part is shown, following up the general arrangement of Fig. 5.1. For both the neutral and the anionic system, the two lowest states are plotted. The asymptotic energy levels given here are taken from Tab. 5.1, but with the small corrections due to zero-point energies removed. The r values resulting from the optimisation are close to the LiH$_2^-$ bond length of 3.3 a.u. near $x = 0$ and diverge for $x \to -1$, corresponding to the separation of the two fragments. The Li-H bond length r_1 calculated from x and r is found to approach (for $x \to -1$) the expected values of 3.0 a.u. for LiH and 3.25 a.u. for LiH$^-$.

In Fig. 5.12, the transition to the Li + H$_2$ asymptote is shown. Here, the parameter space is restricted to the C_{2v} symmetry of isosceles triangles by setting $x = 0$. Again two states of both the neutral and the anionic system are shown. Here the optimised r values stay in the range of 3 a.u. for ϕ between 180° and 30°, and diverge for smaller ϕ, while the H-H distance approaches the H$_2$ equilibrium value of 1.4 a.u.. Although the r-optimisation was done for each state separately, the three curve crossings observed in Fig. 5.12 are not a projection effect due to different r values of these curves, but represent real intersections of the PES involved. An interpretation of these calculations regarding the main results of the experiment is given in the following.

5.4.2 The dominance of the LiH + H channel

An important experimental result at long storage times is the unexpected dominance of the LiH + H dissociation channel. Following the calculations presented here, both the LiH + H channel as well as the Li + H$_2$ channel are energetically open after a vertical transition from the anion geometry to the first neutral PES (indicated by the arrow in Figs. 5.10 and 5.12). However, the neutral ground state potential energy at the LiH + H asymptotic geometry is calculated to be only 20 meV lower than at the LiH$_2^-$ geometry.

Facing this very small energy difference, corrections due to the vibrational zero-point oscillations of both the LiH$_2^-$ and the LiH molecule become important. While the kinetic energy stored in the vibrations of LiH$_2^-$ is available to enlarge the kinetic energy release of a breakup reaction, the corresponding spatial extension of the vibrational wave function can both increase or decrease the potential energy available, depending on the exact shape of the neutral PES in the region covered by this nuclear wave function. In the final channel, the vibrational zero point energy of the LiH molecule has to be provided. To calculate these contributions, a more detailed investigation of the contributing PESs and the resulting vibrational states would be necessary, which is not available at present. As a rough estimate for this energy correction, the kinetic energy stored in the vibrational asymmetric stretching mode of the LiH$_2^-$ molecule might serve, which corresponds to an oscillation of the x coordinate. This energy is semi-classically estimated to be half of the vibrational ground state energy amounting to 68 meV [66]. Therefore, an additional contribution to the energy release in the LiH + H channel of about 34 meV is expected.

The Li + H$_2$ channel, which was anticipated as the result of electron detachment in recent theoretical approaches [9], is found open also in the present calculation, with an energy release of more than 2 eV. Moreover, the minimum energy pathway leading to this channel along the C_{2v} symmetry turns out to be stable against distortions of this symmetry. That is, the introduction of small deviations from $x = 0$ i.e. differences between the bond lengths r_1 and r_2 would raise the energy of the neutral system in the electronic ground state. In contrast to that the pathway to the LiH + H channel along the $C_{\infty v}$ symmetry is instable against symmetry breaking perturbations. However, the $C_{\infty v}$ geometries correspond to a flat maximum of the neutral ground state PES which might allow a fragmentation along this path. Similarly, the gradient of this PES with respect to changes of the bond angle is very small close to the LiH$_2^-$ geometry, which might be unfavourable for a fragmentation into the Li + H$_2$ channel.

An additional process to be taken into account here is the detachment leading to the first excited state of the neutral system, which has a minimum at the anion equilibrium geometry. A transition to this state is expected to be favoured [9] by the good Franck-Condon overlap of the vibrational wave functions of the anion and the electronically excited neutral molecule.

This excited state will then undergo a rapid transition to the neutral ground state, which can be accompanied by a transfer of energy from electronic to vibrational degrees of freedom. The detailed processes governing the transitions between these three PES and in particular the interplay of electronic and vibrational energy might bear the physical reason for the observed dominance of the LiH + H channel.

In summary, a dissociation into the LiH + H channel after electron detachment appears possible from the present *ab initio* calculations. However, the clear dominance of this channel observed in the experiment in contrast to the negligible flux going to the Li + H_2 channel appears to contradict intuition. A more detailed investigation of the PES involved as well as the vibrational dynamics of the system here would be desirable to gain a full theoretical understanding of the observed process.

5.4.3 Possible nature of the transient channel

Another open question is the nature of the transient state of the anion dissociating into the Li + H_2 (+ e^-) and Li^- + H_2 channels, which was observed experimentally at short storage times. In principle, this *transient* state could differ from the usual, *stable* LiH_2^- state in three ways: It could exhibit an exceptional vibrational excitation, an alternative geometry corresponding to a displaced, local minimum of the electronic ground state PES, or belong to another, excited PES.

Vibrational excitation

To access the observed dissociation channels from a vibrationally excited state of the LiH_2^- ion, the system has to overcome an energy barrier of 2.1 eV [66] as confirmed in the present calculations (Fig. 5.12). Without additional energy gained e.g. in a residual gas collision, this would require an excitation of the order of $v = 38$ in the vibrational bending mode, estimated from the harmonic frequency of this mode, which corresponds to an energy of 55 meV [65]. Excitations of the symmetric and asymmetric stretching modes (energies 128 meV and 135 meV) would even increase the height of the barrier by changing the geometry of the system. However, assuming the presence of such high excitations in the first milliseconds of storage, many vibrational states with lower, but still considerable excitation would have to be expected to be even more populated and to live even longer. For these states, a detachment reaction induced by an electron or residual gas collision would have to lead mainly to the Li + H_2 or Li^- + H_2 channel, as the LiH + H channel is energetically closed at the bent geometries connected to high excitations of the vibrational bending modes. Thus, a significant contribution of the Li + H_2 and Li^- + H_2 channels would be expected on a much longer time scale, connected with an increase of the rate in the LiH + H channel. As seen in Fig. 5.9, the experimental data clearly contradicts

this expectation. Thus, the hypothesis of high vibrational excitations being the nature of the transient state appears not very likely.

If one takes into account the possibility of an excitation induced by a residual gas collision to initiate the dissociation process, less high vibrational levels would be needed for the transient state. However, a vibrational excitation of about 1 eV would still be necessary: For lower vibrational levels, and the corresponding bond angles of $\phi > 90°$, a collision induced transition to the first excited anion state would take place at a geometry where the first neutral PES is lower in energy (see Fig. 5.12). In such a case, the observed equal population of both the anion and the neutral dissociation channel would not be expected. For the remaining possibility of a vibrational excitation of $\gtrsim 1$ eV, the same argument still holds as given above for a 2 eV excitation: Such a model cannot explain the observed fast transition from an electron-independent, very rapid dissociation into the Li + H$_2$ and Li$^-$ + H$_2$ channels, to a dissociation which leads exclusively to the LiH + H channel and can be induced by electron-impact.

Alternative geometry

A second possible explanation for a transient state would be the population of a local minimum of the electronic ground state PES at a geometry different from that of the stable state. A good candidate appears to be the *electrostatic complex* configuration Li$^-$(H$_2$) found in recent *ab initio* calculations [14]. The geometry of this complex is close to the Li$^-$ + H$_2$ asymptote with an equilibrium distance of 11.6 a.u. between the Li$^-$ ion and the center of the electrostatically attached H$_2$ molecule. The complex is very weakly bound, with an adiabatic dissociation energy D_0 with respect to the Li$^-$ + H$_2$ asymptote of only 0.9 meV (2.7 meV) for the *para* (*ortho*) nuclear spin configuration of the H$_2$ molecule.

Such a state, if produced in the ion source, would be dissociated by interactions with the surrounding 300 K blackbody radiation, with the observed lifetime of ≈ 3 msec being a reasonable order of magnitude. On the other hand, infrared transitions cannot explain the equal observation of the neutral Li + H$_2$ channel, which requires an additional energy of 0.62 eV. Thus, the dissociation of the electrostatic complex would have to be dominated by residual gas interactions. The observed large fragmentation rate compared to the stable state might in this case be explained by the geometry and binding energy of the electrostatic complex which could result in a large cross section for dissociative residual gas collisions. However, this model of the transient state cannot explain the equal rate in both the anionic and the neutral fragmentation channel. In addition, a large cross section also for electron induced dissociation would be expected here, which is not observed.

Electronically excited state

The third possibility to be taken into account as a transient state is a metastable state belonging to a electronically excited PES of the anion. This would require a local minimum of an excited PES at a geometry that allows for the breakup into $Li + H_2$, as well as $Li^- + H_2$. In addition, the energy of this state would have to be below the energy of the neutral system at the same geometry. Otherwise, a rapid autodetachment would inhibit the fragmentation into $Li^- + H_2$.

A good candidate for such a situation might be the conical intersection of the two lowest electronic states of the anion which appears at the geometry of an equilateral triangle ($\phi = 60°$, $x = 0$). A vibrational ground state wave function constructed in this conical shaped valley of the second PES would be expected to allow for a much faster transition to the lower surface than the lifetime observed, because of the strong coupling at the intersection point. However, a vibrationally excited state would exhibit a much lower probability density at this geometry. This might explain the observed lifetime of 3 ms.

Following this speculation, the transition to the lower PES would be followed either by an opening of the bond angle and successive vibrational relaxation to the anionic ground state configuration. On the other hand, a further reduction of ϕ is possible, finally leading to the separation of an H_2 molecule. This transition would proceed via a second intersection of the two anionic PESs at $\phi \approx 35°$, a geometry where also the two lowest neutral PESs are energetically very close. Thus, the transition to a neutral PES by autodetachment of an electron appears well possible, and the equal contribution of the $Li + H_2$ and $Li^- + H_2$ channels in the experiment are in good agreement with this model.

5.5   Conclusions

From the fragmentation experiments on the LiH_2^- molecular ion described in this chapter, together with the existing theoretical work and new preliminary calculations, the following conclusions can be drawn:

After some milliseconds of internal relaxation following the production of the anion, the electron-induced fragmentation of LiH_2^- is dominated by the detachment of an electron and the subsequent dissociation into the neutral $LiH + H$ channel. The fragmentation proceeds in the geometrically unstable electronic ground state of the neutral system, whereas the first excited neutral state is likely to play an important role as an intermediate state. The strong dominance of the $LiH + H$ channel over the $Li + H_2$ channel, which was clearly observed in the experiment, is at present not understood theoretically. A breakup into a channel containing a negative fragment via a dissociative excitation reaction was not observed, which is in agreement with the new calculations.

The second and just as much unexpected result is the finding of a transient state of the anion with a lifetime of 2.8 ms which was estimated to have a population of ∼5–25% directly after production of the molecular ions. This state was found to decay rapidly, and basically independent of electron impact, by fragmentation into both the Li + H$_2$ and Li$^-$ + H$_2$ channels (at equal rate). Additionally a transition to the stable LiH$_2^-$ ground state is possible.

A tentative interpretation of this state as a metastable bound state located at a conical intersection of the two lowest anionic PES appears thinkable. Detailed theoretical calculations are desirable here to study the lifetime expected for such a complex (taking into account also vibrational and rotational excitations which might inhibit a fast decay) and thus verify or reject this explanation of the experimental findings. On the other hand, a high excitation of the vibrational bending mode in the electronic ground state can, while seeming unlikely, not be excluded completely. Also here, theoretical calculations, e.g. of radiative lifetimes could shed more light on the possible nature of the transient state.

On the experimental side, the next steps now could be investigations of the short-time breakup in an environment where the residual gas pressure or the surrounding temperature can be changed. Thus the influence of residual gas collisions as well as blackbody radiation on the breakup process could be tested.

6. Discussion and outlook

In the present work, the fragmentation of several triatomic molecular ions after electron impact has been studied. For the analysis and interpretation of the data recorded in different types of experiments, standard fragment detection and imaging methods established for studies of diatomic molecules had to be reconsidered and extended in several aspects for the application on these polyatomic systems.

The dissociative recombination of H_3^+ and its isotopomers was studied using neutral fragment imaging techniques aiming at the disclosure of breakup dynamics in the two fragmentation channels. Due to the appearance of more than one channel, a basic problem here is the identification of the breakup channel corresponding to each observed event, which is connected to the problem of an assignment of masses to all recorded fragments. Both problems could be solved by a careful analysis of the center of mass (c.m.) for each observed event, even in the cases of the asymmetric isotopomers of H_3^+, in which one or two protons are replaced by deuterons. Besides the identification of fragment masses and breakup channels, suitable cuts on the c.m. also provide an efficient suppression of background data stemming from incompletely detected or erroneously assigned fragmentation events. The influence of remaining background events on the final results, both quantitatively and qualitatively, could be estimated directly from the measured data. This procedure can in principle be applied also on larger systems containing more atoms and exhibiting more possible breakup channels, provided that a good collimation of the molecular ion beam is given, which results in a good definition of the true c.m. position of all dissociation events.

For the representation of the imaging data in the three-body full breakup channel, a method yielding an unbiased view on the distribution of fragmentation geometries was derived. While applied here on the relatively simple case of a triatomic system containing two identical atoms, this method can easily be further extended to cover the case of three different species. For an extension to larger systems, additional considerations would be necessary regarding the representation of the higher-dimensional data. However, the derivation of a suitable method of data representation would in this case follow the same general procedures as applied for the triatomic case.

The interpretation of imaging data taken in these experiments implies a thorough consider-

ation of quantities that cannot be measured by the present data acquisition system. These are in particular the exact location of a fragmentation event within the electron interaction region, and the orientation of the fragmenting system with respect to the surface of the 2D imaging detector. These uncertainties were taken into account by modelling the fragmentation reaction and the detection system employing a Monte Carlo simulation algorithm. Through the comparison of simulated and experimental data, interesting details of the dissociation process could be revealed from both the total energy release and the correlation between the kinetic energies of the emerging fragments.

In another experiment the dissociation of the LiH_2^- system following electron detachment induced by the impact of a free electron was investigated. Here the branching ratios of the occurring exit channels were studied through an application and extension of the well established grid method. To get an estimate of the contribution of each of the ten channels that had to be taken into account here, the grid method was advanced in two aspects. First, several different grids were employed. Using a suitable normalisation to the total rate, which could not be measured directly, the results for the different grids could then be combined. Second, the algebraic calculation of branching ratios from the measured rates was replaced by an algorithm which takes into account additional boundary conditions like the restriction to non-negative contributions of all channels.

Because of the limited *a priori* knowledge on the reaction studied, a rather large number of fragmentation channels had to be considered. With the extended grid method, it was nevertheless possible to obtain approximative branching ratios for all these channels. In particular, the dominating channels could be identified under different experimental conditions. The accuracy of this method in general depends on the actual conditions in the particular system studied. However, in all cases the results obtained contain additional information when compared to the standard grid method, which often cannot resolve individual channels. The application of the refined method is thus advantageous also for studies of larger molecular systems, or in cases where a large number of channels have to be considered because of strong background contributions.

By application of these techniques, new results could be obtained regarding the physical properties of the fragmentation reactions studied. In particular, for the DR of H_3^+ and its isotopomers the analysis of fragmentation patterns in the three-body channel revealed a preference of linear symmetric breakup geometries. For the heteronuclear isotopomers, an additional strong preference of geometries involving a central D atom, when compared to those with a central H atom, was found. Through the study of the total KER in the three-body channel, a

considerable rotational excitation was found for the stored H_3^+ and D_3^+ ions, but not for H_2D^+ or D_2H^+. The same method was recently applied in the development of a hollow cathode ion source as a diagnostics for monitoring rotational excitations as a function of several parameters describing the source conditions [1].

In the case of LiH_2^-, a dominance of the $LiH + H$ channel in the fragmentation following electron detachment could be observed, as was not expected from theoretical treatments of the system. In addition, a short-lived transient state of the anion with different fragmentation behaviour was found, and some characterisation of this state could be obtained from the experimental data. The variety of results summarised here, which shed new light on several aspects of fragmentation processes of molecular systems, could be achieved only through the described extension of experimental techniques to the situation of polyatomic systems.

Outlook

Having paved the way to more detailed studies of polyatomic systems, several improvements can now be considered regarding the experimental apparatus applied in this work. In particular, for neutral fragment imaging experiments, a 3D detector capable of measuring the impact time difference of the impinging fragments would be desirable. Moreover, a reduction of the relative uncertainty in the flight length from the interaction region to the detector would additionally improve the resolution of KER measurements. Regarding the determination of branching ratios, a considerable improvement of the experimental situation would follow from a change of the geometry of the detector arrangement concerning the recording of charged fragments. Here, a detection system capable of detecting also very light fragments such as H^+, or fragments of opposite charge compared to the stored beam would be desirable.

The technical developments presently being undertaken at the TSR aim at major improvements concerning all these points. In addition to the existing electron cooler device, which was used in the studies discussed here, a new *electron target* was installed in a different section of the storage ring [67]. Beside the advantageous properties of this new electron target, and the new possibilities opening up through the use of two independent electron beams, an important innovation regarding the type of experiments considered here lies in the new detectors for recording fragments of molecular breakup reactions. These detectors in principle are similar to the ones used in this work in connection with the electron cooler, but include several considerable improvements. First, a dedicated new beamline of several meters extends the average flight length L between the electron interaction region and the neutral fragment detector to as much as $12\,m$. With the length of the interaction region being again $\Delta L = 1.5\,m$, this reduces the relative uncertainty of the flight length $\Delta L/L$ from 23% in case of the electron cooler to 13% for the new setup. Second, the neutral fragment imaging detector installed at the new

beamline was designed to be able of recording 3D fragmentation patterns, including the impact time differences of the fragments, through a newly developed two-camera system [71]. With this setup, measurements of both the total kinetic energy release and the breakup geometry of molecular fragmentation reactions will greatly increase in resolution. For example, the weighting procedure in the processing of Dalitz plots then will only represent a minor correction for detector efficiencies, in contrast to the present situation, where the unweighted plots can barely be used in the interpretation of experimental results. The third important innovation will be a detector dedicated for recording fragments of opposite charge compared to the stored beam, which opens up new possibilities in the investigation of branching ratios. The same detector can alternatively be mounted in a position which allows the detection of very light fragments.

In addition to these new technical developments concerning the initiation and detection of fragmentation reactions, new techniques are currently being tested also regarding the production of molecular ions and in particular the control of their internal excitations. As seen in the case of H_3^+, these internal excitations can play an important role in molecular fragmentation processes. While the already noted new hollow cathode ion source was shown to produce already less rotational excitations [1] than the standard CHORDIS sources, a new source including a radio frequency ion trap for cooling and manipulation of the molecular ions is now about to be connected to the accelerator setup [37].

The technical innovations shortly listed here together with the methods of data analysis presented in this work are anticipated to provide new insight in a variety of molecular fragmentation reactions in the near future. In addition to the molecular systems considered here, for which high-resolution measurements could reveal even more detailed information, new studies of various other systems can be considered, among them e.g. the dissociative recombination of CH_2^+, NH_2^+, H_2O^+ or the even larger species H_3O^+, $HNCH^+$ or $HCOH^+$. Within the permanent process of improvements and extensions of both the experimental techniques and the methods applied in the data analysis, the considerations for polyatomic systems presented in this work represent an important step towards new studies employing these larger systems.

Appendix

A Properties of Dalitz plots

A.1 Derivation of the Dalitz coordinates

As seen in Sec. 4.3.2, a pair of coordinates (η_1, η_2) which describes the shape of the fragmentation pattern resulting from a three-body breakup reaction should be a linear combination of single fragment energies in order to ensure a constant phase space density in the kinematically allowed region of the coordinate space. In addition, the graphical representation should reflect the given permutation symmetry of the three identical fragments in terms of simple geometric symmetries.

All permutations of three objects, that is all operations belonging to the S_3 group can be written as the product of two operations: The *transposition* τ_{12} describing the exchange of object 1 and 2, and the *cycle* C_{123}, which replaces object 1 by 2, 2 by 3 and 3 by 1. Obviously, a double application of τ_{12} as well as a triple application of C_{123} will leave the system unchanged. A graphical equivalent of these operations in a two-dimensional plane (as it is spanned by the desired set of two coordinates), is given as follows: The transposition τ_{12} corresponds to the reflection about a given mirror axis, while the cycle C_{123} is represented by a rotation through $120°$ about a point contained by the mirror axis.

Following these considerations, an unbiased representation of fragmentation geometries is achieved by choosing two coordinates which are linear combinations of fragment energies and whose transformation under permutations of the fragments is given by the mentioned geometric operations.

We therefore start with the ansatz

$$\eta_1(E_1, E_2, E_3) = a_1 E_1 + b_1 E_2 + c_1 E_3 \qquad \text{(A.1a)}$$

$$\eta_2(E_1, E_2, E_3) = a_2 E_1 + b_2 E_2 + c_2 E_3 . \qquad \text{(A.1b)}$$

As the center of the rotation mediated by the C_{123} operation we choose the origin $(\eta_1, \eta_2) = (0,0)$. Furthermore, the mirror axis corresponding to the τ_{12} operation is chosen to be the line $\eta_1 = 0$. A reflection about this axis is thus performed by a change of the sign of η_1. The

condition that this reflection should represent the operation τ_{12} is thus formulated as

$$\eta_1(E_2, E_1, E_3) \;=\; -\eta_1(E_1, E_2, E_3) \tag{A.2a}$$

$$\eta_2(E_2, E_1, E_3) \;=\; \eta_2(E_1, E_2, E_3) \,. \tag{A.2b}$$

From (A.2a) follows with (A.1a)

$$a_1 E_2 + b_1 E_1 + c_1 E_3 \;=\; -a_1 E_1 - b_1 E_2 - c_1 E_3 \,.$$

$$\Rightarrow \quad (a_1 + b_1)(E_1 + E_2) + 2c_1 E_3 \;=\; 0 \,.$$

As this has to hold for all (E_1, E_2, E_3), we get

$$a_1 = -b_1 \qquad \text{and} \qquad c_1 = 0 \,.$$

and therefore

$$\eta_1(E_1, E_2, E_3) = a_1(E_1 - E_2) \,. \tag{A.3}$$

As the second symmetry condition we demand that the operation C_{123} corresponds to a rotation through $120°$ about the origin, that is

$$\begin{pmatrix} \eta_1(E_2, E_3, E_1) \\ \eta_2(E_2, E_3, E_1) \end{pmatrix} = \begin{pmatrix} -\frac{1}{2} & \frac{1}{2}\sqrt{3} \\ -\frac{1}{2}\sqrt{3} & -\frac{1}{2} \end{pmatrix} \begin{pmatrix} \eta_1(E_1, E_2, E_3) \\ \eta_2(E_1, E_2, E_3) \end{pmatrix} \,. \tag{A.4}$$

This means in particular

$$\eta_1(E_2, E_3, E_1) = \frac{1}{2}\left(-\eta_1(E_1, E_2, E_3) + \sqrt{3}\,\eta_2(E_1, E_2, E_3) \right) \,,$$

and with (A.3) and $E_{\text{kin}} = E_1 + E_2 + E_3$ follows

$$\begin{aligned} \eta_2(E_1, E_2, E_3) \;&=\; \frac{2}{\sqrt{3}}\,a_1(E_2 - E_3) + \frac{1}{\sqrt{3}}\,a_1(E_1 - E_2) \\ &=\; \frac{a_1}{\sqrt{3}}\,(E_1 + E_2 - 2E_3) \\ &=\; \frac{a_1}{\sqrt{3}}\,(E_{\text{kin}} - 3E_3) \,. \end{aligned} \tag{A.5}$$

The remaining coefficient a_1 defines the overall normalisation of the (η_1, η_2) coordinates without affecting the symmetry properties. We chose arbitrarily $a_1 = (-\sqrt{3}E_{\text{kin}})^{-1}$ and finally get from (A.3) and (A.5) the dimensionless *Dalitz* coordinates:

$$\eta_1(E_1, E_2, E_3) \;=\; \frac{E_2 - E_1}{\sqrt{3}E_{\text{kin}}} \tag{A.6a}$$

$$\eta_2(E_1, E_2, E_3) \;=\; \frac{E_3}{E_{\text{kin}}} - \frac{1}{3} \,. \tag{A.6b}$$

A.2 Energetically allowed region

The allowed region in the (η_1, η_2) plane is firstly constrained by the requirement that all fragment energies have to be non-negative. To calculate the consequences of this requirement, the generalised form (4.14) of the Dalitz coordinates (η_1, η_2) is directly used here, which is equivalent to the standard Dalitz coordinates (4.13) in case of the homonuclear species.

The coordinates (4.14) can be written as

$$\eta_1 = \sqrt{\frac{M}{m_3}} \frac{E_2 - E_1}{3E_{\mathrm{kin}}}, \qquad \eta_2 = \frac{m + m3}{3m} - \frac{M}{3m} \frac{E_1 + E_2}{E_{\mathrm{kin}}}, \qquad (A.7)$$

with $m = m_1 = m_2$ and $M = \sum m_i = 2m + m_3$. The requirement of non-negative energies then leads to

$$E_1 \geq 0 \;\; \Rightarrow \;\; E_2 \geq 3 \sqrt{\frac{m_3}{M}} E_{\mathrm{kin}} \eta_1$$

$$\Rightarrow \;\; \eta_2 \leq \frac{m + m3}{3m} - \frac{\sqrt{m_3 M}}{m} \eta_1 \qquad (A.8)$$

$$E_2 \geq 0 \;\; \Rightarrow \;\; E_1 \geq -3 \sqrt{\frac{m_3}{M}} E_{\mathrm{kin}} \eta_1$$

$$\Rightarrow \;\; \eta_2 \leq \frac{m + m3}{3m} + \frac{\sqrt{m_3 M}}{m} \eta_1 \qquad (A.9)$$

$$E_3 \geq 0 \;\; \Rightarrow \;\; \eta_2 \geq -\frac{1}{3} . \qquad (A.10)$$

This defines a triangular area in the $\eta_1 \eta_2$ plane (see Fig. 4.5). In the case of homonuclear molecules, $m = m_3$, these results simplify to

$$-1 \;\leq\; \eta_2 - \frac{2}{3} \;\leq\; |\sqrt{3}\, \eta_1| , \qquad (A.11)$$

as indicated by the triangle in Fig. 4.4a.

A.3 Restrictions through momentum conservation

To conserve the total momentum of the fragmenting molecule, the momenta $\vec{p}_i$ of the three fragments in the co-moving c.m. frame have to add to zero:

$$\sum_{i=1}^{3} \vec{p}_i = \vec{0} .$$

The absolute values p_i of the fragment momenta then have to obey

$$|p_1 - p_2| \;\leq\; p_3 \;\leq\; |p_1 + p_2| .$$

From this follows

$$(p_1 - p_2)^2 \leq p_3^2 \leq (p_1 + p_2)^2$$
$$\Rightarrow \quad -2p_1p_2 \leq p_3^2 - p_1^2 - p_2^2 \leq 2p_1p_2$$
$$\Rightarrow \quad |p_3^2 - p_1^2 - p_2^2| \leq 2p_1p_2 \,.$$

Using $E_i = p_i^2/2m_i$ and $m := m_1 = m_2$ (but retaining the possibility that $m \neq m_3$ as in case of the heteronuclear isotopomers of H_3^+), we get

$$\left| \frac{m_3}{m} E_3 - E_2 - E_1 \right| \leq 2\sqrt{E_1 E_2}$$
$$\Rightarrow \quad \left(\frac{m_3}{m} E_3 - E_2 - E_1 \right)^2 \leq 4E_1 E_2$$
$$\Rightarrow \quad (E_1 - E_2)^2 - (E_1 + E_2)^2 + \left(\frac{m_3}{m} E_3 - E_2 - E_1 \right)^2 \leq 0$$
$$\Rightarrow \quad (E_1 - E_2)^2 + \left(\frac{m_3}{m} E_3 \right) \left(\frac{m_3}{m} E_3 - 2E_2 - 2E_1 \right) \leq 0$$

and thus, with $E_{\text{kin}} = E_1 + E_2 + E_3$ and $M = 2m + m_3$,

$$(E_1 - E_2)^2 + \left(\frac{m_3}{m} E_3 \right) \left(\frac{M}{m} E_3 - 2E_{\text{kin}} \right) \leq 0$$
$$\Rightarrow \quad (E_1 - E_2)^2 + \frac{m_3 M}{m^2} E_3^2 - 2 \frac{m_3}{m} E_{\text{kin}} E_3 \leq 0$$
$$\Rightarrow \quad (E_1 - E_2)^2 + \left(\frac{\sqrt{m_3 M}}{m} E_3 - \sqrt{\frac{m_3}{M}} E_{\text{kin}} \right)^2 \leq \frac{m_3}{M} E_{\text{kin}}^2$$
$$\Rightarrow \quad \left(\sqrt{\frac{M}{3m_3}} \frac{E_2 - E_1}{\sqrt{3} E_{\text{kin}}} \right)^2 + \left(\frac{M}{3m} \frac{E_3}{E_{\text{kin}}} - \frac{1}{3} \right)^2 \leq \left(\frac{1}{3} \right)^2 . \qquad \text{(A.12)}$$

In the case of the homonuclear isotopomers, where $m_3 = m = M/3$, we can write (A.12) using the Dalitz coordinates (4.13) as

$$\eta_1^2 + \eta_2^2 \leq \left(\frac{1}{3} \right)^2 .$$

Therefore the area in the (η_1, η_2)-plane, which is allowed by momentum conservation, is defined by a circle around the origin with a radius of $\frac{1}{3}$. Moreover, the form of (A.12) suggests a more general definition of the Dalitz coordinates:

$$\eta_1 = \sqrt{\frac{M}{3m_3}} \frac{E_2 - E_1}{\sqrt{3} E_{\text{kin}}}, \qquad \eta_2 = \frac{M}{3m} \frac{E_3}{E_{\text{kin}}} - \frac{1}{3} \qquad \text{(A.13)}$$

This definition is equivalent to (4.13) for the homonuclear case, and results in the same circular area as the momentum allowed region for all four isotopomers.

B   Reconstruction of branching ratios in the fragmentation of LiH$_2^-$

When employing a grid with transmission probability T in front of the neutral fragment detector, the probabilities P_m to detect an event with a total neutral fragment mass m are connected to the branching fractions α_i of the possible channels i listed in Eq. (5.8) by the equation

$$\vec{P} = A\vec{\alpha} \tag{B.1}$$

with $\vec{P} = (P_1, P_2, P_7, P_8, P_9)^\top$, $\vec{\alpha} = (\alpha_1, \ldots, \alpha_{10})^\top$ and

$$A = \begin{pmatrix} 0 & T(1-T) & 0 & 2T(1-T)^2 & 0 & T(1-T) & 0 & 0 & 2T(1-T) & T \\ 0 & 0 & T(1-T) & T^2(1-T) & 0 & 0 & 0 & T & T^2 & 0 \\ 0 & 0 & T(1-T) & T(1-T)^2 & 0 & T(1-T) & T & 0 & 0 & 0 \\ 0 & T(1-T) & 0 & 2T^2(1-T) & T & T^2 & 0 & 0 & 0 & 0 \\ T & T^2 & T^2 & T^3 & 0 & 0 & 0 & 0 & 0 & 0 \end{pmatrix} \tag{B.2}$$

The matrix A is obviously not invertible. Even when using several grids with different T, that is, adding observables to $\vec{P}$ and thus adding rows to A, a direct calculation of $\vec{\alpha}$ from $\vec{P}$ turns out to be impossible. Nevertheless, a lot of information on $\vec{\alpha}$ can be deduced from $\vec{P}$. Using the reconstruction algorithm described in the following, at least upper and lower limits can be given for all α_i, with the range between these limits depending on the actual values of the P_m. For the studies of LiH$_2^-$ considered here, all α_i can be determined with an uncertainty of some percent.

The reconstruction algorithm uses as input the mass ratios $\vec{P}^0$ measured without application of any grid (that is, with a transmission factor of $T_0 = 1$), the ratios $\vec{P}^g$ measured with grid #g in place ($g = 1,2$), and the transmission factors T_g of the grids which were determined in a separate experiment (see Sec. 5.2).

The total number of dissociation events reaching the detection setup cannot be measured, as for an unknown fraction P_0^g of these events all fragments are stopped by the grid. Thus, the rates P_m for different masses can be given only relative to each other, but not in the form of absolute detection probabilities (which would require the normalisation $\sum_{m=0,1,2,7,8,9} P_m = 1$). However, a consistent normalisation of the vectors $\vec{P}^g$ is necessary to enable a comparison of the mass fractions observed with different grids. Inspection of the matrix A here yields the useful relation $\sum_{m=7,8,9} P_m = T \cdot \sum_{i=1..7} \alpha_i$. Thus, a normalisation of the mass fractions such that $\sum_{m=7,8,9} P_m^g = T_g$ results in a normalisation of the branching factors α_i corresponding to $\sum_{i=1..7} \alpha_i = 1$, which is independent of the grid in use.

(In other words, by setting the probability $\sum_{m=7,8,9} P_m$ for the detection of a fragment with $m \geq 7$ to the transmission of the grid, the branching factors of all channels are expressed in units

of the total branching factor for events which include a neutral Li atom, that is $\sum_{i=1..7} \alpha_i = 1$. This can be done for each grid individually, and thus the measured P_m^g values can be expressed in the same units for all m and all g.)

After the determination of all α_i, the vector $\vec{\alpha}$ can be re-normalised to fulfil $\sum_{i=1}^{10} \alpha_i = 1$.

To simplify the algebraic expressions used in the following, both sides of Eq. (B.1) are divided by T. Thus, the equation

$$\vec{p} = A'\vec{\alpha} \tag{B.3}$$

is used with $\vec{p} = \vec{P}/T$ and $A' = A/T$. Obviously, $\vec{p}$ is now normalised such that $\sum_{m=7,8,9} p_m = 1$, while A' is simplified by factoring out of the factor T common to each entry of A.

From the relative count rates for $m = 9$ one then obtains

$$p_9^g = \alpha_1 + T_g (\alpha_2 + \alpha_3) + T_g^2 \alpha_4 . \tag{B.4}$$

This equation contains the only information accessible for α_1, as the last row of A (corresponding to $m = 9$) is the only one with a nonzero entry in the first column (connected to α_1). As (B.4) constitutes a second order polynomial in T_g, the mass fraction p_9^g has to be known for three different values of T_g in order to determine the three parameters α_1, $(\alpha_2 + \alpha_3)$ and α_4. At this point, the use of two different grids (in addition to one measurement without grid) is crucial in the reconstruction of branching factors. The three parameters are then obtained, together with their statistical errors, by fitting a second order polynomial to the three measured values of the function $p_9^g(T_g)$. For the remaining calculations described in the following the use of one grid is sufficient, and the second measurement can be used as a check of consistency.

Inspection of the rate of $m = 7$ events (third row of A) directly yields

$$\alpha_7 = p_7^0 , \tag{B.5}$$

and, using the α_4 obtained above,

$$\alpha_3 + \alpha_6 = \frac{p_7^g - p_7}{1 - T_g} - (1 - T_g)\alpha_4 , \tag{B.6}$$

for either grid $g = 1, 2$.

Similarly, one gets from the $m = 2$ channel

$$\alpha_3 + \alpha_8 = \frac{p_2 - T_g p_2^g}{1 - T_g} - T_g \alpha_4 \tag{B.7}$$

$$\alpha_3 - \alpha_9 = \frac{p_2 - p_2^g}{1 - T_g} - T_g \alpha_4 , \tag{B.8}$$

from the $m = 8$ channel

$$\alpha_2 + \alpha_5 = \frac{p_8^g - T_g p_8}{1 - T_g} - 2T_g \alpha_4 \tag{B.9}$$

$$\alpha_2 - \alpha_6 = \frac{p_8^g - p_8}{1 - T_g} - 2T_g \alpha_4 \,, \tag{B.10}$$

and finally, from $m = 1$

$$\alpha_{10} = p_1^0 \,. \tag{B.11}$$

Taking into account that all α_i have to be non-negative, one can deduce from this an upper limit α_3^{max} and a lower limit α_3^{min} for α_3:

$$\alpha_3^{\mathrm{max}} = \min\left[(\alpha_3 + \alpha_8), (\alpha_3 + \alpha_6), (\alpha_3 + \alpha_2)\right] \tag{B.12}$$

$$\alpha_3^{\mathrm{min}} = \max\left[(\alpha_3 - \alpha_9), (\alpha_3 + \alpha_2) - (\alpha_2 + \alpha_5), 0\right] \,. \tag{B.13}$$

As an estimated value, α_3 is then set to

$$\alpha_3 = \left(\alpha_3^{\mathrm{max}} + \alpha_3^{\mathrm{min}}\right)/2 \tag{B.14}$$

with the well-known systematic error

$$\Delta\alpha = \left(\alpha_3^{\mathrm{max}} - \alpha_3^{\mathrm{min}}\right)/2 \,. \tag{B.15}$$

Using this estimation, α_2, α_5, α_6, α_8 and α_9 can now easily be calculated from (B.4)–(B.10) with the same systematic uncertainty of $\pm\Delta\alpha$.

In addition, statistical errors originating from the measurement of the p_m^g can be calculated for each α_i using standard Gaussian error propagation. The total error typically amounts to few percent in the experiments considered here, which for some channels is in the same order of magnitude as the α_i value obtained. However, using the algorithm described here, it is possible to clearly identify dominant and secondary channels of the fragmentation reaction, as seen in Sec. 5.3.

For some channels, data obtained with either grid #1 or #2 can be used to calculate α_i. In these cases, the deviation of the two results is typically also in the order of few percent. As the final value, the average of the two results is taken with their difference considered an additional contribution to the error.

Finally, the reconstructed vector $\vec{\alpha}$ is normalised to fulfil $\sum_{i=1}^{10} \alpha_i = 1$.

C Decay modes of the *transient state* of LiH$_2^-$

As observed in Sec. 5.3.3, LiH$_2^-$ molecules in the *transient state*, as identified by a fragmentation into Li + H$_2$ or Li$^-$ + H$_2$, show a much faster decay than in the *stable state*, which fragments into the LiH + H channel. At $E_e = 0\,$eV, the decay rates per molecule were found as the inverse of the 1/e lifetime of the observed fragmentation signal as

$$\Gamma^T = 360 \pm 15\,\text{sec}^{-1}\,, \qquad \Gamma^S = 0.63 \pm 0.04\,\text{sec}^{-1}\,, \tag{C.1}$$

with T and S denoting the transient and stable state, respectively. While for the stable state, the observed decay is caused only by residual-gas induced fragmentation of the molecule, for the transient state both a fragmentation and a transition to the stable state has to be considered:

$$\begin{aligned}
\Gamma^T &= \Gamma^T_{\text{frag}} + \Gamma^T_{\text{trans}} \\
\Gamma^S &= \Gamma^S_{\text{frag}}
\end{aligned} \tag{C.2}$$

To estimate the relative size of these two contributions, not only the decay rates per molecule Γ have to be taken into account, but also the absolute count rates of fragmentation events R. These are connected to the decay rates Γ by the number of ions N present in both states:

$$\begin{aligned}
R^S_{(t)} &= \eta\, N^S_{(t)}\, \Gamma^S_{\text{frag}} \\
R^T_{(t)} &= \eta\, N^T_{(t)}\, \Gamma^T_{\text{frag}}
\end{aligned} \tag{C.3}$$

with t the time after injection and η a common factor describing the probability for a fragmentation event to be detected.

Considering the fragmentation rates shown in Fig. 5.9 for $E_e = 0\,$eV, especially the situation at a storage time of $t_2 := 2\,$msec, where the largest contribution of the transient state can be analysed, two observations can be made: Firstly, the total rate in the two transient channels, calculated as $R^T = R_{\text{Li} + \text{H}_2} + R_{\text{H}_2}$, is found to be about a factor of 20 higher than the rate in the stable channel $R^S = R_{\text{LiH} + \text{H}}$, that is

$$R^T_{(t_2)} \approx 20\, R^S_{(t_2)} \tag{C.4}$$

Secondly, an increase of the stable rate R^S at short storage times, as would be expected for a strong transition from the transient state, is not observed. For example, out of the $N^T_{(t_2)}$ transient state molecules present in the beam at $t = t_2$, a fraction of $\Gamma^T_{\text{trans}}/\Gamma^T$ will transform to the stable state, thus increasing the number N^S and the observed rate of fragmentation events R^S. The time scale for this transition is in the order of a few lifetimes of the transient state, that is, several milliseconds. For the increase of R^S in the milliseconds following t_2, an upper limit of

the order of 10% can be estimated from the experimental data, thus setting an upper limit to the number of transient state ions present at t_2:

$$N_{(t_2)}^{\mathrm{T}} \cdot \frac{\Gamma_{\mathrm{trans}}^{\mathrm{T}}}{\Gamma^{\mathrm{T}}} \;\lesssim\; 0.1\, N_{(t_2)}^{\mathrm{S}} \tag{C.5}$$

From (C.4) and (C.3) follows

$$N_{(t_2)}^{\mathrm{T}}\, \Gamma_{\mathrm{frag}}^{\mathrm{T}} \;\approx\; 20\, N_{(t_2)}^{\mathrm{S}}\, \Gamma_{\mathrm{frag}}^{\mathrm{S}} \,. \tag{C.6}$$

The division of (C.5) by (C.6) then yields

$$\frac{\Gamma_{\mathrm{trans}}^{\mathrm{T}}}{\Gamma_{\mathrm{frag}}^{\mathrm{T}}} \;\lesssim\; 0.005\, \frac{\Gamma^{\mathrm{T}}}{\Gamma^{\mathrm{S}}} \;\stackrel{\mathrm{(C.1)}}{\approx}\; 3 \tag{C.7}$$

The estimates performed here thus result in an upper limit of $\approx 75\%$ for the contribution $\Gamma_{\mathrm{trans}}^{\mathrm{T}}/\Gamma^{\mathrm{T}}$ of a transition to the stable state in the total decay rate of the transient state. A lower limit higher than 0% cannot be given here as no lower limit for an increase of R^{S} was found in the experimental data. From these boundaries, some conclusions can be drawn on the absolute rates of transition and fragmentation:

$$\begin{aligned}
0 &\;\leq\; \Gamma_{\mathrm{trans}}^{\mathrm{T}} \;\lesssim\; 270\,\mathrm{sec}^{-1} \\
90\,\mathrm{sec}^{-1} &\;\lesssim\; \Gamma_{\mathrm{frag}}^{\mathrm{T}} \;\lesssim\; 360\,\mathrm{sec}^{-1}
\end{aligned} \tag{C.8}$$

It should be noted again that these numbers are not more than very rough estimates, as no exact values can be extracted from the data available. However, an important conclusion still possible is that the fragmentation rate $\Gamma_{\mathrm{frag}}^{\mathrm{T}}$ found for the transient state is about two orders of magnitude higher than $\Gamma_{\mathrm{frag}}^{\mathrm{S}}$ for the stable state. Even without knowledge of more accurate numbers, this gives already an important clue for a possible interpretation of the nature of the transient state.

Following this result, also the relative population n^{T} of the transient state in the ion beam can be estimated. Using (C.8) and (C.6) one obtains

$$n_{(t_2)}^{\mathrm{T}} := \frac{N_{(t_2)}^{\mathrm{T}}}{N_{(t_2)}^{\mathrm{T}} + N_{(t_2)}^{\mathrm{S}}} \;\approx\; 3.4\% - 12\% \,, \tag{C.9}$$

which can be extrapolated using (C.1) to the population at the time of injection $t_0 := 0\,\mathrm{msec}$, yielding

$$n_{(t_0)}^{\mathrm{T}} \;\approx\; 7\% - 24\% \,. \tag{C.10}$$

References

[1] S. Altevogt, *Production of rotationally cold H_3^+ ions with a hollow cathode ion source*, Diploma thesis, Universität Heidelberg, 2003.

[2] Z. Amitay, A. Baer, M. Dahan, L. Knoll, M. Lange, J. Levin, I. F. Schneider, D. Schwalm, A. Suzor-Weiner, Z. Vager, R. Wester, A. Wolf, and D. Zajfman, *Dissociative recombination of vibrationally excited HD^+: State selected experimental investigation*, Phys. Rev. A **60** (1999), 3769.

[3] Z. Amitay, D. Zajfman, P. Forck, U. Hechtfischer, B. Seidel, M. Grieser, D. Habs, D. Schwalm, and A. Wolf, *Dissociative recombination of CH^+ – cross section and final states*, Phys. Rev. A **54** (1996), 4032–4050.

[4] L. H. Andersen, P. Hvelplund, D. Kella, P. H. Mokler, H. B. Pedersen, H. T. Schmidt, and L. Vejby-Christensen, *Resonance structure in the electron-impact detachment cross section of C_2^- caused by the formation of C_2^{2-}*, J. Phys. B **29** (1996), L643–L649.

[5] T. Andersen, H.K. Haugen, and H. Hotop, *Binding energies in atomic negative ions: III*, J. Phys. Chem. Ref. Data **28** (1999), 1511–1533.

[6] M. Beckert and U. Müller, *Molecular many-body dissociation: Data reduction strategies in translational spectroscopy*, Eur. Phys. J. D **12** (2000), 303–310.

[7] M. Beutelspacher, M. Grieser, D. Schwalm, and A. Wolf, *Longitudinal and transverse electron cooling experiments at the heidelberg heavy ion storage ring TSR*, Nucl. Instr. Meth. A **441** (2000), 110–115.

[8] G. Bisoffi, M. Grieser, E. Jaeschke, D. Krämer, and A. Noda, *Radiofrequency stacking experiments at the Heidelberg Test Storage Ring*, Nucl. Instr. Meth. A **287** (1990), 320–323.

[9] A. I. Boldyrev and J. Simons, *Vertical and adiabatical ionization potentials of MH_{k+1}^- anions. ab initio study of the structure and stability of hypervalent MH_{k+1} molecules*, J. Chem. Phys. **99** (1993), 4628.

[10] M. Born and R. Oppenheimer, *Zur Quantentheorie der Molekeln*, Ann. Phys. **84** (1927), 457.

[11] P. R. Bunker, *Molecular symmetry and spectroscopy*, Academic press, New York, 1979.

[12] A. Cassimi, M. Tarisien, G. Laurent, P. Sobocinski, L. Adoui, J.Y. Chesnel, F. Frémont, B. Gervais, and D. Hennecart, *Charged-particle-induced molecular fragmentation at large velocities*, Many-Particle Quantum Dynamics in Atomic and Molecular Fragmentation (J. Ullrich and V. P. Shevelko, eds.), Springer, Berlin Heidelberg, 2003.

[13] W. Cencek, J. Rychlewski, R. Jaquet, and W. Kutzelnigg, *Sub-microhartree accuracy potential energy surface for H_3^+ including adiabatic and relativistic effects. I. Calculation of the potential points*, J. Chem. Phys. **108** (1998), 2831.

[14] D. T. Chang, G. Suttatt, G. Ristroff, and G. I. Gellene, *First principles determination of the bound levels of $Li^-(H_2)$*, J. Chem. Phys. **116** (2002), 9188.

[15] J.-J. Chen and K.-C. Lin, *Influence of vibrational excitation on the reaction $Li(2\,^2P_J) + H_2(v=1) \rightarrow LiH(X\,^1\Sigma^+) + H$*, J. Chem. Phys. **119** (2003), 8785–8789.

[16] P. C. Cosby and H. Helm, *Experimental determination of the H_3^+ bond dissociation energy*, Chem. Phys. Lett. **152** (1988), 71.

[17] R. H. Dalitz, *On the analysis of τ-meson data and the nature of the τ-meson*, Phil. Mag. **44** (1953), 1068.

[18] S. Datz, M. Larsson, C. Stromholm, G. Sundström, V. Zengin, H. Danared, A. Källberg, and M. af Ugglas, *Dissociative recombination of H_2D^+: Cross sections, branching fractions, and isotope effects*, Phys. Rev. A **52** (1995), 2901.

[19] S. Datz, G. Sundström, Ch. Biedermann, L. Broström, H. Danared, S. Mannervik, J. R. Mowat, and M. Larsson, *Branching processes in the dissociative recombination of H_3^+*, Phys. Rev. Lett. **74** (1994), 896.

[20] T. Tanabe et al., *Dissociative recombination at the TARN II storage ring*, Dissociative Recombination: Theory, Experiment and Applications IV (M. Larsson, J. B. A. Mitchell, and I. F. Schneider, eds.), 2000, p. 170.

[21] E. E. Eyler and N. Melikechi, *Near-threshold continuum structure and the dissociation energies of H_2, HD, and D_2*, Phys. Rev. A **48** (1993), R18–R21.

[22] M. J. Gaillard, D. S. Gemmell, G. Goldring, I. Levine, W. J. Pietsch, J. C. Poizat, A. J. Ratkowski, J. Remillieux, Z. Vager, and B. J. Zabransky, *Experimental determination of the structure of H_3^+*, Phys. Rev. A **17** (1978), 1797.

[23] U. Galster, U. Müller, and H. Helm, *Maps of nonadiabatic coupling in triatomic hydrogen*, Phys. Rev. Lett. **92** (2004), 073002.

[24] T. R. Geballe and T. Oka, *Detection of H_3^+ in interstellar space*, Nature **384** (1996), 334.

[25] D. Habs, W. Baumann, J. Berger, P. Blatt, A. Faulstich, P. Krause, G. Kilgus, R. Neumann, W. Petrich, R. Stokstad, D. Schwalm, E. Szmola+, K. Welti, A. Wolf, S. Zwickler, E. Jaeschke, D. Krämer, G. Bisoffi, M. Blum, A. Friedrich, C. Geyer, M. Grieser, H. W. Heyng, B. Holzer, R. Ihde, M. Jung, K. Matl, W. Ott, B. Povh, R. Repnow, M. Steck, E. Steffens D. Dutta, T. Kühl, D. Marx S. Schröder, M. Gerhard, R. Grieser, G. Huber, R. Klein, M. Krieg, N. Schmidt, R. Schuch, J. F. Babb, L. Spruch, W. Arnold, and A. Noda, *First experiments with the heidelberg test storage ring TSR*, Nucl. Instr. Meth. B **43** (1989), 390–410.

[26] E. Heinicke, K. Bethge, and H. Baumann, *A universal ion source for tandem accelerators*, Nucl. Instr. Meth. **58** (1968), 125–133.

[27] H. Helm and U. Müller, *Laser-induced fragmentation of triatomic hydrogen*, Many-Particle Quantum Dynamics in Atomic and Molecular Fragmentation (J. Ullrich and V. P. Shevelko, eds.), Springer, Berlin Heidelberg, 2003.

[28] E. Herbst, *Chemistry in the interstellar medium*, Annu. Rev. Phys. Chem. **46** (1995), 27–53.

[29] E. Herbst and W. Klemperer, *The formation and depletion of molecules in dense interstellar clouds*, Astrophys. J. **185** (1973), 505–533.

[30] R. K. Janev, *Role of dissociative recombination and related molecular processes in fusion edge plasmas*, Dissociative Recombination: Theory, Experiment and Applications IV (M. Larsson, J. B. A. Mitchell, and I. F. Schneider, eds.), 2000, p. 40.

[31] R. Jaquet, W. Cencek, W. Kutzelnigg, and J. Rychlewski, *Sub-microhartree accuracy potential energy surface for H_3^+ including adiabatic and relativistic effects. II. Rovibrational analysis for H_3^+ and D_3^+*, J. Chem. Phys. **108** (1998), 2837.

[32] M. J. Jensen, H. B. Pedersen, C. P. Safvan, K. Seiersen, X. Urbain, and L. H. Andersen, *Dissociative recombination and excitation of H_3^+*, Phys. Rev. A **63** (2001), 052701.

[33] R. Keller, B. R. Nielsen, and B. Torp, *Metal beam production using a high current ion source*, Nucl. Instr. Meth. B **37/38** (1989), 74–77.

[34] K. H. Kim, Y. S. Lee, T. Ishida, and G.-H. Jeung, *Dynamics calculations for the LiH + H ↔ Li + H_2 reactions using interpolations of accurate ab initio potential energy surfaces*, J. Chem. Phys. **119** (2003), 4689–4693.

[35] V. Kokoouline and C. H. Greene, *Theory of dissociative recombination of D_{3h} triatomic ions applied to H_3^+*, Phys. Rev. Lett. **90** (2003), 133201.

[36] V. Kokoouline and C. H. Greene, *Unified theoretical treatment of dissociative recombination of D_{3h} triatomic ions: Application to H_3^+ and D_3^+*, Phys. Rev. A **68** (2003), 12703.

[37] H. Kreckel, *Internal excitations of stored triatomic hydrogen molecular ions*, Ph.D. thesis, Universität Heidelberg, 2003.

[38] H. Kreckel, S. Krohn, L. Lammich, M. Lange, J. Levin, M. Scheffel, D. Schwalm, J. Tennyson, Z. Vager, R. Wester, A. Wolf, and D. Zajfman, *Vibrational and rotational cooling of H_3^+*, Phys. Rev. A **66** (2002), 052509.

[39] S. Krohn, *Inelastic collisions and recombination between electrons and molecular ions*, Ph.D. thesis, Universität Heidelberg, 2001.

[40] S. Krohn, Z. Amitay, A. Baer, J. Levin, D. Zajfman, M. Lange, L. Knoll, D. Schwalm, R. Wester, and A. Wolf, *Electron induced vibrational de-excitation of H_2^+*, Phys. Rev. A **62** (2000), 032713.

[41] H. W. Kroto, *Molecular rotation spectra*, Dover Publications, 1992.

[42] L. Lammich, H. Kreckel, S. Krohn, M. Lange, D. Schwalm, D. Strasser, A. Wolf, and D. Zajfman, *Breakup dynamics in the dissociative recombination of H_3^+ and its isotopomers*, Rad. Phys. Chem. **68** (2003), 175–179.

[43] L. Lammich, D. Strasser, H. Kreckel, M. Lange, H. B. Pedersena, S. Altevogt, V. Andrianarijaona, H. Buhr, O. Heber, P. Witte, D. Schwalm, A. Wolf, and D. Zajfman, *Evidence for subthermal rotational populations in stored molecular ions through state-dependent dissociative recombination*, Phys. Rev. Lett. **91** (2003), 143201.

[44] G. Laricchia, *Scattering of positrons and positronium by atoms and molecules*, Proceedings of the International Conference on Photonic, Electronic and Atomic Collisions, Santa Fe 2001 (J. Burgdörfer, J. S. Cohen, S. Datz, and C. R. Vane, eds.), Rinton press, Princeton, 2002.

[45] M. Larsson, *Experimental studies of the dissociative recombination of H_3^+*, Phil. Trans. R. Soc. Lond. A **358** (2000), 2433–2444.

[46] H. S. Lee, Y. S. Lee, and G.-H. Jeung, *Potential energy surfaces for LiH_2 and photochemical reactions $Li^* + H_2 \leftrightarrow LiH + H$*, J. Phys. Chem. A **103** (1999), 11080–11088.

[47] C. M. Lindsay and B. J. McCall, *Comprehensive evaluation and compilation of H_3^+ spectroscopy*, J. Mol. Spec. **210** (2001), 60–83.

[48] B. J. Mccall, A. J. Huneycutt, R. J. Saykally, T. R. Geballe, N. Djuric, G. H. Dunn, J. Semaniak, O. Novotny, A. Al-Khalili, A. Ehlerding, F. Hellberg, S. Kalhori, A. Neau, R. Thomas, F. Österdahl, and M. Larsson, *An enhanced cosmic-ray flux towards ζ Persei inferred from a laboratory study of the $H_3^+ - e^-$ recombination rate*, Nature **422** (2003), 500–502.

[49] S. Miller, J. Tennyson, and B. T. Sutcliffe, *Forbidden rotational and ro-vibrational transitions in H_3^+: first principles calculations*, Mol. Phys. **66** (1989), 429.

[50] I. Mistrík, R. Reichle, H. Helm, and U. Müller, *Predissociation of H_3^+ rydberg states*, Phys. Rev. A **63** (2001), 042711.

[51] MOLPRO, *a package of ab initio programs designed by H.-J. Werner and P. J. Knowles, with contributions from* R. D. Amos, A. Bernhardsson, A. Berning, P. Celani, D. L. Cooper, M. J. O. Deegan, A. J. Dobbyn, F. Eckert, C. Hampel, G. Hetzer, P. J. Knowles, T. Korona, R. Lindh, A. W. Lloyd, S. J. McNicholas, F. R. Manby, W. Meyer, M. E. Mura, A. Nicklass, P. Palmieri, R. Pitzer, G. Rauhut, M. Schütz, U. Schumann, H. Stoll, A. J. Stone, R. Tarroni, T. Thorsteinsson, and H.-J. Werner, Birmingham, UK, 2000.

[52] T. J. Morgan, K. H. Berkner, and R. V. Pyle, *Cross sections for the destruction of 1- to 25-keV/nucleon $X^1\Sigma_g^+$ and $c^3\Pi_u$ hydrogen molecules in collisions with h_2 gas*, Phys. Rev. Lett. **26** (1971), 602–604.

[53] U. Müller, Th. Eckert, M. Braun, and H. Helm, *Fragment correlation in the three-body breakup of triatomic hydrogen*, Phys. Rev. Lett. **83** (1999), 2718.

[54] L. Neale, S. Miller, and J. Tennyson, *Spectroscopic properties of the H_3^+ molecule: A new calculated line list*, Astrophys. J. **464** (1996), 516–520.

[55] D. M. Neumark, *Transition-state spectroscopy via negative ion photodetachment*, Acc. Chem. Res. **26** (1992), 33–39.

[56] L. C. Northcliffe and R. F. Schilling, *Range and stopping-power tables for heavy ions*, Nuclear data tables; Section A, vol. 7 (3-4), Acad. Pr., 1970.

[57] A. E. Orel, I. F. Schneider, and A. Suzor-Weiner, *Dissociative recombination of H_3^+: Progress in theory*, Phil. Trans. R. Soc. Lond. A **358** (2000), 2445–2456.

[58] H. B. Pedersen, N. Djuric, M. J. Jensen, D. Kella, C. P. Safvan, H. T. Schmidt, L. Vejby-Christensen, and L. H. Andersen, *Electron collisions with diatomic anions*, Phys. Rev. A **60** (1999), 2882–2899.

[59] D. H. Perkins, *Introduction to high energy physics*, 2nd ed., Addison-Wesley, 1982.

[60] R. Plašil, J. Glosík, V. Poterya, P. Kudrna, J. Rusz, M. Tichý, and A. Pysanenko, *Advanced integrated stationary afterglow method for experimental study of recombination of processes of H_3^+ and D_3^+ ions with electrons*, Int. J. Mass Spec. **218** (2002), 105–130.

[61] O. L. Polyansky and J. Tennyson, *Ab initio calculation of the rotation-vibration energy levels of H_3^+ and its isotopomers to spectroscopic accuracy*, J. Chem. Phys. **110** (1999), 5056–5064.

[62] H. Preuss and G. Diercksen, *Wellenmechanische Absolutrechnungen an Molekülen und Atomsystemen mit der `SCF-MO-LC(LCGO)` Methode, VII. Das System (LiH_2^-)*, Int. J. Quant. Chem. **1** (1967), 631–635.

[63] R. Prosmiti, O. L. Polyansky, and J. Tennyson, *A global potential energy surface for the H_3^+ molecule*, Chem. Phys. Lett. **273** (1997), 107–296.

[64] H. W. Sarkas, J. H. Hendricks, S. T. Arnold, and K. H. Bowen, *Photoelectron spectroscopy of lithium hydride anion*, J. Chem. Phys. **100** (1993), 1884–1888.

[65] J. Senekowitsch and P. Rosmus, *Ab initio calculation of spectroscopic properties for the $HLiH^-$ ion in the $X^1\Sigma_g^+$ state*, J. Chem. Phys. **86** (1987), 6329.

[66] S. B. Sharp and G. I. Gellene, *Ab initio investigations of $Li^- + nH_2 \rightarrow LiH_2^-(H_2)_{n-1}$, n=1–3*, J. Chem. Phys. **113** (2000), 6122.

[67] F. Sprenger, *Production of cold electron beams for collision experiments with stored ions*, Ph.D. thesis, Universität Heidelberg, 2003.

[68] P. C. Stancil, S. Lepp, and A. Dalgarno, *The lithium chemistry of the early universe*, Astrophys. J. **458** (1996), 401–406.

[69] D. Strasser, L. Lammich, H. Kreckel, S. Krohn, M. Lange, A. Naaman, D. Schwalm, A. Wolf, and D. Zajfman, *Breakup dynamics and isotope effect in H_3^+ and D_3^+ dissociative recombination*, Phys. Rev. A **66** (2002), 32719.

[70] D. Strasser, J. Levin, H. B. Pedersen, O. Heber, A. Wolf, D. Schwalm, and D. Zajfman, *Branching ratios in the dissociative recombination of polyatomic ions: The H_3^+ case*, Phys. Rev. A **65** (2002), 10702(R).

[71] D. Strasser, X. Urbain, H. B. Pedersen, N. Altstein, O. Heber, R. Wester, K. G. Bhushan, and D. Zajfman, *An innovative approach to multiparticle three-dimensional imaging*, Rev. Sci. Inst. **71** (2000), 3092–3–098.

[72] W. C. Stwalley and W. T. Zemke, *Spectroscopy and structure of the lithium hydride diatomic molecules and ions*, J. Phys. Chem. Ref. Data **22** (1993), 87–112.

[73] G. Sundström, J. R. Mowat, H. Danared, S. Datz, L. Broström, A. Filevich, A. Källberg, S. Mannervik, K. G. Rensfelt, P. Sigray, M. af Ugglas, and M. Larsson, *Destruction rate of H_3^+ by low-energy electrons measured in a storage-ring experiment*, Science **263** (1994), 785–787.

[74] T. C. Thompson, G. Izmirlian, Jr., S. J. Lemon, D. G. Truhlar, and C. A. Mead, *Consistent analytic representation of the two lowest potential energy surfaces for Li_3, Na_3, and K_3*, J. Chem. Phys. **82** (1985), 5597–5603.

[75] Z. Vager, R. Naaman, and E. P. Kanter, *Coulomb explosion imaging of small molecules*, Science **244** (1989), 426.

[76] A. J. C. Varandas, F. B. Brown, C. A. Mead, D. G. Truhlar, and N. C. Blais, *A double many-body expansion of the two lowest-energy potential surfaces and nonadiabatic coupling for H_3*, J. Chem. Phys. **86** (1987), 6258–6269.

[77] L. Vejby-Christensen, L. H. Andersen, O. Heber, D. Kella, H. B. Pedersen, H. T. Schmidt, and D. Zajfman, *Complete branching ratios for the dissociative recombination of H_2O^+, H_3O^+, and CH_3^+*, Astrophys. J. **483** (1997), 531–540.

[78] L. Vejby-Christensen, D. Kella, D. Mathur, H. B. Pedersen, H. T. Schmidt, and L. H. Andersen, *Electron-impact detachment from negative ions*, Phys. Rev. A **53** (1996), 2371–2378.

[79] R. von Hahn, R. Cee, M. Grieser, V. Koessler, M. Madert, S. Papureanu, H. Podlech, R. Repnow, D. Schwalm, C.-M. Kleffner, D. Habs, and A. Schemp, *The High Current*

Injector at the MPI für Kernphysik in Heidelberg, Proceedings of the European Particle Accelerator Conference, Stockholm, 1989.

[80] J. K. G. Watson, *An introduction to the spectroscopy of H_3^+*, Phil. Trans. R. Soc. Lond. A **358** (2000), 2371–2384.

[81] R. Wester, F. Albrecht, M. Grieser, L. Knoll, R. Repnow, D. Schwalm, A. Wolf, A. Baer, J. Levin, Z. Vager, and D. Zajfman, *Coulomb explosion imaging at the heavy ion storage ring TSR*, Nucl. Instr. Meth. A **413** (1998), 379–396.

[82] G. Wissler, *Ein Detektorsystem für Umladungs- und Fragmentationsexperimente mit gespeicherten Ionen*, Ph.D. thesis, Universität Heidelberg, 2002.

[83] A. Wolf, *Storage ring experiments with cold molecular ions: The H_3^+ puzzle*, Proceedings of the International Conference on Photonic, Electronic and Atomic Collisions, Stockholm 2003, to be published.

Danksagung